

FABRICATION OF SUPERHYDROPHILIC NANOSTRUCTURED MEMBRANES FOR OIL/WATER

SEPARATION

Zhiwei Liao

A DISSERTATION

in

Chemical and Biomolecular Engineering

Presented to the Faculties of the University of Pennsylvania

in

Partial Fulfillment of the Requirements for the

Degree of Doctor of Philosophy

2019

Supervisor of Dissertation

Daeyeon Lee, Professor, Chemical and Biomolecular Engineering

Co-Supervisor of Dissertation

Shu Yang, Professor, Materials Science and Engineering

Graduate Group Chairperson

John Crocker, Professor, Chemical and Biomolecular Engineering

Dissertation Committee

Daeyeon Lee, Professor, Chemical and Biomolecular Engineering

Shu Yang, Professor, Materials Science and Engineering

Kathleen Stebe, Professor, Chemical and Biomolecular Engineering

Amish Patel, Associate Professor, Chemical and Biomolecular Engineering

**FABRICATION OF SUPERHYDROPHILIC NANOSTRUCTURED
MEMBRANES FOR OIL/WATER SEPARATION**

COPYRIGHT

2019

Zhiwei Liao

To my family

ACKNOWLEDGMENT

First, I would like to thank my advisors, Dr. Daeyeon Lee and Dr. Shu Yang, for their guidance and support throughout my journey as a PhD student at Penn. They have been very patient and dedicated to teach me what I need to do to be a good researcher. They are always willing to share their invaluable experiences and thoughts with me to guide me through tough times. I am very grateful to them and I am very lucky to have them as my advisors.

Next, I would like to thank my dissertation committee members, Dr. Kathleen Stebe and Dr. Amish Patel, for their valuable inputs and discussions on my research topics. What I learned from their classes and research helped me a lot.

I am also very grateful to all current and former members I have encountered Lee and Yang groups. They are interesting and talented people. They never hesitated to offer their help when I needed no matter is about research or just daily life. I feel extremely lucky to know each one of them: Steven Cheng, Yuchong Gao, Saihua Jiang, Jason Jolly, Heesuk Jung, Dae Seok Kim, Se-Um Kim, Young-Joo Lee, Jing Li, Jiaqi Liu, Xinyu Wang, Yuchen Wang, Elaine Lee, Yu Xia, Gaoxiang Wu, Hye-Na Kim, Yubo Zhao, Bo Cao, Kaiyang Yin, Huseyin Kaya, Xinghang Shen, Xinyue Zhang, Evan Dolling, Sipiao Peng, Vidyanand Wagh, Rui Yin, Dengteng Ge, Xiaoming Yang, Younghyun Cho, Francesca Serra, Weerapha Panatdasirisuk, Hyesung Cho, Xu Zhang, and Wei-Liang Chen from Yang group; Neha Manohar, Giuseppe Di Vitantonio, Syung Hun Han, Katie Rose, Wilfredo Ortiz, Jingyu Wu, Bharath Venkatesh, Yiwei Qiang, Tiancheng Wang, Joseph Rosenfeld, Joe Rummaneethorn, Jessica O'Callaghan, Tian Ren, Yupan Wu, Jinpei Huang, David Ring, Yang Lan, Woo-Sik Jang, Danny Strickland, Shizhao Lu, Renjing Huang, Je

Choi, Zhuo Chen, Gang Duan, Yankai Jia, Yuanchi Ma, Jyo Lyn Hor, Katie Pulsipher, Jiayi Deng, Wei-Han Chen, Laura Bradley, Sarah Hann, Tagbo Niepa, Harim Jeon, Heon-Ho Jeong, Tianren Zhang, Tianqi Chen, Martin Hasse, Ankit Kumar, Yingliang Zhou, Weiyang Lim, Miju Kim, Likai Hou, Tae Soup Shim, Yeongseon Jang, Jacob Prosser, Chia-Jun Hsieh, Lu Yan, and Fuquan Tu from Lee group. I feel very lucky to be a part of these two amazing groups.

Finally, I would like to thank my family especially my parents. Without their care and support, I would not have the chance to come to study abroad and pursuit a PhD.

ABSTRACT

FABRICATION OF SUPERHYDROPHILIC NANOSTRUCTURED MEMBRANES FOR OIL/WATER SEPARATION

Zhiwei Liao

Daeyeon Lee

Shu Yang

Membrane separation methods have been reported to be 90% more energy efficient than thermal based separation methods. However, conventional membranes for water filtration suffer from the issue of membrane fouling by oily contents, which leads to a decrease of separation efficiency. One potential approach to overcome this challenge is to introduce superhydrophilic coatings on membrane surface to achieve underwater oil repellent as well as render the membrane with a proper pore size to have the ability to separate challenging oil/water emulsions with nanometer-sized oil droplets. Silica (SiO_2) nanoparticles (NPs) coatings possess great hydrophilicity due to surface hydroxylation and its surface chemistry can be further tuned. Furthermore, if the shape of NPs is anisotropic chain-like shaped, the film it formed upon deposition can be highly rough and porous. However, its superhydrophilicity dissipated with time rather than robust due to high tendency of contamination, and its porous structure and rough surface textures can trap oil compromising the anti-fouling. Smooth solid surfaces grafted with polyelectrolytes can induce oil dewetting and lifting from grafted surfaces by adding water. Combining the chain-like SiO_2 NPs and polyelectrolytes through surface grafting might generate a highly porous and long-lasting robust superhydrophilic coating. To achieve this, we need to

investigate the following questions: (1) How to fabricate this coating based on this idea and does the fabricated coating possess the robust oil repellency under water that we are expecting? (2) Does the oil repellency of the coating preserve when it is applied onto actual membranes and does it enhance the efficiency of the coated membrane filtrating oil/water mixtures? To search the answer these questions, poly(acrylic acid) (PAA)-grafted SiO₂ nanochains are synthesized and made into superhydrophilic coatings. The coating successfully introduces robust anti-fouling to smooth surfaces and can lift trapped oil by immersing into water. Both chain-like shapes of the NP and grafted PAA are essential to ensure the robustness. The coated porous membrane has improved surface wettability and enhanced separation efficiency for oil/water mixtures by having increased breakthrough pressures. In conclusion, the fabrication approach presents a promising future for further studies and applications for oil/water separation membranes.

TABLE OF CONTENTS

ACKNOWLEDGMENT	IV
ABSTRACT.....	VI
LIST OF TABLES	X
LIST OF FIGURES	XI
CHAPTER 1. INTRODUCTION.....	1
1.1 Background	1
1.2 Motivation and Objectives	20
1.3 Thesis Outline	22
CHAPTER 2. ULTRASTABLE UNDERWATER ANTI-OIL FOULING COATINGS FROM SPRAY ASSEMBLIES OF POLYELECTROLYTE GRAFTED SILICA NANOCHAINS	23
2.1 Introduction	23
2.2 Experimental Section	25
2.3 Results and Discussion	30
2.4 Conclusion.....	60
CHAPTER 3. DRASTIC ENHANCEMENT OF OIL/WATER SEPARATION THROUGH POLYELECTROLYTE-GRAFTED SILICA NANOCHAIN COATINGS	62
3.1 Introduction	62
3.2 Experimental Section	65
3.3 Results and Discussion	69
3.4 Conclusion.....	82
CHAPTER 4. FABRICATING JANUS MEMBRANES VIA IMMERSION PRECIPITATION OF POLYMERS ON NANOPARTICLE PACKINGS.....	83

4.1 Introduction	83
4.2 Experimental Section	85
4.3 Results and Discussion	87
4.4 Conclusion.....	99
CHAPTER 5. CONCLUSION AND OUTLOOK	101
5.1 Conclusion.....	101
5.2 Outlook for Future Research.....	103
BIBLIOGRAPHY	105

LIST OF TABLES

Table 1. 1 Summary of fabrication methods for superhydrophilic/underwater superoleophobic surfaces.....	11
Table 2. 1 Global and Local Roughness Obtained from AFM Scan in Terms of the Root Mean Squared Roughness (Rrms), Arithmetic Average Roughness (Ra), and Maximum Roughness Depth (Rmax) of the Coatings.....	42
Table 2. 2 Summary of the abbreviations of the tested samples.....	46
Table 2. 3 Parameters and R-Squared Values for Fitting the Decay Function eq 2-9	53

LIST OF FIGURES

Figure 1. 1 Illustration of a liquid drop on a smooth solid surface at three-phase interface.	2
Figure 1. 2 Illustration of a liquid droplet on a structured surface in the Wenzel state.	3
Figure 1. 3 Illustration of a liquid droplet on a structured surface in the Cassie-Baxter state.	4
Figure 1. 4 (left) A liquid droplet on a vertical surface, with the advancing contact angle of θ_{adv} and the receding contact angle of θ_{rec} . (right) A liquid droplet is sliding on a solid surface at a minimum tilting angle of θ_{slide}	5
Figure 1. 5 Illustration of the liquid spreading on fractal textured or porous surfaces.	8
Figure 1. 6 Schematics of separating oil droplets in water using membranes	16
Figure 1. 7 “Reprinted (adapted) with permission from Chen, C.; Weng, D.; Mahmood, A.; Chen, S.; Wang, J. Separation Mechanism and Construction of Surfaces with Special Wettability for Oil/Water Separation. ACS Appl. Mater. Interfaces 2019, 11 (11), 11006–11027. Copyright 2019 American Chemical Society.” Design strategies of special wettability surfaces and the mechanism of oil/water mixture separation. Superwetting materials with a large pore size are used for stratified mixture separation (top), those with a small pore size for emulsified mixture separation based on size-sieving (bottom left), and those with a moderate pore size for emulsified mixture separation based on demulsification.	19
Figure 2. 1 Amount of NPs deposited on the substrate per unit area with respect to the volume of the NP dispersion used for spray coating.	27
Figure 2. 2 Illustration of the steps to study dewetting of ETPTA fouled on NP coated surfaces.	29
Figure 2. 3 (a) Illustration of the synthesis of SiO ₂ nanochains. (b) Schematics of grafting PAA onto SiO ₂ nanochains. (c–e) SEM images of the assynthesized SiO ₂ nanochains with feed mass ratios of seed solution to water of 0.33, 0.56, and 1. (f) Size distribution of the contour lengths of SiO ₂ nanochains obtained by image processing program ImageJ from analyzing SEM images.	31
Figure 2. 4 FT-IR spectra of PAA, PAA grafted nanochains (PAA-c-SiO ₂), and pristine nanochains (c-SiO ₂). After grafting PAA onto SiO ₂ nanochains, the characteristic peaks of C-H stretching (2961 cm ⁻¹) of carbon chain and C=O stretching (1714 cm ⁻¹) of carboxylic acid are shifted to 2938 cm ⁻¹ and 1655 cm ⁻¹ , respectively, indicating the formation of amide bonds. These peaks are absent in the spectrum of pristine SiO ₂ nanochains.	33

Figure 2. 5 TGA results of pristine SiO ₂ NPs and PAA-grafted SiO ₂ NPs.	35
Figure 2. 6 Cross-sectional SEM images of spray-coated NPs: (a) Spherical SiO ₂ NP coating, (b) SiO ₂ nanochain coating, and (c) PAA-grafted SiO ₂ nanochain coatings. (d) Schematic of the wetting test. Inset: spray coating setup. (e) Optical images of the sessile drop of (top) water in air and (bottom) dichloroethane in water on the pristine silicon (Si) wafer, oxygen plasma treated Si (O ₂ -t-Si) wafer, spherical SiO ₂ NP coating (s-SiO ₂), SiO ₂ nanochain coating (c-SiO ₂), and PAA-grafted SiO ₂ nanochain coating (PAA-c-SiO ₂). (f) Underwater oil contact angles (OCAs) and contact angle hysteresis (CAH) of dichloroethane on Si, O ₂ -t-Si, s-SiO ₂ , c-SiO ₂ , and PAA-c-SiO ₂ . (g) Adhesion hysteresis (ΔW) of dichloroethane on Si, O ₂ -t-Si, s-SiO ₂ , c-SiO ₂ , and PAA-c-SiO ₂	36
Figure 2. 7 (a) Change of water contact angles (WCAs) in air and dichloroethane contact angles (OCAs) in water as a function of the number of spray cycles used in coating PAA-s-SiO ₂ on APTMS treated Si surface. (b-c) Cross-sectional view and (d-e) top-view SEM images of the coatings deposited on APTMS treated Si surface with (b, d) 2 spray cycles and (c, e) 45 spray cycles.	38
Figure 2. 8 Top-view SEM images of (a) spherical SiO ₂ NPs coating, (b) SiO ₂ nanochain coating, and (c) PAA grafted SiO ₂ nanochain coating, respectively. Scale bar: 500 nm. 38	
Figure 2. 9 (a-c) Top-view SEM images and (d-f) AFM images of the spherical SiO ₂ NPs coating (a, d), SiO ₂ nanochain coating (b, e), and PAA grafted SiO ₂ nanochain coatings (c, f), respectively.	41
Figure 2. 10 Optical images of the dichloroethane (DCE) pendent drops underwater on different coating surfaces under compression (top) and stretching (bottom). (Top) the pendent drop is continuously lowered towards the surface until the DCE drop wets the surface or the needle slips to the side of the DCE drop. (Bottom) The DCE drop is pulled away from the surface, showing different degrees of deformation.	44
Figure 2. 11 (a) Schematics of the setup to investigate anti-fouling effect on oil-spread coatings. (b) OCA of ETPTA changes with respect to time during dewetting for spherical SiO ₂ NP coating (s-SiO ₂), SiO ₂ nanochain coating (c-SiO ₂), and PAA-grafted SiO ₂ nanochain coating (PAA-c-SiO ₂) with (inset) optical images. (c) OCA of ETPTA changes with respect to time submerged in water on aged PAA-grafted SiO ₂ nanochain coating (PAA-c-SiO ₂ aged), aged SiO ₂ nanochain coating (c-SiO ₂ aged), and calcinated PAA-grafted SiO ₂ nanochain coating (PAA-c-SiO ₂ calcinated). (d) OCA of ETPTA changes with respect to time submerged in water on aged PAA-c-SiO ₂ , PAA-grafted spherical SiO ₂ NP coating (PAA-s-SiO ₂), and silicon surface grafted with PAA (PAA-Si).	48
Figure 2. 12 Dewetting behaviors of ETPTA on various PAA grafted surfaces, including PAA-grafted nanochain coating (PAA-c-SiO ₂), aged PAA grafted nanochain coating (PAA-c-SiO ₂ aged), PAA-grafted spherical NPs coating (PAA-s-SiO ₂), and PAA-grafted silicon wafer (PAA-Si) as measured by oil contact angle (OCA) vs. time. The solid line is data fitting using a decay function: $1 - \theta \theta \infty = A \cdot \exp - t\tau$	50

Figure 2. 13 Dewetting behaviors of ETPTA on pristine nanochain coating (c-SiO₂), spherical NPs coating (s-SiO₂), aged nanochain coating (c-SiO₂ aged), and calcinated PAA-grafted nanochain coating (PAA-c-SiO₂ calcinated) as measured by oil contact angle (OCA) vs. time. The solid line data fitting using a decay function: $1 - \theta/\theta^\infty = A \cdot \exp - t/\tau$ 51

Figure 2. 14 The saturated oil contact angle (θ^∞) when ETPTA dewetting stops vs. time needed to reach 99% of its θ^∞ , $t_{0.99}$, on different coating surfaces. 52

Figure 2. 15 Cross-sectional SEM images of PAA-grafted SiO₂ nanochain coating after fouled by ETPTA (a) at the beginning and (b) after submerging in water for 1 h, followed by UV curing. (c) Zoomed-in representation of a single nanochain surface inside the oil-fouled region of the substrate. Hydration and imbibition of water molecules into nanopores between PAA-grafted SiO₂ nanochains lead to spontaneous dewetting of the ETPTA from the coating surface. (d) Schematic illustration of ETPTA wetting transition on PAA-grafted SiO₂ nanochain coating from the fouled state to the dewetted state. Note: macroscopically only part of the substrate is covered by the oil drop. 56

Figure 2. 16 Cross-sectional SEM images of NP coatings (a,b) fouled by ETPTA for 30 s, followed by UV curing, and (c,d) fouled by ETPTA for 30 s, submerged in water for 1 h, taken out, followed by UV curing. (a,c) Spherical SiO₂ NP coating and (b,d) pristine SiO₂ nanochain coating. Inset: zoomed-in SEM images. 57

Figure 2. 17 Dichloroethane contact angles on the PAA-c-SiO₂ coated Si surface under water with respect to the time the coating is subjected to a stirred water environment. .. 60

Figure 3. 1 Schematics of the membrane module used for sandwiching membranes during emulsion separation under (left) low pressure and (right) high pressure. 68

Figure 3. 2 Schematic of the fabrication steps and close-up of PAA-grafted nanochains coated the porous membranes. 70

Figure 3. 3 Top-view SEM images of (a) pristine and (b) PAA-grafted nanochain coated PC, (c) pristine and (d) PAA-grafted nanochain coated MCE membranes, (e) pristine and (f) PAA-grafted nanochain coated SSM, respectively. 71

Figure 3. 4 (a, c) Water contact angles measured in air. (b, d) Underwater contact angles of dichloroethane on pristine and PAA-grafted nanochain coated PC, MCE, and SSM. .. 73

Figure 3. 5 Image captures of the sticky dichloroethane drop on pristine MCE under water during shaking (top), and the bouncy dichloroethane drop rolling off from a tilted coated MCE (bottom). 74

Figure 3. 6 Optical images of dead-end gravity driven filtration of hexadecane-water free mixtures on (a) pristine and (b) PAA-grafted nanochain coated PC membrane, (c) pristine and (d) PAA-grafted nanochain coated MCE membrane, (e) pristine and (f) PAA-grafted

nanochain coated SSM, respectively. (g) Average flux of dead-end gravity driven filtration of hexadecane-water free mixtures. 76

Figure 3. 7 (a) A flowchart of the pressure driven filtration for hexadecane-water emulsions using PAA-grafted nanochain coated PC membrane: (b) feed and (c) filtrate. (d) size distribution of the oil drop from DLS..... 79

Figure 3. 8 (a) Relation of oil rejection and flux normalized by transmembrane pressure for emulsion separation using pristine and coated PC. (b) Optical microscope image of the filtrate from emulsion separation using PC membrane. (c) DLS result of the feed and the filtrate from emulsion separation using PC with and without the coating..... 80

Figure 3. 9 (a) Schematic illustration of the setup used for measuring the breakthrough pressures for completely water pre-wetted membranes. (b) Measured breakthrough pressures for pristine and coated SSM, MCE, and PC. (c) The preservation time of the continuous water film on completely water pre-wetted membranes. 80

Figure 4. 1 Schematic of each steps to fabricate the membrane. 88

Figure 4. 2 (a) Cross-sectional SEM image of the Janus membrane. (b) Zoomed-in image of the membrane area at the NP-PVDF interface. (c, d) Top-view SEM image of the Janus membrane surface on the side with (c) SiO₂ NPs and the side with (d) PVDF, respectively. 89

Figure 4. 3 (a) Contact angles of water (WCA) in air and dichloroethane (OCA) under water on nanoparticle (NP) side of the membrane and PVDF side of the membrane. (b) Goniometer captured images of a pendent drop of dichloroethane in water contacting the NP side (top) and PVDF side (bottom) of the membrane. (c) Visual images of dispensing drops of dichloroethane dyed by oil red under water onto the NP side (top) and the PVDF side (bottom) of the membrane. (d) Visual image captures of the Janus membrane (left) during filtrating the DI water and (right) at the end of filtrating the hexadecane/water free mixture. 91

Figure 4. 4 (a) The correlation between the thickness of the NP layer on top of the sacrificial layer after the flow coating versus the blade casting speed during the flow coating. (b-f) Cross-sectional SEM images of the NP layer deposited on the sacrificial layer using flow coating with blade speed of (b) 0.5 mm/s, (c) 1 mm/s, (d) 5 mm/s, (e) 10 mm/s, and (f) 20 mm/s, respectively..... 93

Figure 4. 5 (a, b, c) Top-view and (d, e, f) zoomed-in SEM images of the NP side of the final Janus membrane with blade speed of (a, d) 5 mm/s, (b, e) 10mm/s, and (c, f) 20 mm/s during the flow coating step of the fabrication procedure, respectively. 94

Figure 4. 6 (a) Schematic illustration of the spray coating step for the NP layer replacing the second step, flow coating NPs, of the fabrication procedure in Figure 4.1. (b) Cross-

sectional and (c, d) top-view SEM images of the final Janus membrane when the NP layer is spray coated instead of flow coated during the second step of the fabrication. Note: red circles in dashed line indicates the PVDF bridging between NPs. 96

Figure 4. 7 (a) Schematic illustration of the particle shape changes from spherical NPs to chain-like shaped NPs. (b) Top-view and (c) cross-sectional SEM images of the NP side of the final Janus membrane when the spray coated NP is chain-like shaped instead of spherical during the NP coating step of the fabrication. (d, e, f) Zoomed-in SEM images of three distinctive regions of the membrane surface showed in Figure 4.7b. Note: the red, blue, green colored letters and markers in (b) corresponds (d), (e), and (f), respectively.97

Figure 4. 8 (a) Top-view SEM image of the PVDF membrane surface at an interface with the left-hand side of the membrane in the image formed using the procedure in Figure 4.2 with 10 wt% of NP solution during the flow coating, and the right-hand side of the membrane in the image formed without any NP solution coating in the fabrication procedure. (b) Zoomed-in SEM image of the left-hand side of the membrane in Figure 4.8a. (c) Zoomed-in SEM image of the right-hand side of the membrane in Figure 4.8a. (d) Cross-sectional SEM image of the Janus membrane with visual cracks on the NP layer and (e, f) their zoomed-in SEM images. 99

CHAPTER 1. Introduction

1.1 Background

1.1.1 Controlling Surface Wettability

When a drop of water contacts a solid surface, the water drop may stick to the surface and form a hemispherical cap. It may also completely spread into a thin layer of water film. If the surface is not smooth or has pores, the water drop may bead up and bounce and roll off from the surface when tilted, or it may stick onto the surface and gradually impinge into pores, forming a continuous water film on the surface. These different wetting behaviors on different surfaces are governed by surface topography and surface chemistry at the three-phase contact line, which the latter is determined by molecular interactions at the interface, including electrostatic interactions, hydrogen bonding, and van der Waals interactions.¹ The ability to control different wetting behaviors is important to many applications.^{2,3}

1.1.1.1 Wetting on Smooth Surfaces

As demonstrated in Figure 1.1, in a system of a liquid drop sitting on a solid smooth surface in a vapor environment, the equilibrium contact angle of this liquid on the surface is described by Young's equation⁴ as

$$\cos \theta = \frac{\gamma_{SV} - \gamma_{SL}}{\gamma_{LV}} \quad (1-1)$$

where θ is the equilibrium contact angle, also referred as the Young's contact angle. γ_{SV} , γ_{SL} , and γ_{LV} are the interfacial tension of the solid-vapor interface, the solid-liquid interface, and the liquid-vapor interface, respectively. When the interfacial tensions at the three phase contact line are balanced, the contact angle defines the wettability of the surface.⁵ For a water droplet on a surface, if $\theta > 90^\circ$, the surface is considered hydrophobic. If $\theta < 90^\circ$, the surface is considered hydrophilic. Therefore, change of the surface chemistry of the solid surface will lead to change of the surface wettability, as interfacial tensions originate from intermolecular interactions.⁵

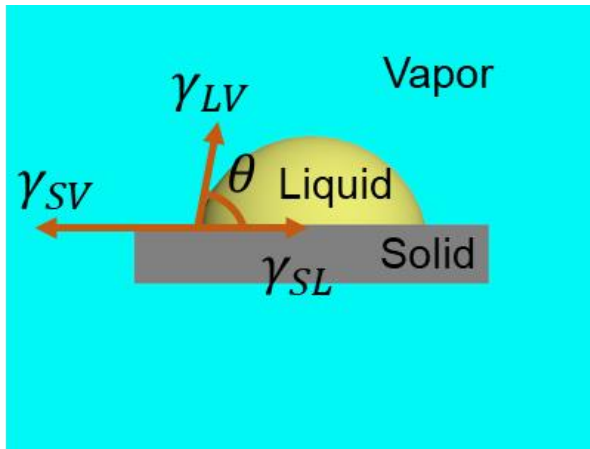


Figure 1. 1 Illustration of a liquid drop on a smooth solid surface at three-phase interface.

1.1.1.2 Wetting on Structured Surfaces

In the real world, most surfaces are not smooth and contain surface textures such as pores, grooves, regular or irregular protrusions. Therefore, wetting behaviors of liquids on structured surfaces are more complex and the Young's equation can no longer be applied.

On a rough surface where the liquid fully wets the grooves of the surface textures as demonstrated in Figure 1.2, the wetting behavior can be described by the Wenzel's equation⁶ as

$$\cos \theta_W = r \cdot \cos \theta \quad (1-2)$$

where θ_W is the observed apparent contact angle in the Wenzel state, and r is the roughness factor which is the ratio of the actual contact area over the projected area, typically greater than 1.

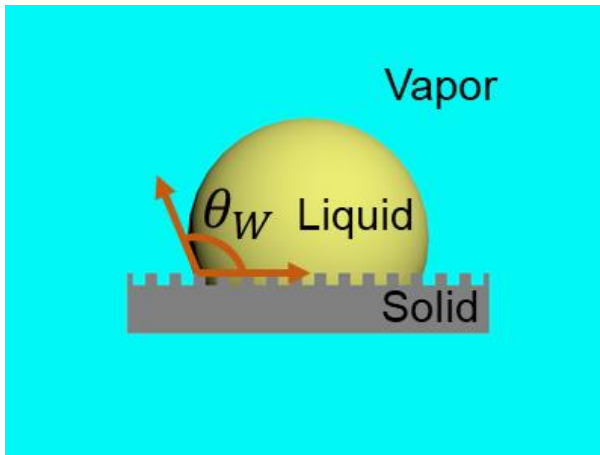


Figure 1. 2 Illustration of a liquid droplet on a structured surface in the Wenzel state.

When liquid sits on top of the surface textures, leaving some parts of the liquid “suspended” as showed in Figure 1.3, the wetting is in so-called Cassie-Baxter state⁷ described as

$$\cos \theta_{CB} = f_s \cdot \cos \theta - (1 - f_s) \quad (1-3)$$

where θ_{CB} is the observed apparent contact angle in the Cassie-Baxter state, and f_s is the fraction of the area that has the actual liquid-solid contact.

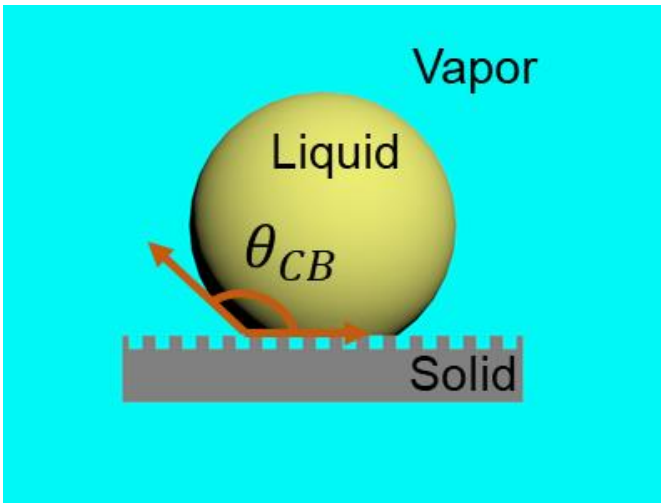


Figure 1. 3 Illustration of a liquid droplet on a structured surface in the Cassie-Baxter state.

On a rough surface, the surface chemistry determines the equilibrium contact angle, whether the surface is hydrophobic or hydrophilic, surface roughness amplifies the degree of hydrophobicity or hydrophilicity, and the surface becomes super-nonwetable or superwetable.

1.1.1.3 Contact Angle Hysteresis

The contact angle hysteresis (CAH) is defined as the difference between the advancing contact angle θ_{adv} and the receding contact angles θ_{rec} ($CAH = \theta_{adv} - \theta_{rec}$). The advancing contact angle and the receding contact angle are dynamic contact angles which are measured when the liquid drop is in movement or the three-phase contact line is moving. The measurement of dynamic contact angles is more consistent than static contact

angles when the surface is rough or chemically heterogeneous, since the static contact angle changes due to the irregularity of the surface.⁸ The sliding angle is another measurement people often use to describe how strong of the interaction between a liquid droplet and the surface, which is the minimum tilting angle of the surface when the droplet starts to roll (Figure 1.4).

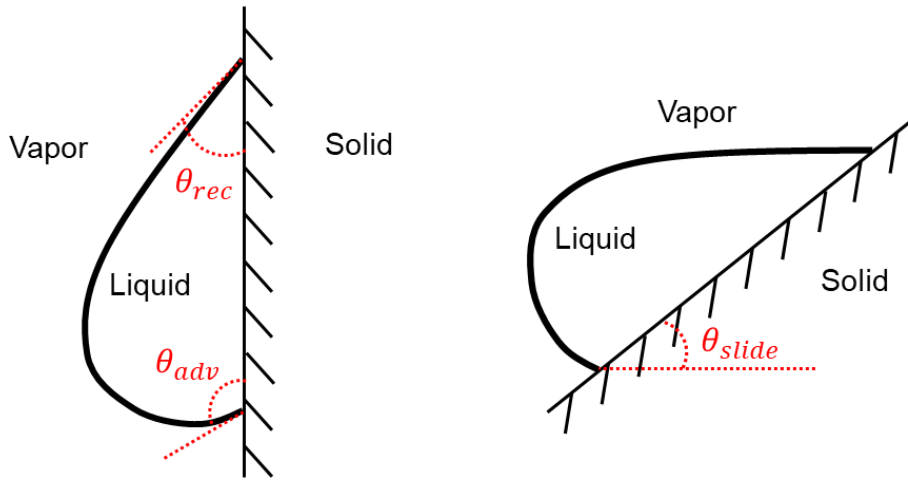


Figure 1. 4 (left) A liquid droplet on a vertical surface, with the advancing contact angle of θ_{adv} and the receding contact angle of θ_{rec} . (right) A liquid droplet is sliding on a solid surface at a minimum tilting angle of θ_{slide} .

1.1.1.4 Superhydrophobic and Superhydrophilic Surfaces

When the apparent contact angles θ' (either Wenzel or Cassie-Baxter contact angles) of a water drop on a surface is greater than 150° with very low contact angle hysteresis or sliding angles (only a few degrees), the surface is referred as superhydrophobic.⁹ This definition has been widely used and accepted since the material with the highest Young's

water contact angle is Teflon ($\sim 120^\circ$). Introduction of surface roughness is necessary to increase water contact angle to be greater than 150° .¹⁰ For superhydrophilic surfaces, however, the definition is not a clear-cut.⁹ A surface is referred as superhydrophilic when water spreads on the surface with zero or nearly zero contact angles (less than 5°).^{11,12} However, this definition can be confusing sometimes, because on some smooth freshly prepared surfaces such as gold, glass, and other oxides with exposed hydroxyl groups on the surface, water can spread completely on surface.¹³⁻¹⁶ Therefore, the latest proposed definition is that the superhydrophilic surface is refer to a structured surface ($r > 1$) where water spreads completely.¹⁷

To make superhydrophobic surfaces, both the surface chemistry and the surface structure are critical. According to Eq. 1.2, the Wenzel's equation, an intrinsic hydrophobic surface ($\theta > 90^\circ$), which is determined by its surface chemical composition, can increase its apparent contact angle above 150° ($\theta_w > 150^\circ$) through surface roughening ($r > 1$). However, droplets in Wenzel state has large contact angle hysteresis (over 2 times higher than Cassie state) due to large contact area with the surface. For example, the contact angle hysteresis of a drop in Wenzel state can be 3 times higher than when it is in Cassie state for the case of $r = 2$.¹⁸ When the surface is intrinsically hydrophilic ($\theta < 90^\circ$), surface roughness reduces the apparent contact angle. Therefore, to create a superhydrophobic surface, it is important that the water drop should be in Cassie-Baxter state, that is, water has minimal contact with the surface, having air pocket underneath the water droplet, resulting in low contact angle hysteresis and sliding angles. However, water droplets in Cassie-Baxter state can collapse into Wenzel state. The critical contact angle θ_c is used to

describe the condition for wetting transition from Cassie-Baxter state to Wenzel state and it is described as

$$\cos \theta_c = \frac{\varphi - 1}{r - \varphi} \quad (1-4)$$

where φ is the fraction of solid-liquid interface where drop is in contact with surface (the f_s in Cassie-Baxter equation) and r is the roughness factor in Wenzel equation. Note that this bounds the critical angle between 0° and 90° .¹⁹ If the contact angle is less than the critical contact angle, the liquid penetrates and spreads on the textured surface. Therefore, when the contact angle is greater than the critical contact angle, Cassie-Baxter state can be maintained, which is very important to maintain the superhydrophobic surfaces.

Similar to superhydrophobic surfaces, if the surface is intrinsically hydrophilic ($\theta < 90^\circ$), increase of surface roughness ($r > 1$) can reduce the apparent contact angle (θ_W) according to Eq. xx, leading to superhydrophilicity ($\theta_W \approx 0^\circ$). For example, when θ is less than 60° , surfaces with $r = 1.2 - 2$ become superhydrophilic.⁹ However, it becomes impractical for surfaces that have θ greater than 65° , where r has to be extremely high to achieve superhydrophilicity according to Wenzel equation. For fractal surfaces with a large r (2.6 to 4.4), it cannot achieve the zero apparent contact angle even with low values of θ such as alkylketene dimer (AKD) surfaces.^{20,21} Later people recognized that such Fractal-like structured surfaces should be treated as porous surfaces. Due to capillarity, liquid spontaneously invades into the texture of porous materials while the remaining liquid stays on the surface, leaving a patch work of liquid and solid (Figure 1.5).⁹

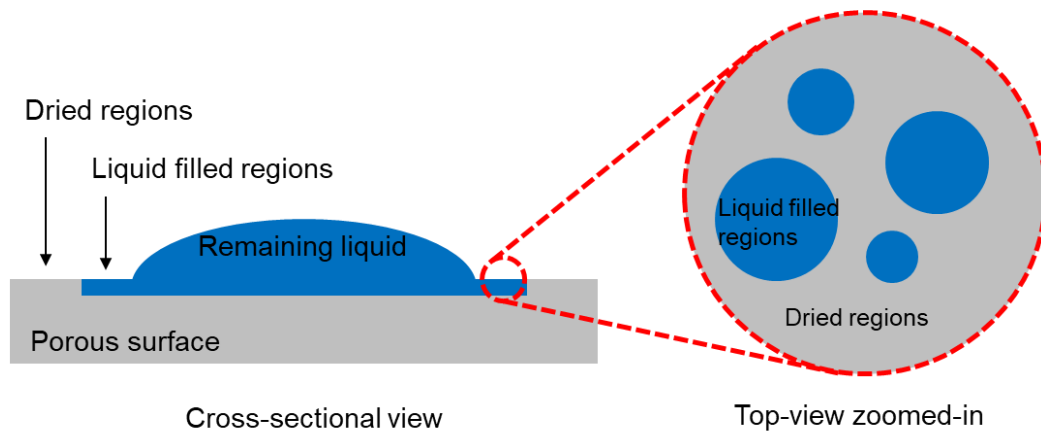


Figure 1. 5 Illustration of the liquid spreading on fractal textured or porous surfaces.

For these structured surfaces that is infiltrated by the wetting liquid, air is replaced by the liquid, the apparent contact angle can be described as

$$\cos \theta_p = f_s(\cos \theta - 1) + 1 \quad (1-5)$$

where θ_p is the apparent contact angle, θ is the intrinsic contact angle, and f_s is the fraction of liquid-solid contact. This equation looks very similar to Cassie-Baxter equation, which are indeed interchangeable simply by replacing the air-liquid contact with the liquid-liquid contact. From this equation, we learn that in theory every hydrophilic surface ($\theta < 90^\circ$) can reduce its apparent water contact angle by increase the porosity. If the porosity of the surface is larger than the liquid volume used in the spreading test, a zero apparent contact angle might also be observed since all the wetting liquid is impregnated into the pores.⁹

1.1.1.5 Underwater Superoleophobicity

Like the superhydrophobicity, the superoleophobicity is referring to the same super-nonwetting behavior (with high contact angles over 150° and small of work of adhesion below 0.1 mN/m) of oils on surfaces. However, it is more challenging to achieve superoleophobicity, because oils have much lower surface tension than water. The term underwater superoleophobicity originates from the inspiration of observing and mimicking the oil repellency of fish scale under water by replicating its structure and chemical composition.²² The constructed surfaces are underwater superoleophobic (dichloroethane contact angle up to 174.8° in water and adhesion force of $10.2 \mu\text{N}$) and also superhydrophilic (water contact angle of less than 5°). The wetting behavior is described using Cassie-Baxter equation in an oil/water/solid system instead of its original water/air/solid system. Later on, many underwater superoleophobic surfaces made based on this concept are also all superhydrophilic surface.²²⁻²⁹ Even though there have not been a clear statement to define the relation between superhydrophilicity and underwater superoleophobicity, people have been using these two terms, superhydrophilic and underwater superoleophobic, interchangeably.

1.1.1.6 Fabrication of Superhydrophilic/Underwater Superoleophobic Surfaces

To create a robust superhydrophilic/underwater superoleophobic surface, the modification of the surface chemistry and manipulation of the surface texture are usually both involved. One approach to fabricate superhydrophilic surfaces is to choose an intrinsic hydrophilic

material as the substrate and then directly introduce surface textures via various methods to obtain superhydrophilicity/underwater superoleophobicity. For examples, using femtosecond laser microfabrication on silicon wafer surface to create hierarchical micro/nanostructures.²⁴ Lithography etching can also be used on silicon surfaces to create microstructures to obtain superhydrophilicity/underwater superoleophobicity.²² It can also be done by using surface oxidation of copper surfaces.²⁵ Another approach is to choose an initial substrate and modify both the surface structure and chemistry. For examples, one method is using base corrosion to create surface structures followed by sputtering of gold and self-assembly of functionalized thiols to modify surface chemistry.³⁰ Another one is to use PDMS copy an existing pattern through soft lithography and the surface treated with oxygen plasma to increase the hydrophilicity.³¹ Assembly of chemically surface-modified nanoparticles to form textured surface are also used to create robust superhydrophilic surfaces.³² Superhydrophilic/underwater superoleophobic surfaces can also be made directly through fabricating freestanding membranes via phase separation of polymer solutions, such as salt-induced phase inversion of poly(acrylic acid)-grafted PVDF (PAA-g-PVDF).³³ It can also be made through electrospinning of polymer solutions such as polycaprolactone.³⁴ Other methods are summarized in Table 1.1.

Table 1. 1 Summary of fabrication methods for superhydrophilic/underwater superoleophobic surfaces.

Categories	Materials	Fabrication Methods	Reference
Create textures on substrates	Silicon wafers, silica glass surfaces, TiO ₂ surfaces, Ti surfaces	Femtosecond laser microfabrication to add hierarchical structures	24,27,28,35,36
	Silicon wafers	Lithography etching	22,37
	Copper mesh, copper sheets, copper wires	Surface oxidation by base (NaOH, ammonia)	25,38,39
	TiO ₂ NP film and ZnO	Hydrothermal process to grow ZnO nanorods on TiO ₂	40
	ITO glass and TiO ₂	Spin coating of TiO ₂ NPs	41
	Sapphire and ZnO, mesh and ZnO	Chemical vapor deposition of ZnO	42,43
Modify both chemistry and structures on substrates	Copper foil	Base corrosion followed by sputter of cold and self-assembly of functionalized thiols	30
	PDMS	Soft lithography followed by oxygen plasma treatment	31

	PAA-grafted silica nanoparticles (NPs), silane modified silica NPs, mixture of silica NPs and EAC, TiO ₂ NPs	Spray coating on silicon wafer, paper, glass, cotton fabrics, stainless steel mesh	32,44-48
	Silica nanoparticles and polyelectrolytes, TiO ₂ and SiO ₂	Layer-by-layer (LbL) assembly dip coating, LbL spray coating	49-52
Freestanding	PAA-g-PVDF, PDH and PVDF, PAAS-g-PVDF	Phase separation, phase separation followed by crosslinking, phase inversion with mesh	33,53,54
	Polycaprolactone, poly(ethylene terephthalate) and poly(vinyl alcohol)	electrospinning	34,55

The grafting of polymers onto surfaces to obtain superhydrophilicity/underwater superoleophobicity has attracted lots of attentions recently because the surface wettability can be modified by proper choosing the chemical structure of surface-grafted polymers.⁵⁶ For examples, By grafting water-soluble or hydrophilic polymer such as poly(methacrylic acid sodium salt) (PMANa) onto surfaces, the grafted surface can become more hydrophilic but without changing in the bulk performance of the substrates.⁵⁷ Besides changing the chemical composition of the functional group, the conformational change of the polymer chain also involves and affects the surface wetting. Grafted hydrophilic polymer brushes collapse when dry and extend when hydrated. For example, When the grafted polymer is

hydrophilic but nonionic such as poly(2,3-dihydroxypropyl methacrylate) (PDHMA), poly(vinyl alcohol) (PVA), and poly(oligo(ethylene glycol) methacrylate) (POEGMA), the grafted surface is more hydrophilic and underwater oleophobic. However, the water contact angle of a flat surface coated with these polymers is typically around 45° to 74° and the underwater oil contact angle is between 89° to 119° . It is still far away from the contact angle criteria for superhydrophilicity/underwater superoleophobicity.⁵⁷ For weak polyelectrolytes such as poly(acrylic acid) (PAA), it is possible to improve the water spreading and reduce water contact angles by increasing thickness of the polymer brush due to its strongly hygroscopic property.⁵⁸

If grafted polymers are ionic hydrophilic polymers or strong polyelectrolytes including negatively charged polymers, positively charged polymers, or zwitterionic polymers such as poly(methacrylic acid sodium salt) (PMANa), poly(2-(methacryloyloxy)ethyltrimethylammonium chloride) (PMTAC), poly(3-sulfopropyl methacrylate potassium salt) (PSPMK), poly(4-[dimethyl(2'-methacryloyloxyethyl)ammonio]butanoate) (PDMAB), their water contact angles are much smaller and in the range of 7° to 31° and underwater contact angles are above 150° . However, there are still strong interactions between the grafted surface and the oil, as the oil droplet can still adhere on the surface.⁵⁷ It is common to observe surfaces grafted with polyelectrolytes have low but a finite water contact angle. This is because a highly ordered hydrogen bonding network of water molecules is formed in the thin hydrated layer just beneath the water drop. This ice-like structured water prevents the complete spreading of

water.⁵⁶ This thin water layer thickness corresponds to the thickness of the swollen brush and can be hundreds of nanometers long stabilized by the hydration of polyelectrolytes.⁵⁹

So far, smooth surfaces only grafted with some specific types of zwitterionic polymers such as poly[2-(methacryloyloxy)ethyl phosphorylcholine] (PMPC) can have extremely low water contact angles ($< 3^\circ$) and high underwater oil contact angles ($\sim 175^\circ$) with very low oil adhesion (work of adhesion ~ 0.054 mN/m). A smooth surface grafted with PMPC can make an oil film on the surface dewet and detach from the surface by simply immersing the surface into water, indicating the surface is underwater superoleophobic and anti-fouling. Strong polyelectrolytes but non-zwitterionic such as PMANa and PSPMK can also achieve this oil detachment while a pristine hydrophilic silicon surface, fluoropolymer grafted surface, or poly(methyl methacrylate) (PMMA) grafted surface cannot.⁵⁷ This low oil adhesion and anti-fouling effect are contributed by the conformational mobility and high free volume of the hydrated swollen brush, preventing contacts between the oil and the surface. The water in hydrated layer also promotes as lubrication.^{60,61}

Surfaces grafted with other types of zwitterionic polymers such as poly(3-[dimethyl(2'-methacryloyloxyethyl)ammonio]propanesulfonate) (PMAPS) might achieve the same oil detachment under water if there are enough salts added into the water to weaken dipole-dipole interactions between functional groups, switching the brush conformation from collapsed state to extended hydrated state. A more detailed study on poly(sulfobetaine) (PSB) with different alkyl chain spacer lengths (CSL) shows that even though higher relative humidity (RH) makes brushes hydrate more easily due to reduction of the total interfacial free energy, the structure of hydrogen bonding networks is independent of the

CSL and RH. Increasing the ionic strength by adding salts into the system can extend the hydrated layer further through producing a diffusive swollen layer due to charge screening and dissociation of paired sulfobetane groups. Larger CSL increases this ionic strength sensitivity due to more separated partial chargers.⁶² In addition, studies have shown that the excellent hydrophilicity achieved through grafting of ionic polymers can be maintained for a long time, for example, PMPC brushes can maintain low water contact angles ($< 10^\circ$) for over three years in air.⁵⁶ In contrast, hydrophilicity generated on plasma treated surfaces usually lasts only a few minutes.

1.1.2 Superhydrophilic Membranes for Oil/Water Separation

Membrane filtration is considered to be very promising to treat oil/water mixtures due to high selectivity, low energy consumption, and simple operational processes.^{63,64} The separation of oil/water emulsion is more challenging than separating the free mixture, and the main mechanism of separating oil/water mixtures is size exclusion (Figure 1.6).

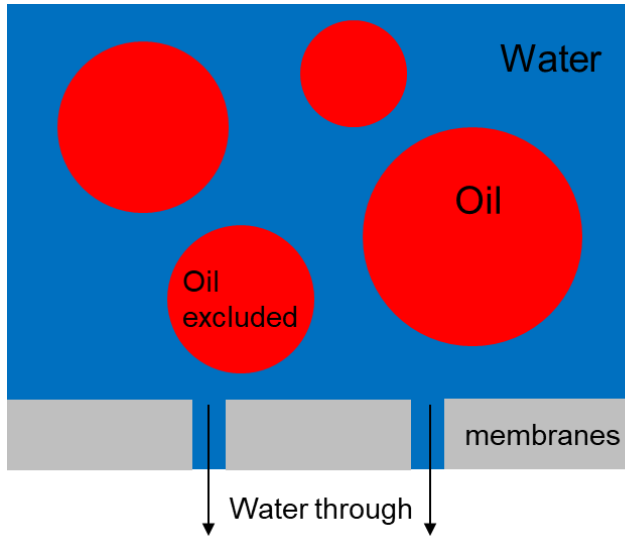


Figure 1. 6 Schematics of separating oil droplets in water using membranes

If the water contact angle here in the presence of oil is less than the critical contact angle, the water preferentially wets the membrane and permeate through, while the oil floats on the membrane surface. The volumetric flow rate Q of a fluid with viscosity μ through a membrane with area A , permeability k , thickness L , pore radius of r and under transmembrane pressure of ΔP can be described using Darcy's law as

$$Q = -\frac{kA}{\mu} \frac{\Delta P}{L} = jA \sim r^4 \quad (1-6)$$

where j is the volumetric flux.¹⁹

Since the main mechanism of separating oil/water mixtures is size exclusion, the ΔP needs to be below the breakthrough pressure P_b to ensure a good selectivity of the filtration. The breakthrough pressure P_b is the minimum pressure at which the oil will be pushed through

the pore despite geometrical constraints or unfavorable wetting characteristics, and it can be described by following Young-Laplace equation as

$$P_b = \frac{2\gamma_{ow} \cos \theta_{adv,o(w)}}{r} \quad (1-7)$$

where γ_{ow} is the water-oil interfacial tension and $\theta_{adv,o(w)}$ is the advancing angle of oil on the membrane material in water. From perspective of designing the membrane, it suggests that the flux can be increased by making the membrane thinner and with larger pores. From the operation point of view, we can also increase the transmembrane pressure to increase the flux. However, this leads to some tradeoffs to be considered. For examples, thinner membrane might have negative impacts on the mechanical robustness of the membrane. Increasing pore size of the membrane makes size exclusion less effective, and also reduces the breakthrough pressure which also reduces the maximum possible flux without compromising the selectivity. There are also lots of challenges such as membrane-fouling and low recyclability when using traditional membranes to deal with oil/water mixtures.⁶⁵

However, as mentioned before about the critical contact angle of the membrane and the advancing contact angle of oil in water on the membrane material, the surface wettability also plays a major role in filtration oil/water mixtures. Recently, there have been significant effort to introduce materials with specific wettability onto membranes to enhance oil/water separation efficacy. Superhydrophilic/underwater superoleophobic membranes are among one of them. Its “oil-blocking” type of approach makes it most relevant for gravity driven oil/water separation since most types of oil have smaller density

than water.⁶⁵ In comparison with traditional membranes, superhydrophilic membranes have better efficiency, selectivity, and recyclability.⁶⁶

Typically, membranes with large pores are used for stratified oil/water mixtures and smaller ones are for separating emulsions.⁶⁵ Nevertheless, questions remain such as low flux as a result of higher separation efficiency using smaller pores, and surface fouling and pore clogging by the residual oils.³³

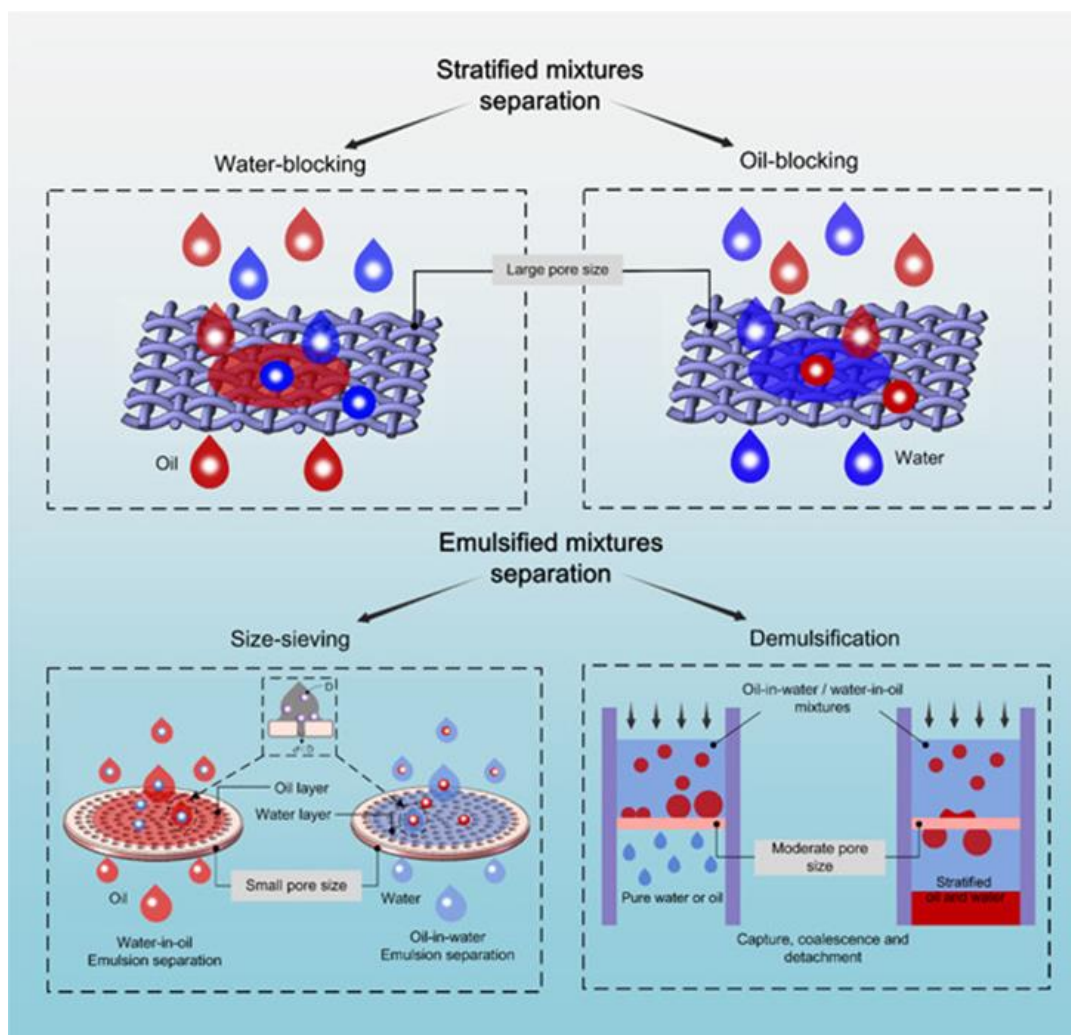


Figure 1. 7 “Reprinted (adapted) with permission from Chen, C.; Weng, D.; Mahmood, A.; Chen, S.; Wang, J. Separation Mechanism and Construction of Surfaces with Special Wettability for Oil/Water Separation. *ACS Appl. Mater. Interfaces* 2019, 11 (11), 11006–11027. Copyright 2019 American Chemical Society.” Design strategies of special wettability surfaces and the mechanism of oil/water mixture separation. Superwetting materials with a large pore size are used for stratified mixture separation (top), those with a small pore size for emulsified mixture separation based on size-sieving (bottom left), and those with a moderate pore size for emulsified mixture separation based on demulsification.

1.2 Motivation and Objectives

1.2.1 Motivation

Recycling of oil contaminated water can be an effective way to address the water scarcity challenge, making the water waste reusable. Membrane separation is one of the most promising approaches to separate oil from water, it is both highly selective and energy efficient. However, traditional membrane suffers from fouling problems over time when dealing with oil/water mixtures, as oil accumulates on the membrane surface and blocks pores, reducing the water flux. Anti-fouling property is necessary for a membrane to effectively separate oil/water mixtures.

Superhydrophilic membranes are one of the solutions. However as mentioned earlier, fabrication approaches such as common surface treatment and surface structure micro- or nanofabrication have problems of scalability and the resulting surface might not be robust enough for oil-lifting or long-lasting. Grafting of polyelectrolytes is one way to add excellent anti-fouling properties to membranes and make the surface underwater superoleophobic. However, so far only a few types of densely grafted zwitterionic polymer brushes have demonstrated excellent anti-fouling properties on smooth surfaces and under neutral aqueous environment. Other zwitterionic types such as PMAPS is not effective unless adding salts.⁵⁷ In addition, the procedure of prepare densely grafted zwitterionic polymers is sophisticated and not scalable. surfaces grafting of weak polyelectrolytes, such as poly(acrylic acid), is much simpler. However, its weak polarity rendered the surface to have large oil adhesion under water, therefore, it cannot lift oil from the surface like

zwitterionic polymers. We note that recent studies on superhydrophilic membranes⁶⁷ usually overlook break-through pressure and transmembrane pressure described in equation 1-6 and equation 1-7, two important parameters that determine the filtration flux in oil/water separation, which are dependent on pore size, porosity, and pore morphology of the membranes. Meanwhile, the mechanical durability and fouling problems have always be unsolving issues of the nanostructured membranes. Therefore, it would be interesting to explore a new approach that can scalably fabricate a more mechanically robust nanostructured membrane with desired wettability.

1.2.2 Objectives

The objective of this dissertation is to explore the answers to the following questions:

- (1) How can we make a robust underwater superoleophobic surfaces based on an approach that combines nanoparticle coatings and polyelectrolyte grafting?
- (2) Can this coating be applied to a commercial porous membranes to improve oil-water separation and filtration efficiency?
- (3) Can we increase the membrane mechanical robustness while maintaining its surface wettability?

1.3 Thesis Outline

Chapter 2 demonstrates a scalable approach to create a robust superhydrophilic/underwater superoleophobic coating from spray coating using anisotropic chain-like silica nanoparticles and poly(acrylic acid) grafts. The combination of the two not only achieve extremely high oil contact angles underwater, but also ultra low oil adhesion that allows the trapped oil extruded from the surface structure by immerse the coating into water. A more detailed comparison oil dewetting dynamic study is included to investigate the main factor determine the oil dewetting speed and completely lift-off.

Chapter 3 shows the performance of the coating developed in *Chapter 2* on actual coated commercially membranes. The coated membranes can effectively separate oil/water free mixtures and emulsions with improved contact angles, reduced oil adhesions, enhanced breakthrough pressure and flux.

Chapter 4 explores a new fabrication approach based on immersion precipitation of hydrophobic PVDF onto pre-deposited hydrophilic silica NP packings to fabricate a freestanding membrane that possesses large wettability contrast on each side and with tunability potential for various applications that benefit from Janus properties.

Chapter 5 concludes the dissertation by summarizing the finding in each chapter and give an outlook for possible future work.

CHAPTER 2. Ultrastable Underwater Anti-Oil Fouling Coatings from Spray

Assemblies of Polyelectrolyte Grafted Silica Nanochains

Reprinted (adapted) with permission from Liao, Z.; Wu, G.; Lee, D.; Yang, S. Ultrastable Underwater Anti-Oil Fouling Coatings from Spray Assemblies of Polyelectrolyte Grafted Silica Nanochains. *ACS Appl. Mater. Interfaces* 2019, 11 (14), 13642–13651. Copyright (2019) American Chemical Society.

2.1 Introduction

Superhydrophilic surfaces play important roles in applications including wastewater treatment,^{33,68} anti-fogging/anti-frosting,^{69,70} anti-corrosion,⁷¹ and self-cleaning.^{72,73} To achieve superhydrophilicity, it is important to manipulate both the surface chemistry and surface topography.^{17,74} Micro- or nanoscale surface features have been shown to induce capillary wicking to facilitate the wetting of water on the surface, resulting in a very low water contact angle (typically below 5°).⁹ This ability to induce complete wetting by water impart superhydrophilic surfaces with exceptional underwater oil repellency.^{22,66,75,76} Surface textures or roughness that can amplify surface hydrophilicity have been produced by various methods, including etching,^{22,24,77} soft lithography,⁷⁸ phase separation of polymers,^{33,53,54} assembly of nanoparticles,^{46,47,49–52,79–81} scaffold templating,^{47,50,82} and electrospinning.^{34,55} Various methods have been introduced to make surface hydrophilic, including oxygen plasma treatment,^{24,78,83} chemical grafting of hydrophilic polymers such as poly(acrylic acid) (PAA),^{33,54,78} poly(3-(*N*-2-methacryloxyethyl-*N*,*N*-

dimethyl)ammonatopropane sultone)-*co*-2-hydroxyethyl methacrylate),⁵³ polydopamine,⁸⁴ and poly[2-(methacryloyloxy)ethyl phosphorylcholine],⁸⁵ physical blending of hydrophilic polymers such as poly(ethylene glycol) diacrylate⁸² and poly(diallyldimethylammonium chloride),⁸³ and coating the surface with a natural compound such as calcium alginate.⁸⁶

Assemblies from silica (SiO₂) nanoparticles (NPs) offer great advantages in scalable manufacturing of nanostructured coatings with tunable surface chemistry to achieve superhydrophilicity^{49–52} or superhydrophobicity.^{46,87–90} Compared to spin coating and drop-casting,⁴⁶ spray coating^{87,91,92} offers rapid coverage over large areas, and has been widely implemented in practical applications. More recently, we have shown that spray coating of elongated SiO₂ NPs with chain-like morphology leads to the formation of films with higher porosity and roughness than those prepared from spherical NPs, resulting in superamphiphobicity that repels both water and oil.^{79,80}

One significant disadvantage of superhydrophilic coatings, however, is that they could be easily fouled by organic contaminants because of their high surface energy, thus losing their superwetting characteristic^{17,93} and anti-fouling properties over time.^{94,95} Meanwhile, once the textured surface is wetted by oil, it is very challenging to recover its superhydrophilicity due to strong capillary interactions within the pores.^{81,96,97}

In this work, we create ultrastable superhydrophilic coatings from spray assemblies of PAA-grafted SiO₂ nanochains, demonstrating underwater superoleophobicity and anti-oil fouling characteristics. Due to the flexible chain conformation and strong affinity to water molecules, polyelectrolyte brushes such as PAA^{33,58,78} and poly[2-(methacryloyloxy)ethyl

phosphorylcholine]^{85,98} can maintain a thick hydration shell close to the surface in non-aqueous environments,^{62,99–101} ensuring stable and long-term hydrophilicity. By taking advantage of unique architecture of SiO₂ nanochains,¹⁰² which show high asperity and large porosity upon assembly, we graft them with PAA brush, followed by spray-coating the NPs on a substrate, demonstrating underwater superoleophobicity with an oil (1,2-dichloroethane, $\gamma = 33.3 \text{ mN m}^{-1}$) contact angle of 165°. Even after the coating is impregnated with oil ($\gamma = 36.3 \text{ mN m}^{-1}$), oil can be readily and completely expelled and lifted-off from the coating within 10 seconds when placed under water, which is not possible from the spherical NP coatings or pristine SiO₂ nanochain coatings.

2.2 Experimental Section

Materials. L-arginine (reagent grade, $\geq 98\%$), tetraethyl orthosilicate (TEOS, reagent grade, 98%), (3-aminopropyl)triethoxysilane (APTES, 99%), (3-aminopropyl)trimethoxysilane (APTMS, 97%), poly(acrylic acid) (PAA, average $M_v \sim 450,000$), dimethylformamide (DMF, anhydrous, 99.8%), trimethylolpropane ethoxylate triacrylate (ETPTA, average $M_n \sim 428$), 2-hydroxy-2-methylpropiophenone (HMPP, 97%), n-hexadecane (ReagentPlus[®], 99%), n-octane (reagent grade, 98%), and n-hexane (anhydrous, 95%) were purchased from Sigma-Aldrich and used as received. Spherical SiO₂ NPs (99.9% SiO₂, diameter, 40 nm) were purchased from General Engineering and Research. Ethanol 200 proof (100%), acetone (99.6%), 1,2-dichloroethane (DCE, $\geq 99\%$), n-decane (99%) and silicone oil (Fisher Chemical[™], S159-500, 100%) were purchased from Fisher Scientific and used as received.

Synthesis of SiO₂ nanochains. SiO₂ nanochains are synthesized in 3 steps: seed synthesis, chain assembly, and chain fixation. To synthesize seeds, 0.0566 g L-arginine was added to the mixture of 40.45 g deionized water (DI water) and 4.2 g tetraethyl orthosilicate (TEOS). The mixture was stirred at a low speed (<100 rpm) at 60 °C overnight with reflux. To grow SiO₂ nanochains, 0.26 g L-arginine was added to the mixture of 8 g seeds solution from the first step, 8 g of DI water, and 64 g of ethanol. The mixture was kept at 60 °C without stirring overnight. To fix the shape of nanochains, 1 g of TEOS was added to the resulting mixture from the second step, which was stirred at a moderate speed (~750 rpm) at 60 °C overnight. After Step 3, the sample was centrifuged at 7500 rpm for 45 min and the precipitate was re-dispersed in DI water by sonication. This process was repeated 3 times. The remaining solid was dried in air.

Grafting of PAA onto SiO₂ nanochains: First, 0.2 g of SiO₂ nanochains were dispersed into a mixture of 3.5 mL DI water and 40 mL ethanol. After adding 110 µL APTES, the mixture was kept at 68 °C with reflux overnight with stirring at a moderate speed (~750 rpm). The product was centrifuged and the remaining solid was re-dispersed in ethanol. The process was repeated three times and the remaining solid was re-dispersed in a mixture of 40 mL DMF and 0.3 g PAA by sonication. The final mixture was heated to 140 °C with reflux overnight with moderate stirring. The product after the reaction was washed with ethanol and DI water by centrifuging and re-dispersing three times before drying in air.

Spray coating of SiO₂ nanochains. To deposit nanochains onto a silicon wafer, the substrate was first rinsed with acetone and followed by oxygen plasma cleaning for 5 min. The synthesized dry particles were then dispersed in ethanol by sonication. The 0.25 wt%

nanochain dispersion was loaded into an airbrush which was connected to an air pump. The dispersion was sprayed at a pressure of 10 psi onto a substrate that was 10 cm away. The spraying stopped when the loaded NP dispersion was depleted. The thickness of the coating was controlled by the loading volume of the NP dispersion and the surface area of the substrate (Figure 2.1).

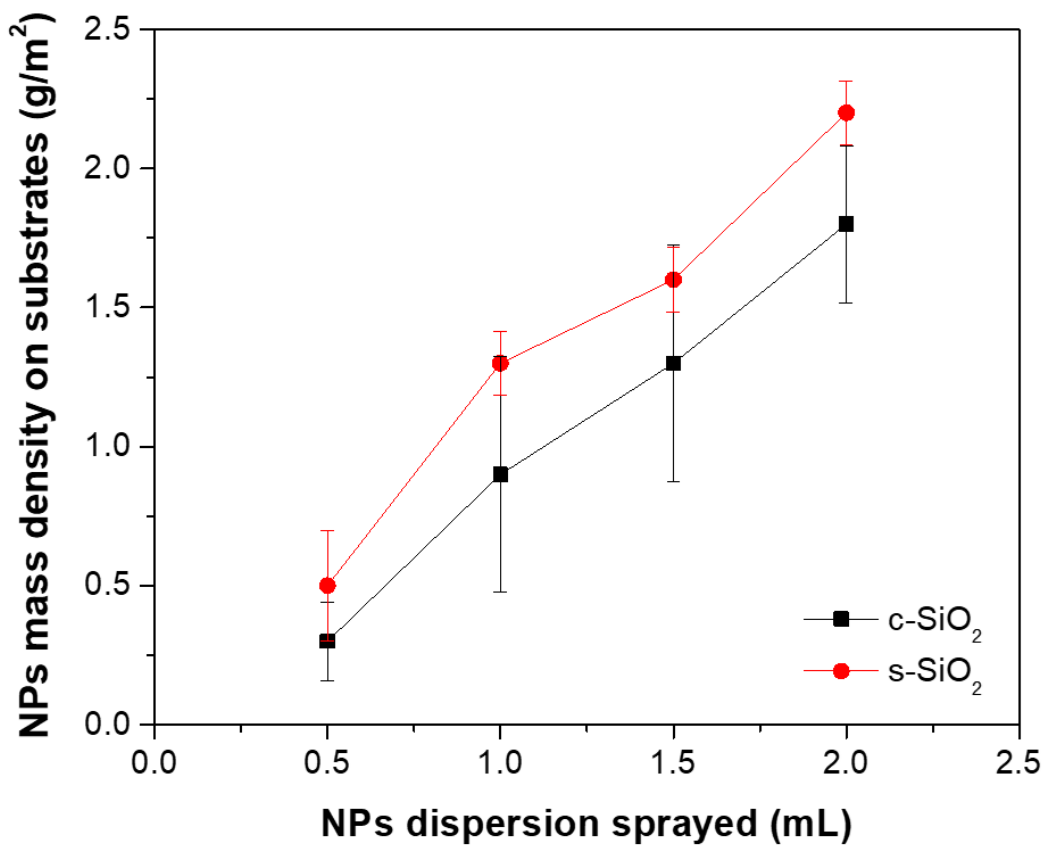


Figure 2. 1 Amount of NPs deposited on the substrate per unit area with respect to the volume of the NP dispersion used for spray coating.

Wettability study. To test underwater superoleophobicity of the coating, the substrate was first placed in a small cubic glass container filled with DI water to pre-wet the surface. A drop of 4 μL DCE was then dispensed onto the substrates and static contact angles were measured. The dynamic contact angles were also measured to determine the contact angle hysteresis and adhesion hysteresis for water pre-wetted samples. To investigate oil lifting behaviors within the nanochain coating, the substrates was purposely fouling with photocrosslinkable monomer, ETPTA ($\gamma = 36.3 \text{ mN m}^{-1}$), as oil. A drop of 4- μL ETPTA was first dispensed on the nanochain coating. After ETPTA completely covered the surface to mimic an oil-fouled environment (30 s), DI water was added into the tank using a syringe to completely cover the entire coating and provide an underwater environment. The oil lifting process was recorded using the camera attached to the goniometer. To show the stability of the coating, we tested the coating wettability right after their oxygen plasma treatment and after storing them in air for at least two weeks.

Coating thickness effect. The substrate, a silicon wafer, was rinsed with acetone and followed by oxygen plasma cleaning for 5 min. To have a better initial contact angle contrast between the water and the oil, the substrate was treated with (3-aminopropyl)trimethoxysilane (APTMS) for 2 hours via vapor deposition in a vacuum chamber. The APTMS-treated substrate was then spray coated with the nanochain dispersion (0.25 wt% in ethanol) using an air brush (10 psi, 10 cm spraying distance). Each time the air brush nozzle sweeping across the substrate was counted as half spraying cycle during the spray coating. The coated samples were characterized using the goniometer and SEM.

Coating durability. A water bath was prepared from a cylindrical glass tank filled with DI water and fitted with a magnetic stir bar. The coating sample was then submerged and suspended in the water bath using copper wires. The entire bath was set to stir at 1000 rpm, exerting a shear stress to the coating. This setting mimics a possible situation that the coating may encounter in a practical application. The sample was periodically taken out of the water bath to characterize the contact angle of dichloroethane underwater as a function of time.

Imaging residual oil remained in the coating. 1 wt% of UV initiator, HMPP, was added to ETPTA to crosslink it (Figure 2.2). The samples were exposed to a LED UV lamp (Thor Lab, 85 mWatt) for 4.5 min, followed by rinsing with ethanol and dried in air before SEM imaging.

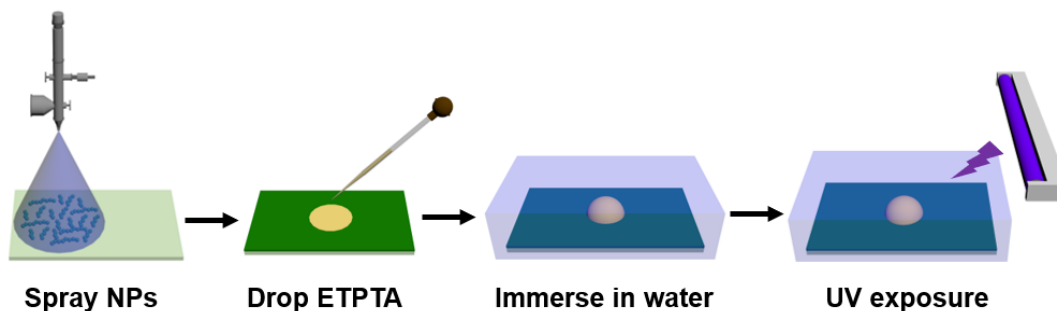


Figure 2. 2 Illustration of the steps to study dewetting of ETPTA fouled on NP coated surfaces.

Calcination Treatment: PAA grafted on SiO₂ nanochains was calcined at 400 °C in a furnace in air (Fisher Scientific, Isotemp[®] Muffle Furnace, 650 series) for 4 h, followed by plasma cleaning (Harrick PDC-001 & PlasmaFlo[™] PDC-FMG, air, high RF level) for 10 min.

Characterization. Morphologies of the synthesized NPs and their assemblies before and after oil fouling were characterized by SEM using the JEOL 7500F HRSEM under acceleration voltage of 5 kV and emission current of 20 µA. Zeta potential of nanochains and their size distribution were measured by a Delsa Nano C (Beckman Coulter) and Zetasizer Nano S (Marvern Instruments, UK) at 25 °C in water, respectively, based on dynamic light scattering (DLS). AFM images were scanned at 324 kHz over an area of 5 µm x 5 µm using Bruker Icon AFM (Dimension Icon with ScanAsyst, Bruker NanoScope[®] V). FTIR spectra were obtained from Nicolet iS5 FTIR Spectrometer (Thermo Scientific) in the transmittance mode. Thermogravimetric analysis (TGA) was performed on an SDT Q600 (TA Instruments) with at a heating rate of 10°C/min in nitrogen. The static and dynamic contact angles of DCE underwater were measured by a ramé-hart goniometer (Model 200). Dewetting of ETPTA underwater were recorded and analyzed using Biolin Scientific Attension goniometer.

2.3 Results and Discussion

The SiO₂ nanochains of different length are synthesized from spherical seeds (~20 nm in diameter) by sol-gel reactions of tetraethyl orthosilicate (TEOS) (Figure 2.3a). By adjusting

the interactions between the seeds through tuning its concentration in the presence of L-arginine and ethanol, spherical seeds assemble into flexible nanochains, which are subsequently locked by a thin coating (12 nm) of SiO₂ shell from TEOS (Figure 2.3b & see details in Experimental Section). Scanning electron microscopy (SEM) images (Figures 1c-1e) show that as the mass ratio of the seed solution to water increases, the chain length increases. Size distributions of these SiO₂ nanochains are summarized in Figure 2.3f based on their contour lengths, which are measured by dynamic light scattering (DLS), ranging from 150 nm to 1000 nm, while the diameter is kept constant, ~ 45 nm. Here, we define short chain as nanochains that have the contour length of 150-200 nm, long chain as those with the contour length greater than 200 nm.

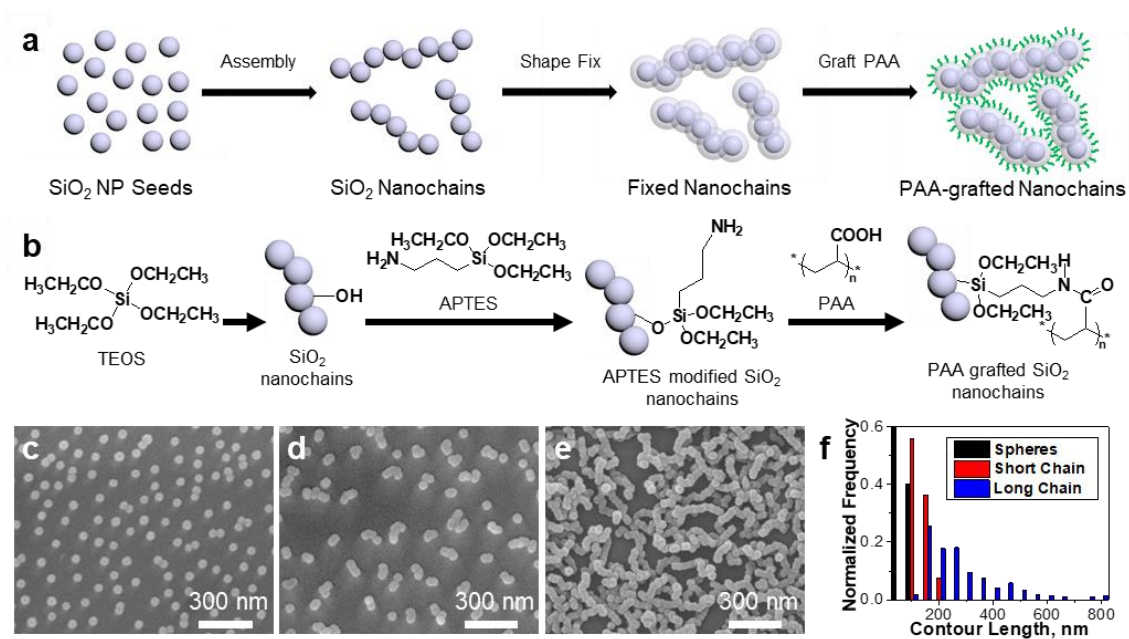


Figure 2. 3 (a) Illustration of the synthesis of SiO₂ nanochains. (b) Schematics of grafting PAA onto SiO₂ nanochains. (c–e) SEM images of the assynthesized SiO₂ nanochains with

feed mass ratios of seed solution to water of 0.33, 0.56, and 1. (f) Size distribution of the contour lengths of SiO₂ nanochains obtained by image processing program ImageJ from analyzing SEM images.

PAA is then grafted onto SiO₂ nanochains via (3-aminopropyl)triethoxysilane (APTES) (Figure 2.3b). Here, we choose PAA because of its high hygroscopic nature.^{33,58,78} To ensure a full coverage of hydrated PAA brushes on SiO₂ nanochains, we use a high molecular weight PAA ($M_v \sim 450$ kDa). The amino groups from APTES react with the carboxylic acid groups on PAA to form amide bonds, which is confirmed by Fourier transform-infrared (FT-IR) spectroscopy (see Figure 2.4). Zeta potential is measured to determine the surface charge before and after grafting of PAA. The pristine SiO₂ NPs have zeta potential of -47.6 mV due to the presence of silanol groups on the surface. After modification with APTES, the zeta potential changes to $+24.6$ mV. After grafting of PAA, the zeta potential turns negative again, -33.4 mV, confirming the success of grafting PAA.

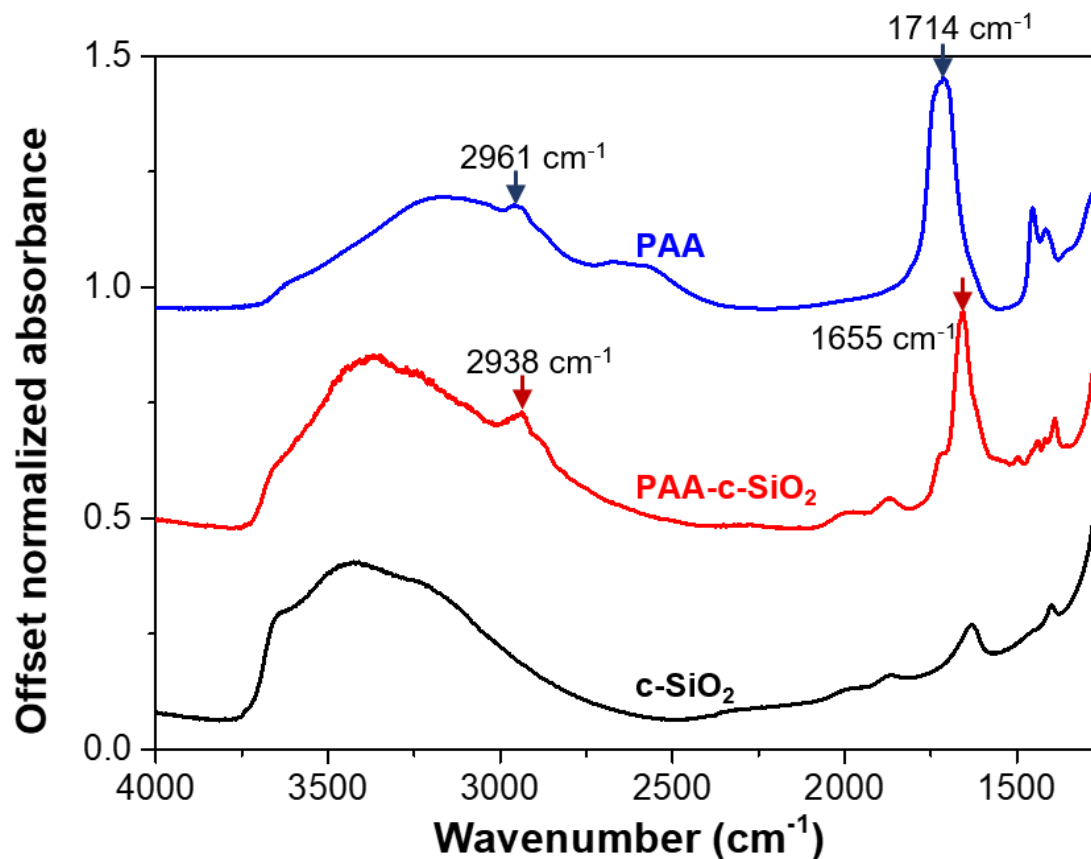


Figure 2. 4 FT-IR spectra of PAA, PAA grafted nanochains (PAA-c-SiO₂), and pristine nanochains (c-SiO₂). After grafting PAA onto SiO₂ nanochains, the characteristic peaks of C-H stretching (2961 cm⁻¹) of carbon chain and C=O stretching (1714 cm⁻¹) of carboxylic acid are shifted to 2938 cm⁻¹ and 1655 cm⁻¹, respectively, indicating the formation of amide bonds. These peaks are absent in the spectrum of pristine SiO₂ nanochains.

To estimate the grafting density of PAA on SiO₂ nanochains, we grafted the same PAA on spherical SiO₂ NPs based on the same chemistry, and measured weight loss using

thermogravimetric analysis (TGA). Spherical NPs were used here because this approach allow us to accurately estimate the surface area. Accordingly, the grafting density of PAA grafted on SiO₂ NPs per gram of NPs, m_{PAA} , is given by

$$m_{PAA} = \frac{(m_i - m_f) - m_f \times \left(\frac{m'_i - m'_f}{m'_f}\right)}{m_f} \quad (2-1)$$

Here, m_i is the initial mass of PAA grafted NPs before TGA and m_f is the residual mass of PAA grafted NPs after TGA. m'_i is the initial mass of pristine NPs before TGA and m'_f is the residual mass of pristine NPs after TGA. To better compare our results with prior work that describes the grafting of PAA onto SiO₂ NPs,¹⁰³ we convert the grafting density to the number of repeat units of PAA per unit area of NPs,

$$D_{PAA} = \frac{\frac{m_{PAA} \times N_A}{M_{PAA}}}{A \times N} \times \frac{M_{PAA}}{M_{ru}} \quad (2-2)$$

Here, M_{PAA} is the viscosity-average molecular weight of PAA we used, which is 450 kDa. N_A is the Avogadro's constant. A is the surface area of a single NP. N is the number of NPs. Both A and N are calculated from the mass, density, and diameter of the NPs we used. M_{ru} is the molecular weight of the repeat unit of the PAA.

Using this method, The grafting density of PAA is estimated 18.8 repeat units per nm² according to thermogravimetric analysis (TGA) (see Figure 2.5), which is close to the literature value, 21.1 repeat units per nm² using the same grafting chemistry with PAA of a smaller molecular weight, 76 kDa.¹⁰³

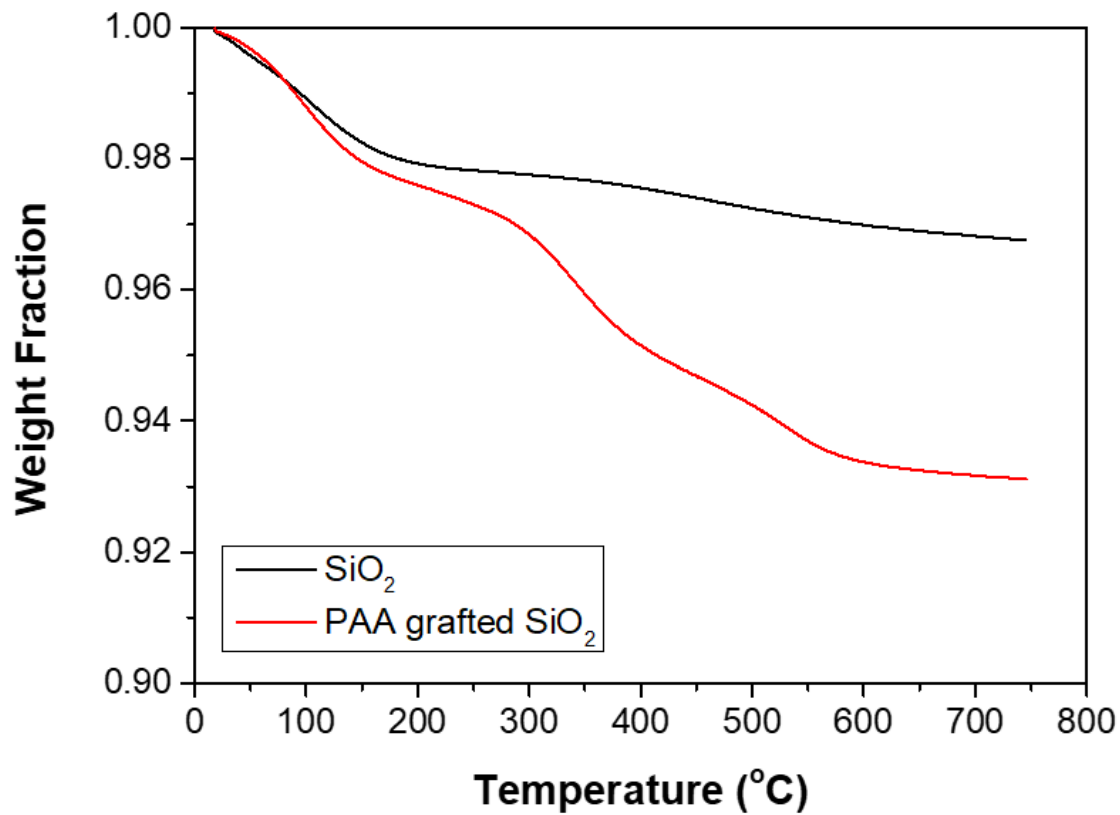


Figure 2. 5 TGA results of pristine SiO₂ NPs and PAA-grafted SiO₂ NPs.

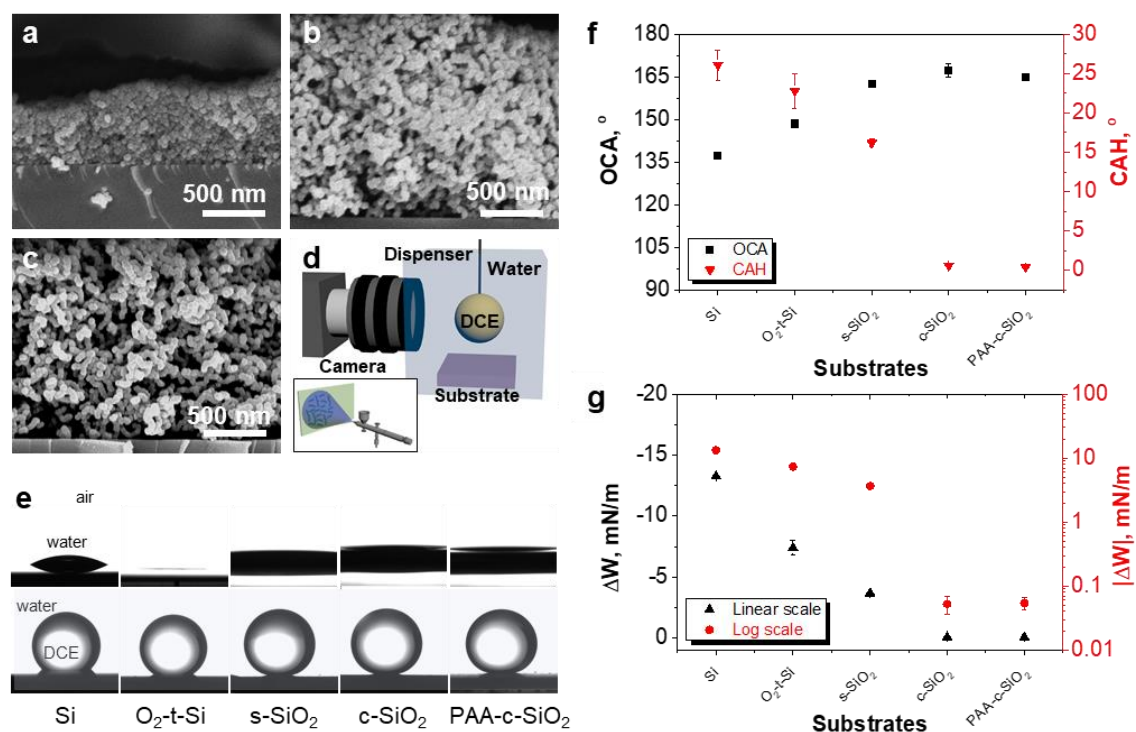


Figure 2. 6 Cross-sectional SEM images of spray-coated NPs: (a) Spherical SiO₂ NP coating, (b) SiO₂ nanochain coating, and (c) PAA-grafted SiO₂ nanochain coatings. (d) Schematic of the wetting test. Inset: spray coating setup. (e) Optical images of the sessile drop of (top) water in air and (bottom) dichloroethane in water on the pristine silicon (Si) wafer, oxygen plasma treated Si (O₂-t-Si) wafer, spherical SiO₂ NP coating (s-SiO₂), SiO₂ nanochain coating (c-SiO₂), and PAA-grafted SiO₂ nanochain coating (PAA-c-SiO₂). (f) Underwater oil contact angles (OCAs) and contact angle hysteresis (CAH) of dichloroethane on Si, O₂-t-Si, s-SiO₂, c-SiO₂, and PAA-c-SiO₂. (g) Adhesion hysteresis (ΔW) of dichloroethane on Si, O₂-t-Si, s-SiO₂, c-SiO₂, and PAA-c-SiO₂.

The longest nanochains we synthesize (weighted-average contour length of 300 nm) are used in our study since they have the lowest percolation threshold, thus, the largest porosity. Their ethanol solution is sprayed onto a substrate using airbrush (Figure 2.6d inset). Since the morphology of the coating depends strongly on the choice of solvent, concentration, spray pressure, distance, and type of solution, we keep all parameters the same, varying only the distance between the air brush and the substrate, to optimize the coating thickness such that the coatings have both high wettability contrast (Figure 2.7a) and a complete coverage of the NPs on the substrate (see Figure 2.7c and 2.7e vs. Figure 2.7b and 2.7d). As seen from Figures 2a-2c and Figure 2.8a-2.8c, SiO₂ nanochains form much more porous structures than spherical SiO₂ NPs. Grafting nanochains with PAA further increases the porosity, due to the charge repulsion between the PAA brushes. The PAA-grafted nanochain coating has the highest thickness of 1,848 nm, whereas the pristine nanochain coating and spherical NP coating have thickness of 1,441 nm 640 nm, respectively.

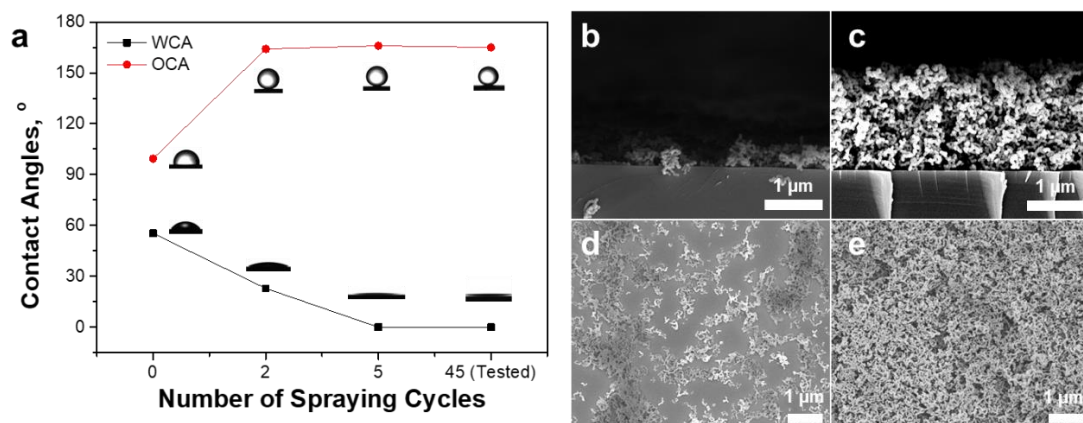


Figure 2. 7 (a) Change of water contact angles (WCAs) in air and dichloroethane contact angles (OCAs) in water as a function of the number of spray cycles used in coating PAA-s-SiO₂ on APTMS treated Si surface. (b-c) Cross-sectional view and (d-e) top-view SEM images of the coatings deposited on APTMS treated Si surface with (b, d) 2 spray cycles and (c, e) 45 spray cycles.

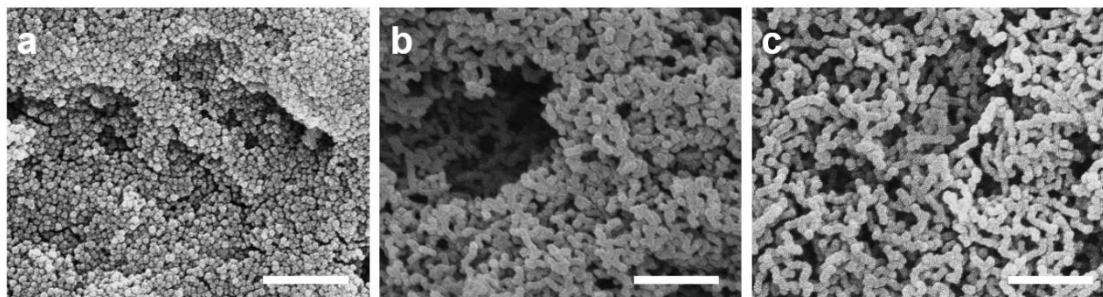


Figure 2. 8 Top-view SEM images of (a) spherical SiO₂ NPs coating, (b) SiO₂ nanochain coating, and (c) PAA grafted SiO₂ nanochain coating, respectively. Scale bar: 500 nm.

To perform the porosity estimation, SiO₂ nanospheres or nanochains are spray coated onto a substrate of surface area A with a film of with thickness h ; the packing fraction, \emptyset , of the nanoparticle (NP) films can be expressed as,

$$\emptyset = \frac{m/\rho_{SiO_2}}{A \cdot h} = 1 - p \quad (2-3)$$

where m , ρ_{SiO_2} , and p are the total mass of the NP spray-coated on the substrate, the density of SiO₂ NPs, and porosity of the film, respectively. Assuming the spray-coated spherical SiO₂ NPs are randomly close packed with \emptyset of 64%,^{104,105} we can estimate the thickness of the spherical SiO₂ NP coating, $h_{spherical}$ as

$$64\% = \frac{m/\rho_{SiO_2}}{A \cdot h_{spherical}} \quad (2-4)$$

Since the volume and concentration of SiO₂ nanochain suspensions are kept the same as the those of spherical SiO₂ nanoparticle suspensions and the substrate area is kept constant, the porosity of spray-coated silica nanochain films can be estimated using,

$$1 - p = \frac{m/\rho_{SiO_2}}{A \cdot h_{nanochain}} \quad (2-5)$$

where $h_{nanochain}$ is the thickness of the nanochain coating. Accordingly, we can estimate the porosity of the nanochain coating for a given coating thickness.

$$p = 1 - 64\% \times \left(\frac{h_{spherical}}{h_{nanochain}} \right) \quad (2-6)$$

According to this approach, the porosity of the PAA-grafted and the pristine nanochain coatings is estimated to be 78% and 72%, respectively, double that of the spherical NP coating, 36%, assuming random close packing for spherical NPs.^{104,105}

In lower magnification SEM images (Figures S4a-S4c), the PAA-grafted SiO₂ nanochain coating (Figure 2.9c) appears to cover the surface rather uniformly with loosely packed worm-like nanochains. In comparison, the pristine SiO₂ nanochain coating (Figure 2.9b) and the spherical SiO₂ NP coating (Figure 2.9a) are rather patchy, displaying microvoids with ridges and valleys. We then use atomic force microscopy (AFM) to characterize surface roughness in local regions (Figures S4d-S4f). Table 2.1 summarizes the estimated root mean squared roughness (R_{rms}), arithmetic average roughness (R_a), and maximum roughness depth (R_{max}) for the three types of coatings over an area of $5 \times 5 \mu\text{m}^2$. Clearly, coatings from spherical NPs ($R_{rms} = 367 \text{ nm}$, $R_a = 291 \text{ nm}$, $R_{max} = 1,753 \text{ nm}$) and pristine nanochains ($R_{rms} = 320 \text{ nm}$, $R_a = 282 \text{ nm}$, $R_{max} = 1,358 \text{ nm}$) are rougher than the PAA-grafted nanochain coating ($R_{rms} = 91 \text{ nm}$, $R_a = 69 \text{ nm}$, $R_{max} = 757 \text{ nm}$). Such large surface roughness of the former can be attributed to the large height changes between ridges and valleys. When we compare the roughness over a smaller area ($1 \times 1 \mu\text{m}^2$), the PAA-grafted coating shows significantly larger roughness ($R_{rms} = 68 \text{ nm}$, $R_a = 53 \text{ nm}$, $R_{max} = 423 \text{ nm}$) than the pristine one ($R_{rms} = 40 \text{ nm}$, $R_a = 31 \text{ nm}$, $R_{max} = 270 \text{ nm}$) and spherical NP coating ($R_{rms} = 39 \text{ nm}$, $R_a = 30 \text{ nm}$, $R_{max} = 259 \text{ nm}$). We note that the roughness of the latter two are measured at the tops of the ridges. These results are consistent with our previous study, which showed rapid evaporation of solvent during spray coating and shape anisotropy of nanochains led to formation of coatings with high protrusion and extreme non-

wettability.^{80,102} We believe grafting of negatively charged PAA brushes onto the surface of nanochains further introduces steric hindrance and charge repulsion during assembly, as evident from the larger porosity vs. that from the pristine nanochains. Moreover, the large molecular weight of PAA could facilitate their physical entanglement between adjacent SiO₂ nanochains, effectively strengthening the coating and preventing collapse of PAA-grafted nanochains caused by capillary pressure during solvent evaporation. Such a collapse may be the reason behind the formation of dense coatings with the ridge-and-valley morphology in spherical NP coatings and pristine nanochain coatings, whereas PAA-grafted nanochains are rather macroscopically uniform overall.

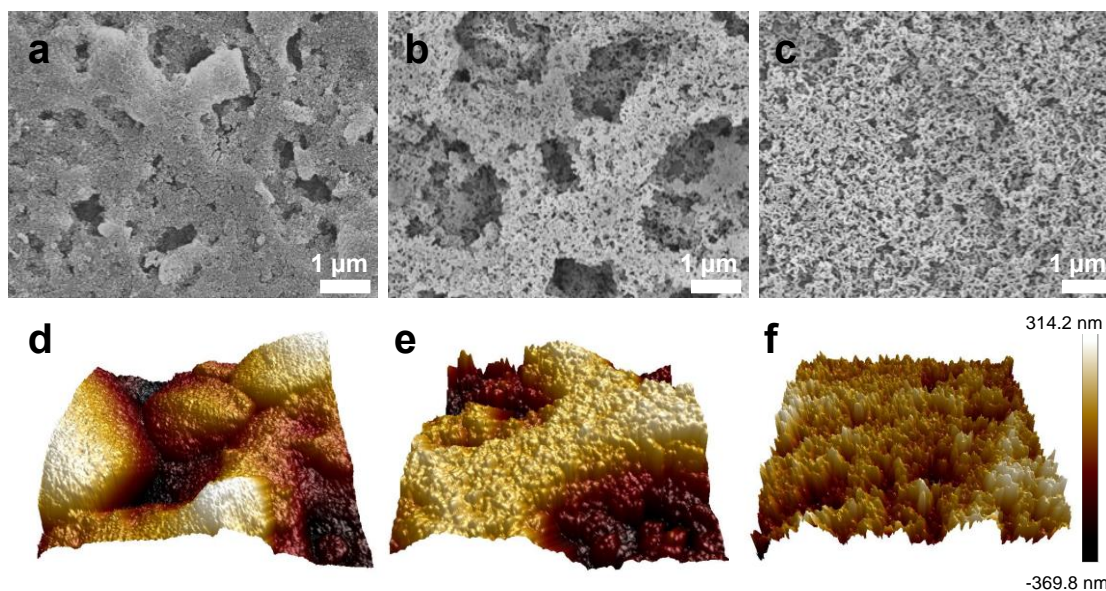


Figure 2. 9 (a-c) Top-view SEM images and (d-f) AFM images of the spherical SiO₂ NPs coating (a, d), SiO₂ nanochain coating (b, e), and PAA grafted SiO₂ nanochain coatings (c, f), respectively.

Table 2. 1 Global and Local Roughness Obtained from AFM Scan in Terms of the Root Mean Squared Roughness (R_{rms}), Arithmetic Average Roughness (R_a), and Maximum Roughness Depth (R_{max}) of the Coatings

Roughness, nm	Global			Local		
	R_{rms}	R_a	R_{max}	R_{rms}	R_a	R_{max}
Spherical NP Coating	367.0	291.0	1753.0	39.1	30.4	259.0
Nanochain Coating	320.0	282.0	1358.0	40.0	31.2	270.0
PAA-grafted Nanochain Coating	90.6	69.2	757.0	68.1	53.2	423.0

Now we turn our attention to underwater superoleophobicity of these surfaces (see setup in Figure 2.6d) and investigate the importance of the coating morphology and surface chemistry. Pre-wetting a porous surface with water is essential for superhydrophilic surfaces to achieve underwater superoleophobicity, which leads to the formation of water-impregnated surface.¹⁷ Figure 2.6e shows all NP coated surfaces are superhydrophilic, regardless of NP morphology or surface chemistry as water spreads completely on a clean smooth hydrophilic SiO_2 surface. To test underwater oil repellency, we choose 1,2-dichloroethane (DCE) because of its high density (1.25 g cm^{-3}) so the droplet will not float away underwater, low surface tension ($\gamma = 33.3 \text{ mN m}^{-1}$), and low DCE-water interfacial

tension. As shown in Figure 2.6e and 2.6f, on a silicon wafer, the static underwater oil contact angle (OCA) is no more than 150° even after oxygen plasma cleaning. In comparison, all NP coatings have static OCA greater than 160° . Even when the DCE drop is forcefully compressed against the coating underwater by pushing down the dispensing needle attached to the DCE drop, the OCA remains very high with minimal contact between the droplet and the surface (Figure 2.10). When the pores in these assemblies are filled with water, an oil droplet sits on top of a composite, textured surface (*i.e.*, an underwater Cassie-Baxter state^{7,81,97,106}). What distinguishes the nanochain coatings from the spherical NP coating is the contact angle hysteresis (CAH) as shown in Figure 2.6f. Coating the pristine silicon wafer with spherical SiO_2 NPs reduces CAH from 26.1° to 16.2° . However, a significant reduction of CAH is observed after coating with either pristine nanochains (0.6°) or PAA-grafted nanochains (0.4°) due to the large porosity provided by the chain morphology.

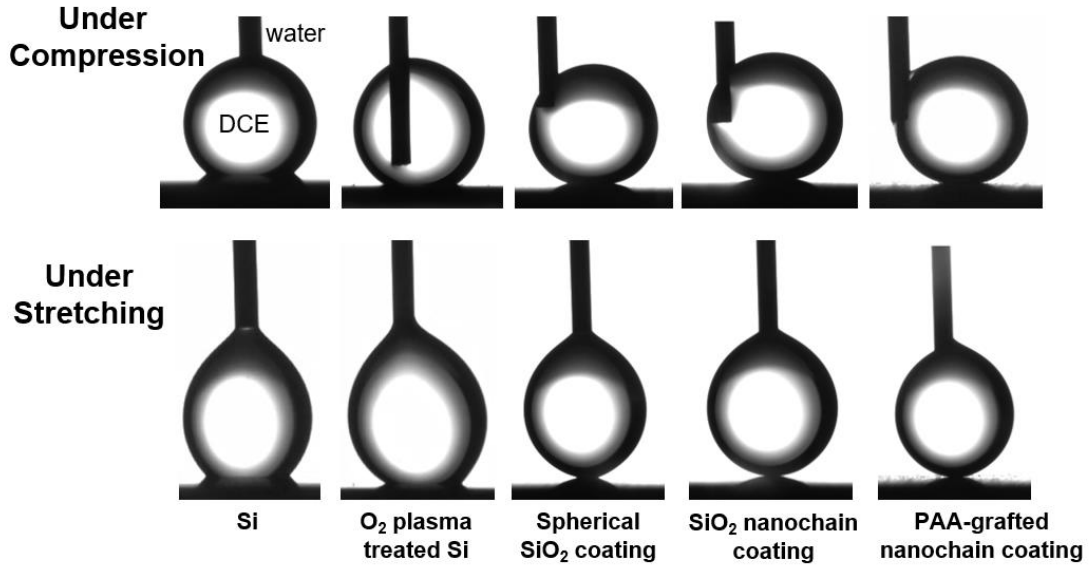


Figure 2. 10 Optical images of the dichloroethane (DCE) pendent drops underwater on different coating surfaces under compression (top) and stretching (bottom). (Top) the pendent drop is continuously lowered towards the surface until the DCE drop wets the surface or the needle slips to the side of the DCE drop. (Bottom) The DCE drop is pulled away from the surface, showing different degrees of deformation.

We estimate the adhesion hysteresis, ΔW , which represents the difference between the energy gained from two surfaces making a contact and the work of adhesion from separating the surfaces¹⁰⁷

$$\Delta W = \gamma_{ow} \cdot (\cos \theta_{adv} - \cos \theta_{rec}) \quad (2-7)$$

where θ_{adv} , θ_{rec} , and γ_{ow} are the advancing and receding contact angles, and the interfacial tension of the oil-water interface, respectively. γ_{ow} of DCE-water system is measured to be 28.15 mN m^{-1} using a pendent drop of DCE in water.

Consistent with the trends of CAHs, both the PAA-grafted nanochain and the pristine nanochain-based coatings show the lowest ΔW , $\sim -0.05 \text{ mN m}^{-1}$, with statistically insignificant difference, as shown in Figure 2.6g. The negative sign represents the attraction between the oil droplet and the substrate surface. The results are at least two orders of magnitude lower than those from the pristine silicon wafer surface (-13.25 mN m^{-1}) and the spherical NP coating (-3.66 mN m^{-1}). These results highlight the importance of large porosity and fractal-like pore morphology introduced by the nanochain assemblies, facilitating water imbibition and trapping within the nanopores to form a continuous water lubricating layer that repels oil, similar to the effect of slippery liquid-infused porous surfaces (SLIPS), which trap oil to repel water or ice.¹⁰⁸

Because of the high surface energy of hydrophilic surfaces, they can be easily fouled. Once fouled, especially on a structured surface with nanopores, the wetting transition from the Cassie-Baxter state to the Wenzel state is typically irreversible,¹⁰⁹ thus limiting their uses in practical applications. Significant energy or work is necessary to overcome capillarity to push the infiltrated liquid out of nanopores.¹¹⁰ The pressure that needs to be overcome to replace one type of fluid trapped in a pore, which is significantly smaller than the capillary length (1.7 mm in our case), with another fluid is dominated by capillary pressure and can be expressed as¹⁹

$$p = \frac{2\gamma \cos \theta}{r} \quad (2-8)$$

where γ , θ , and r are the interfacial energy of the interface (oil-water interface in our case), the contact angle of the wetting fluid (water in our case), and the pore radius. Assuming

that the pores in our coatings are approximately 100 nm (according to SEM images seen in Figure 2.8), we estimate the critical capillary pressure^{111,112} is at least 824 kPa or 8 atm. It would be difficult to reach such a high pressure by simply submerging oil-fouled surfaces in a shallow body of water.

Table 2. 2 Summary of the abbreviations of the tested samples.

Abbreviated Sample Name	Description
Si	Pristine silicon wafer
O ₂ -t-Si	Oxygen plasma treated silicon wafer
s-SiO ₂	Spherical silica NPs spray coated on silicon wafer, fresh prepared
c-SiO ₂	Silicon wafer spray-coated with silica nanochains, fresh prepared
PAA-c-SiO ₂	Silicon wafer spray-coated with PAA-grafted silica nanochains, fresh prepared
c-SiO ₂ aged	Silicon wafer spray-coated with silica nanochains, stored in air for 2 weeks
PAA-c-SiO ₂ aged	Silicon wafer spray-coated with PAA-grafted silica nanochains, stored in air for 2 weeks
PAA-c-SiO ₂ calcinated	Silicon wafer spray-coated with PAA-grafted silica nanochains, calcinated at 400 °C for 4 hours
PAA-s-SiO ₂	Silicon wafer spray-coated with PAA-grafted spherical silica NPs, stored in air for 2 weeks
PAA-Si	Silicon wafer directly grafted with PAA, stored in air for 2 weeks

To test the possibility to recover underwater oleophobicity on various types of silica-based coatings (see the list in Table 2.2), we intentionally foul the surfaces by spreading oil drops onto them. To image the degree of oil fouling and recovery in the NP coatings by SEM, we introduce a photopolymerizable monomer, trimethylolpropane ethoxylate triacrylate (ETPTA), which not only has surface tension of 36.3 mN m⁻¹ close to that of DCE (33.3 mN m⁻¹) but also can be solidified through photopolymerization, allowing for direct visualization of oil entrapped in the coatings using SEM. Except for the PAA-grafted

nanochain coating, all other samples are freshly prepared and treated with oxygen plasma to minimize the effect of contamination. ETPTA droplets readily spread on all surfaces (OCA $\sim 0^\circ$) because of their low surface tension and the high surface energy of the silica-based surfaces. After 30 s, ETPTA completely infiltrates the coating. We then submerge the contaminated surfaces 2 cm below water. The change of OCAs is monitored over time while the coating remains in water (see illustration of experiment setup in Figure 2.11a). As shown in Figure 2.11b, the spread ETPTA dewets and the films become sessile drops on all coating surfaces, reaching finite OCAs over a certain period of time. However, the dewetting behaviors and kinetics vary significantly depending on the coating morphology and chemistry.

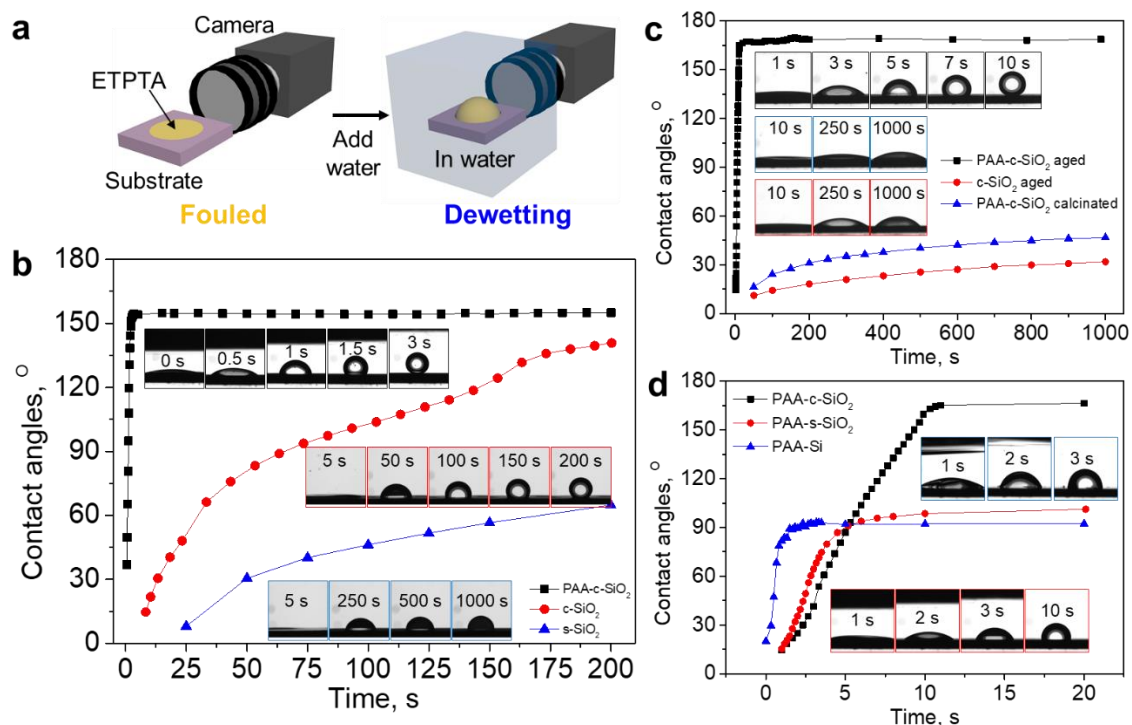


Figure 2. 11 (a) Schematics of the setup to investigate anti-fouling effect on oil-spread coatings. (b) OCA of ETPTA changes with respect to time during dewetting for spherical SiO₂ NP coating (s-SiO₂), SiO₂ nanochain coating (c-SiO₂), and PAA-grafted SiO₂ nanochain coating (PAA-c-SiO₂) with (inset) optical images. (c) OCA of ETPTA changes with respect to time submerged in water on aged PAA-grafted SiO₂ nanochain coating (PAA-c-SiO₂ aged), aged SiO₂ nanochain coating (c-SiO₂ aged), and calcinated PAA-grafted SiO₂ nanochain coating (PAA-c-SiO₂ calcinated). (d) OCA of ETPTA changes with respect to time submerged in water on aged PAA-c-SiO₂, PAA-grafted spherical SiO₂ NP coating (PAA-s-SiO₂), and silicon surface grafted with PAA (PAA-Si).

To quantitatively analyze the dewetting behaviors, we use a decay function

$$1 - \frac{\theta_t}{\theta_\infty} = A \cdot \exp\left(-\frac{t}{\tau}\right) \quad (2-9)$$

where θ_t is the OCA as a function of time, and θ_∞ is the steady-state OCA after immersing in water over a long period of time (typically > 500 s). A is a constant, t is the time. τ is the characteristic timescale in the dewetting process. The fitting results are summarized in Figures S6 and S7 and Table 2.3. Among the 3 types of samples tested in Figure 2.11b, the two SiO₂ nanochain coatings can completely recover from the fouled state to the superoleophobic state with underwater OCAs greater than 150°. Impressively, ETPTA spontaneously and completely dewets on PAA-grafted nanochain coating and OCA reaches > 150° less than 5 s, whereas at least 300 s is needed for the pristine nanochain coating. The dewetted droplets of ETPTA and other low surface energy oils, including hexadecane ($\gamma = 27.47 \text{ mN m}^{-1}$ at 20°C), decane ($\gamma = 23.83 \text{ mN m}^{-1}$ at 20°C), octane ($\gamma = 21.62 \text{ mN m}^{-1}$ at 20°C), hexane ($\gamma = 18.43 \text{ mN m}^{-1}$ at 20°C), and silicone oil, are highly mobile that they can easily roll off from the surface, confirming the ultra-low oil adhesion and a complete transition from Wenzel state to Cassie-Baxter state on PAA grafted nanochain coating upon introduction of water. Without PAA grafting on nanochains, however, even after oxygen plasma cleaning (10 min), it takes more than 300 s for ETPTA to completely dewet (OCA ~ 150°). In sharp contrast, ETPTA on spherical NP coating does not completely dewet (see Figure 2.11b); after 900 s the dewetting process levels and OCA reaching constant, ~ 88°. Figure 2.12-2.14 summarize the fitting, the θ_∞ and the time it needs to almost reach θ_∞ during ETPTA dewetting, $t_{0.99}$.

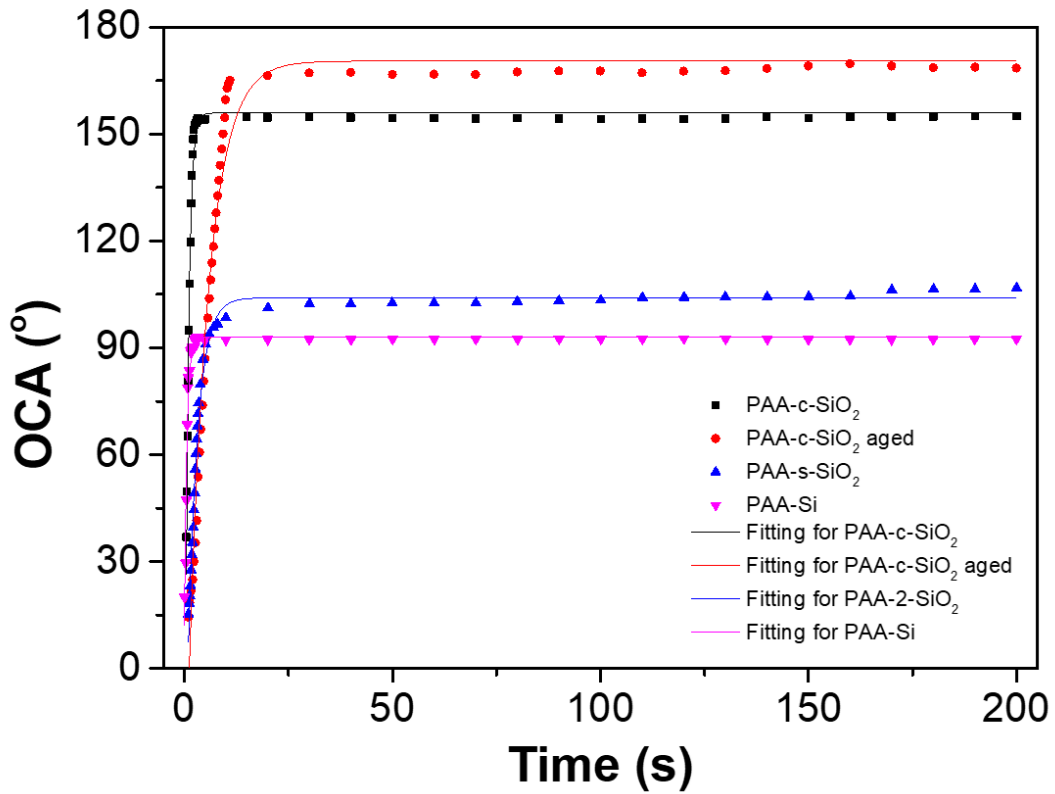


Figure 2. 12 Dewetting behaviors of ETPTA on various PAA grafted surfaces, including PAA-grafted nanochain coating (PAA-c-SiO₂), aged PAA grafted nanochain coating (PAA-c-SiO₂ aged), PAA-grafted spherical NPs coating (PAA-s-SiO₂), and PAA-grafted silicon wafer (PAA-Si) as measured by oil contact angle (OCA) vs. time. The solid line is data fitting using a decay function: $1 - \frac{\theta}{\theta_{\infty}} = A \cdot \exp\left(-\frac{t}{\tau}\right)$.

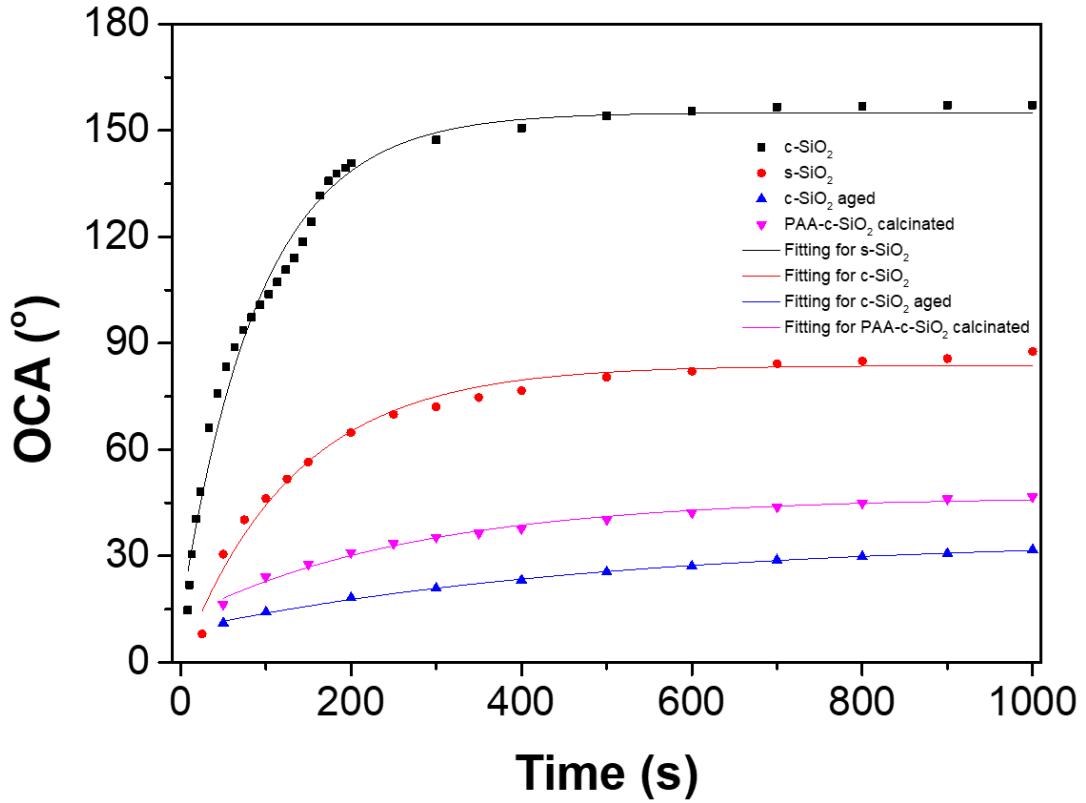


Figure 2. 13 Dewetting behaviors of ETPTA on pristine nanochain coating (c-SiO₂), spherical NPs coating (s-SiO₂), aged nanochain coating (c-SiO₂ aged), and calcinated PAA-grafted nanochain coating (PAA-c-SiO₂ calcinated) as measured by oil contact angle (OCA) vs. time. The solid line data fitting using a decay function: $1 - \frac{\theta}{\theta_{\infty}} = A \cdot \exp\left(-\frac{t}{\tau}\right)$.

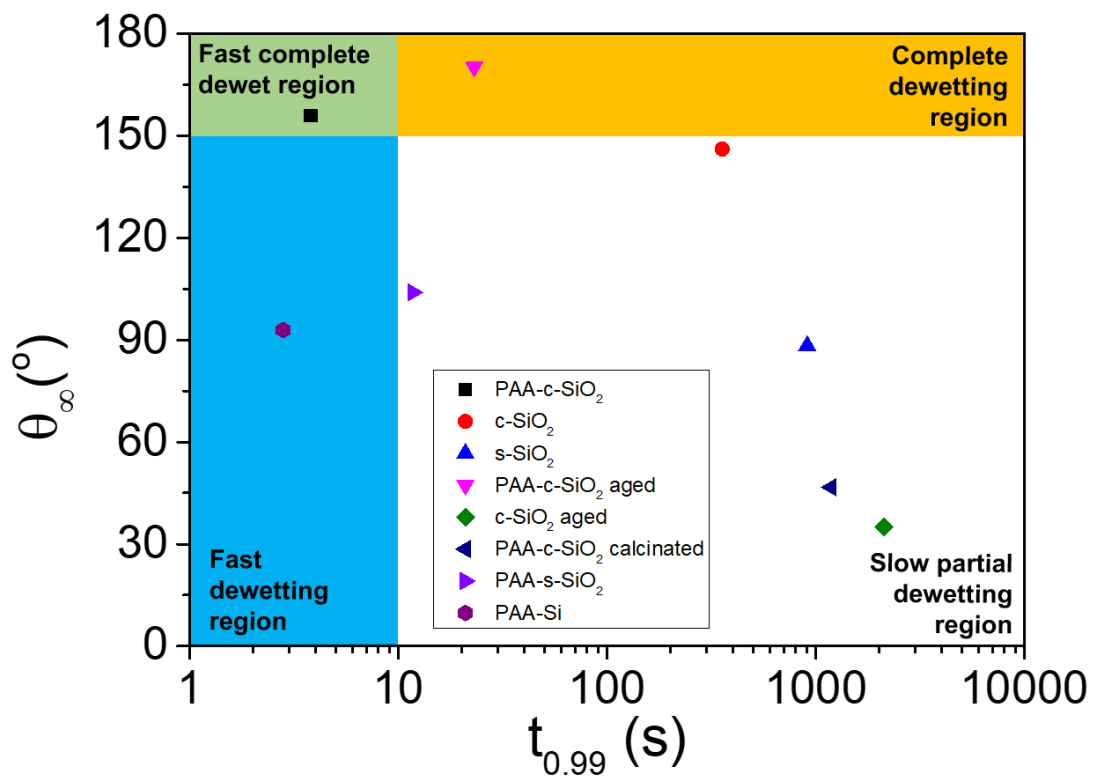


Figure 2. 14 The saturated oil contact angle (θ_{∞}) when ETPTA dewetting stops vs. time needed to reach 99% of its θ_{∞} , $t_{0.99}$, on different coating surfaces.

Table 2. 3 Parameters and R-Squared Values for Fitting the Decay Function eq 2-9

Coatings	A	τ	$CA_{sat}, ^\circ$	R^2	$t_{F=0.99}, s$
PAA-c-SiO ₂	1.61	1.324	155.9	0.984	3.8
c-SiO ₂	0.93	0.013	146.1	0.978	355.2
s-SiO ₂	0.91	0.005	88.3	0.948	907.2
PAA-c-SiO ₂ aged	1.29	0.212	170.2	0.976	23.0
c-SiO ₂ aged	0.74	0.002	35.0	0.998	2117.4
PAA-c-SiO ₂ calcinated	0.74	0.004	46.7	0.988	1183.3
PAA-s-SiO ₂	1.42	0.425	104.0	0.990	11.7
PAA-Si	0.87	1.589	92.9	0.948	2.8

We further investigate anti-oil fouling behaviors on aged samples, which are left in air for two weeks prior to the wettability recovery test as described above. As shown in Figure 2.11c, EPTPA spontaneously dewets on the aged PAA-grafted nanochain coating within 10 s, reaching OCA $> 150^\circ$. However, ETPTA can no longer completely dewet on the aged, pristine nanochain coating even after more than 2000 s and the final OCA is only $\sim 35^\circ$, suggesting some ETPTA is still trapped in the coating. This likely is due to the contamination of the high surface energy silica surface by air-borne pollutants. To confirm the role of PAA, we remove PAA from the surface of the SiO₂ nanochains by subjecting the coating to 400 °C for 4 hours (see details in Experimental Section).¹¹³ Not surprisingly, the calcined sample behaves much like the pristine nanochain coating; EPTPA gradually dewets on coating surface but stops when reaching OCA of $\sim 46^\circ$ after 1000 s; the saturated OCA is higher than that from pristine nanochain coating, possibly due to residue carbon left on SiO₂ surface.

Clearly PAA grafting is critical. We then investigate the role of nanochain morphology by grafting the same PAA onto spherical SiO₂ NPs and the silicon wafer for the same dewetting experiments. As shown in Figure 2.11d and Table 2.3, ETPTA cannot completely dewet on the aged PAA-grafted spherical NP coating and PAA-grafted Si wafer under water, although the dewetting performance is dramatically improved, reaching equilibrium OCAs of ~ 104° and 93°, respectively, after 12 s and 3 s. The latter is faster possibly because there is no capillary resistance to ETPTA dewetting on a flat surface.

Since ETPTA is photopolymerizable, we can observe the presence of oil within the coatings before and after water immersion by photocuring. As seen in Figure 2.15a, ETPTA completely fills the pores of the PAA-grafted nanochain coatings upon spreading on the surface. This is the same case for spherical NP coating (Figure 2.16a) pristine nanochain coating (Figure 2.16b). After submerging under water for 1h, the sample is taken out for UV curing. As seen from Figure 2.15b, there is no trace of ETPTA in the coating, which appears identical to the as-deposited one shown in Figure 2.6c. In contrast, cracks and significant surface charging effect is observed in the case of spherical NP coating (Figure 2.16c) and pristine nanochain coating (Figure 2.16d), and a thin layer of polymer can be seen on top of the coating. As we discussed earlier, expulsion of the trapped ETPTA from the nanopores, especially when pore size is small, requires a lot of work. Cracks may have formed due to polymerization-induced stress, and the crosslinked ETPTA is electrically insulating, inducing significant charging during SEM imaging. These results unequivocally demonstrate the importance of having both the fractal, nanoporous morphology obtained via spray coating of the nanochains and the appropriate surface

chemistry, here hygroscopic PAA brushes, to enable ultrastable and rapid recovery of underwater superoleophobicity.

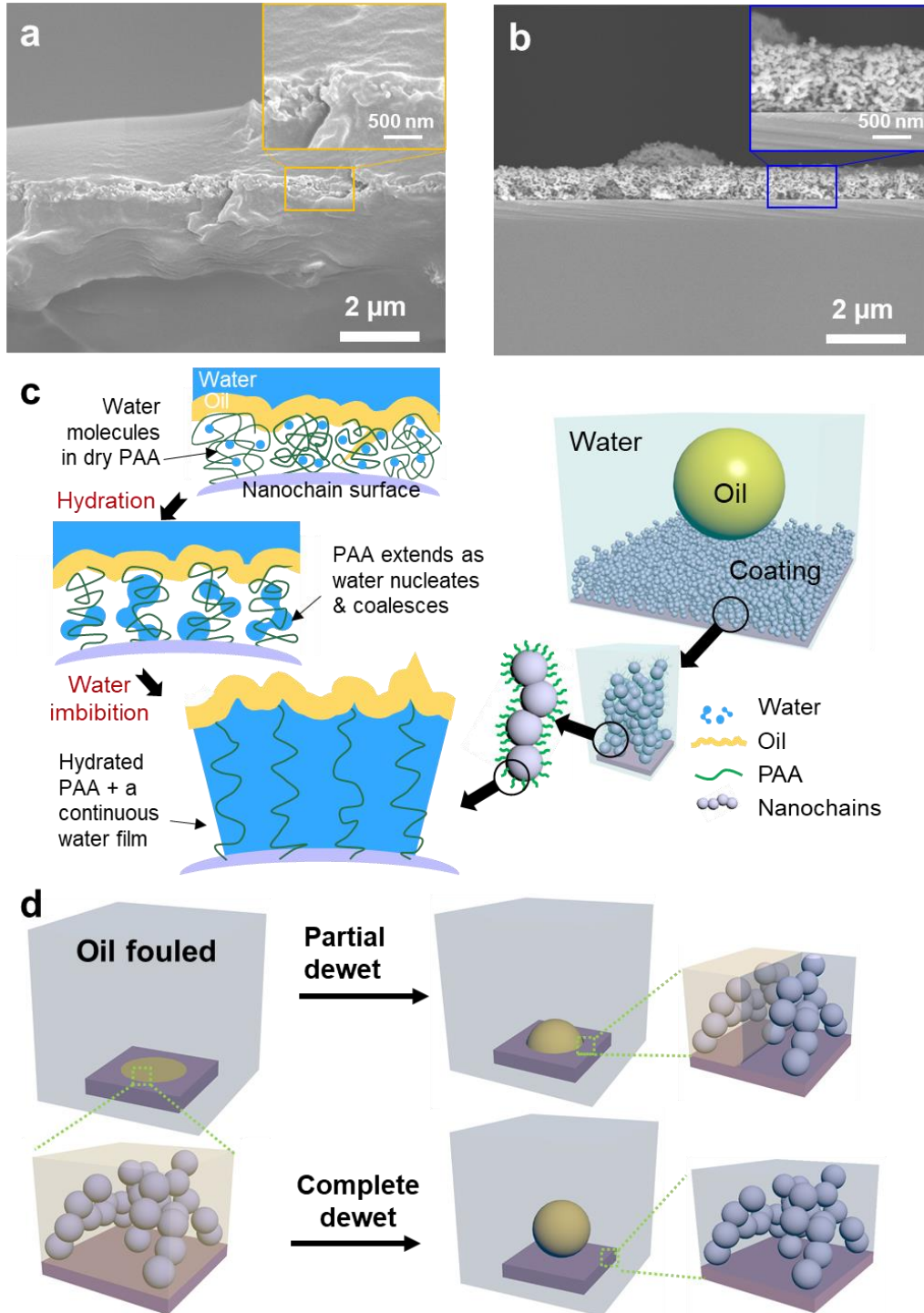


Figure 2. 15 Cross-sectional SEM images of PAA-grafted SiO₂ nanochain coating after fouled by ETPTA (a) at the beginning and (b) after submerging in water for 1 h, followed

by UV curing. (c) Zoomed-in representation of a single nanochain surface inside the oil-fouled region of the substrate. Hydration and imbibition of water molecules into nanopores between PAA-grafted SiO_2 nanochains lead to spontaneous dewetting of the ETPTA from the coating surface. (d) Schematic illustration of ETPTA wetting transition on PAA-grafted SiO_2 nanochain coating from the fouled state to the dewetted state. Note: macroscopically only part of the substrate is covered by the oil drop.

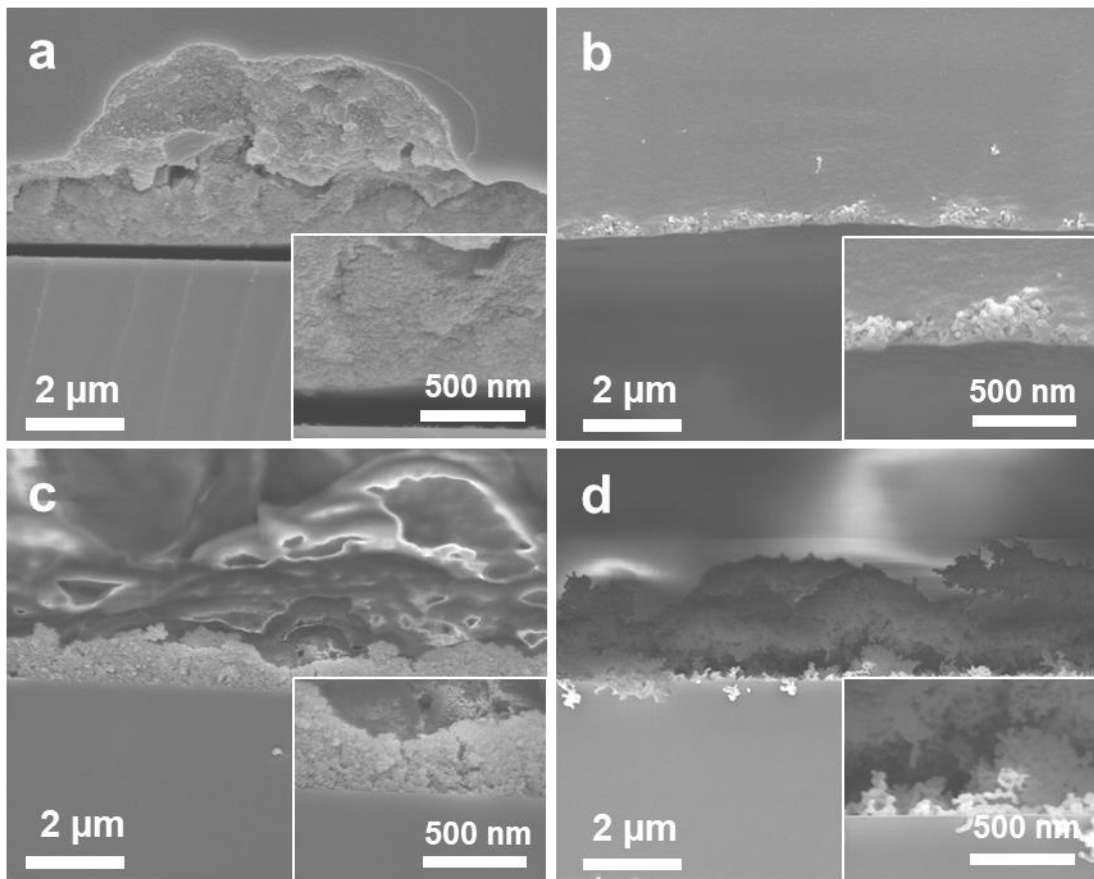


Figure 2. 16 Cross-sectional SEM images of NP coatings (a,b) fouled by ETPTA for 30 s, followed by UV curing, and (c,d) fouled by ETPTA for 30 s, submerged in water for 1 h, taken out, followed by UV curing. (a,c) Spherical SiO_2 NP coating and (b,d) pristine SiO_2 nanochain coating. Inset: zoomed-in SEM images.

It has been suggested from a recent computational study on transition from the Wenzel state to the Cassie-Baxter non-wetting state on nanostructured surfaces that nucleation of a wetting fluid (air in their case), formation of a large vapor-liquid interface (water-air in their case), and the depinning of that interface from surface features as it expands are critical requisites to enable a spontaneous recovery of superhydrophobicity in air.¹¹⁴ In our system, ETPTA is the dewetting fluid and water is the wetting fluid. Due to the intrinsic hygroscopic nature of PAA, there will always be some water molecules surrounding the nanochains even in the ambient condition^{62,115} (see Figure 2.15c). More importantly, PAA grafts provide an ideal environment for water nucleation, which could induce fluid density fluctuation leading to the reduction of the energy barrier for oil dewetting. When the fouled PAA grafts come in contact with bulk water, they hydrate rapidly in an extended chain conformation to maximize the contact with water molecules. PAA also facilitates depinning of the oil-water interface from the nanochain surface, leading to the flooding of the entire structure with water (Figure 2.15d). Although oil dewetting from zwitterionic polymer-grafted planar surfaces^{62,85} and anti-oil fouling effect from zwitterionic polymer-grafted microfibers¹¹⁶ have been demonstrated, similar effects have not been explored on nanostructured surfaces grafted with weak polyelectrolytes such as PAA nor the effect of aging. Even though the study shows the sodium polyacrylate-grafted poly(vinylidene fluoride) (PAAS-g-PVDF), which is formed through ionization of PAA-grafted PVDF using sodium hydroxide, is able to achieve underwater superoleophobicity, the pristine PAA-grafted PVDF without the base treatment does not have anti-oil fouling effect (failing to expel and lift the oil) underwater and shows strong oil adhesion.⁵⁴ Our work

demonstrates that anti-oil fouling actually can be achieved by combining PAA grafts and nanochains morphology, without using the ionization treatment of sodium hydroxide.

Durability of the coating is critical for practical applications. It is highly desirable for the coating to retain its wetting property over time. Earlier we have shown that the PAA-grafted nanochain coating can maintain its oil repellency and oil-lifting capability towards ETPTA after storage in air for at least two weeks. Since our coating is superhydrophilic and most likely will be used under water, it is also important to show its durability in such an environment. To further test the underwater durability of the coating, a shear resistance test is performed (see Experimental section for details). As seen in Figure 2.17, the coating retains underwater superoleophobicity (dichloroethane contact angles underwater $> 165^\circ$) for more than 168 hours subjected to continuous shearing, mimicking possible conditions in practical applications. The results are comparable to those reported in literature¹¹⁷ obtained from a different type of NP coating.

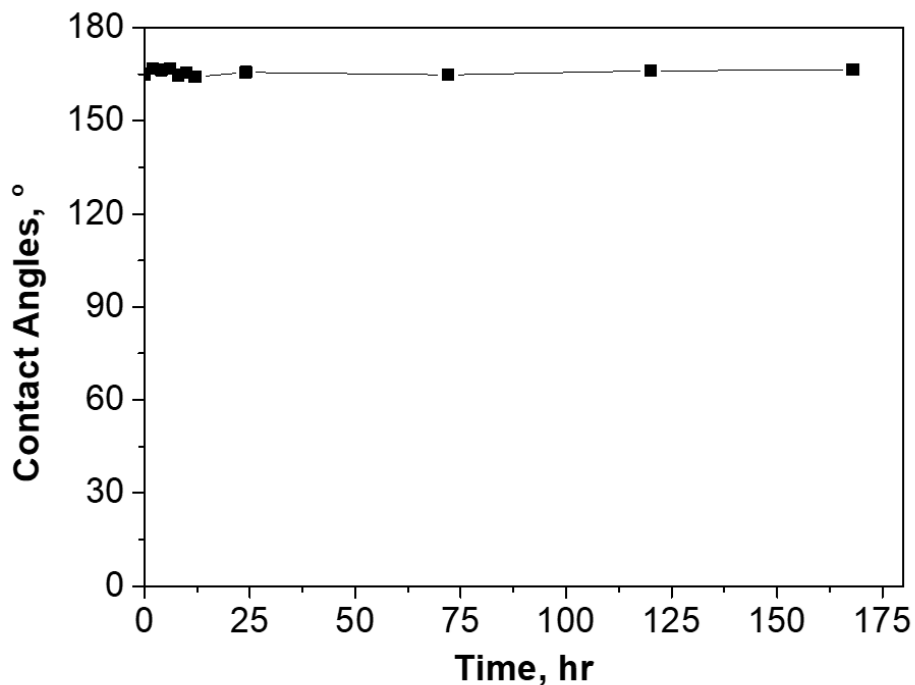


Figure 2. 17 Dichloroethane contact angles on the PAA-c-SiO₂ coated Si surface under water with respect to the time the coating is subjected to a stirred water environment.

2.4 Conclusion

In summary, by taking advantage of the unique architecture of SiO₂ nanochains, we create a ultrastable superhydrophilic/underwater superoleophobic coating by spray coating of PAA-grafted SiO₂ nanochains. Among coatings of similar underwater superoleophobicity, the nanochain coatings with and without PAA show ultra-low underwater adhesion hysteresis, likely due to their large porosity and fractal morphology. More importantly, PAA-grafted nanochains can recover the underwater superoleophobicity spontaneously

(within 10 s) from an oil fouled state simply by submerging the coating in water, which is not possible with other coatings. Our approach is simple yet versatile and scalable to manufacture superhydrophilic surfaces. The study of separate and combined roles of surface topography, porosity, and surface chemistry to anti oil-fouling behaviors offers new insights into creating highly stable coatings and efficient membranes for oil-water separation over a large area. A more detailed investigation of the molecular weight and grafting density of polymer brushes will be pursued in the future to further our understanding of the oil-dewetting mechanism as well as durability of the coatings when subjected to harsh environment conditions.

CHAPTER 3. Drastic Enhancement of Oil/Water Separation through Polyelectrolyte-grafted Silica Nanochain Coatings

3.1 Introduction

Fresh water has become increasingly scarce. However, large amount of them is still wasted each year through contamination by oily contents such as hydraulic fracturing.¹¹⁸ One direct solution to tackle this problem is to perform oil/water separation to recover clean water from its oily mixture. Conventional separation methods such as distillation,⁶³ flotation,¹¹⁹ and electro-coalescence¹²⁰ have drawbacks such as high cost, low efficiency, and secondary pollution. Therefore, membrane filtration to separate oil/water mixtures offers a very promising approach due to its high selectivity and low energy consumption.⁶⁵ However, there one of the major challenges using traditional membranes for oil/water separation is the fouling of the membrane caused by the accumulation of oil on the membrane surface over repeated uses.¹²¹ This blocks pores on the membrane, which are important to water transport, and ultimately leads to reduction of separation efficiency.¹²²

This challenge drives extensive efforts to fabricate a variety of filtration membranes with anti-fouling properties by introducing superwettability on membrane surfaces. Superhydrophilic membranes is ideal for this case, because its high water affinity facilitates water spreading and permeating through membranes, which could lead to underwater superoleophobicity that will greatly reduce membrane fouling. Most superhydrophilic membranes are composed of two parts: a microporous substrate as the mechanical support and a thin layer of nanoporous, superhydrophilic materials on top to provide select

permeation and anti-fouling. The common support substrates are metal meshes, such as stainless steel mesh,^{123–125} copper mesh,¹²⁶ nickel foam,¹²⁷ and nickel mesh,¹²⁸ and porous polymer membranes made from, e.g., cotton,¹²⁹ poly(vinylidene fluoride),¹²² and polyurethane.¹³⁰ To introduce superhydrophobicity, a thin layer of inorganic materials such as nanostructured silica,^{50,52,124} titanium oxide,¹³¹ graphene oxide,¹²⁵ zeolite,¹³² palygorskite,¹²⁶ and nickel oxide^{127,128} and polymers such as poly(acrylic acid),^{31,33,54} cellulose,¹²⁹ and hydrogels.^{122,130} are deposited on surface via spray coating,^{32,126} dip coating,¹²⁵ phase inversion,^{33,133} electrospinning,³⁴ laser-induced ablation,¹²³ and heat,¹²⁸ hydrothermal,^{124,127} and other chemical treatments.^{129,130}

Thin coatings formed from assemblies of silica (SiO₂) nanoparticles (NPs) have been shown as a simple and versatile approach to introduce surface structures to achieve superhydrophilicity.^{49–52} In particular, chained silica NPs are shown as an interesting type of nanomaterials whose assembly could dramatically increase surface roughness and porosity.^{45,46} Recently, our group has grafted polyelectrolytes on chained SiO₂ NPs,³² and demonstrated resilient underwater superoleophobicity for anti-fouling. However, the coatings were fabricated on smooth silicon wafers as a proof-of-concept to understand the combined roles of polyelectrolyte and chain morphology. For practical applications, this thin coating should be put on microporous membranes as substrates. It remains to investigate whether the nanochain coating can stand atop of microporous membranes, or will block them, how the combination of nanopores and micropores will affect the membrane filtration performance in terms of permeation efficiency and flux, and whether the membrane can maintain underwater oil repellency. Current literatures often overlook

the trans-membrane pressure and the breakthrough pressure. For examples, superhydrophilic membranes made from paint brushing Michael addition reaction treated aloe vera mucilage onto polyurethane fabrics can separate stratified oil/water mixtures with high separation efficiency of 97%, but the separation flux and breakthrough pressure were not reported.¹³⁰ Membranes made from spray coating of corn straw powders onto cotton fabrics also separate oil/water emulsions with high efficiency of 98%, but the transmembrane pressure and breakthrough pressure are unknown.¹³⁴ In the most recent reviews on oil water separation using membrane with special wettability, most flux are reported in unit of $\text{L}\cdot\text{h}^{-1}\text{ m}^{-2}$, where the transmembrane pressure and breakthrough pressure information are not included.⁶⁵ To achieve high flux, the transmembrane pressure and breakthrough pressure, which are two key factors that determines the filtration flux, should be studied more. The mechanical robustness of the ensemble of the bilayers is also important, which could allow for application of a high pressure during the separation.

In this work, we spray coat chain-like silica NPs (referred as SiO_2 nanochains) grafted with poly(acrylic acid) (PAA), which were synthesized according to our previous study,³² onto three different types of porous support substrates, including track-etched polycarbonate (PC) membrane, mix cellulose ester (MCE) membrane, and stainless steel (SSM) mesh. Here, spray coating offers an efficient way to modify the membrane surface, both surface topography and surface chemistry. All coated membranes have shown greatly improved hydrophilicity (water contact angle $< 30^\circ$) and underwater oleophobicity (underwater dichloroethane contact angle $>150^\circ$). The improved surface wettability enhances the filtration efficiency for both oil/water free mixtures and oil-in-water (OIW) emulsions. The

coated SSM performs the best for separating oil/water free mixtures, while it is the worst without NP coating. Due to the increase of breakthrough pressure and the reduction of pore size after the coating, the NP coated PC membrane outperform the one without the coating significantly for separating OIW emulsions.

3.2 Experimental Section

Materials. Whatman[®] Nuclepore[™] track-etched membranes (pore size 1 μm , polycarbonate), sulfuric acid (ACS reagent, 95.0-98.0%), n-hexadecane (ReagentPlus, 99%), methylene blue (blue dye), oil red-O (red dye), sodium dodecyl sulfate (SDS) and NOCHROMIX[®] (cleaning agent) were purchased from Sigma-Aldrich and used as received. Mixed cellulose ester membranes (pore size 1 μm) were purchased from Sterlitech. Stainless steel meshes (opening 30 μm) were purchased from TWP. 1,2-dichloroethane (DCE, $\geq 99\%$), and ethanol 200 proof (100%) were purchased from Fisher Scientific and used as received. Airbrush and air pump (Master Airbrush) were purchased from Amazon.

Spray coating of PAA-grafted SiO₂ nanochains. The synthesis of SiO₂ nanochains and PAA surface grafting steps were followed our previous study.³² Grafted nanochains were collected and dispersed in ethanol to make particle solution (0.25 wt%) by sonication. The solution was loaded into an airbrush, which was connected to an air pump (10 psi), and sprayed onto substrates (~ 10 cm away from the nozzle). For spraying on stainless steel meshes, the mesh was first soaked with a mixture of 98% sulfuric acid and NOCHROMIX[®] cleaning agent for 2 min, followed by rinse of DI water and drying before spray coating

with nanochains. There was no treatment for PC and MCE membranes before spray coating. The thickness of the coatings was kept as consistent as possible by controlling the loaded solution volume and the area of the membrane to be sprayed on.

Wettability study. Both water contact angles and underwater oil contact angles were measured based on the sessile drop method using ramé-hart (Model 200) and Biolin Scientific Attension goniometer. To measure the water contact angles, a drop of 4 μL DI water was dropped onto the substrate and the static contact angle was measured and averaged 6 sets. To measure the underwater oil contact angle, the substrate was first placed in a small cubic glass container filled with DI water to pre-wet the surface. A drop of 4 μL DCE was then dropped onto the substrate and the static contact angle was measured. To qualitatively demonstrate the adhesion/hysteresis, a drop of 4 μL DCE was dropped onto the substrate under water and the substrate was then tilted slightly ($\sim 10^\circ$) to observe whether the droplet would stick to the substrate or roll off from the substrate.

Preparation of oil/water mixtures used as separation feed stock. For oil/water free mixtures, 10 mL of hexadecane (dyed by oil red) and DI water (dyed by methylene blue) were mixed with 1:1 vol/vol by handshaking for 10 seconds right before pouring into the filtration device. For OIW emulsions, 200 mL of hexadecane and DI water were mixture with 1:99 vol/vol stabilized by surfactants (SDS, 0.3 mg/mL) by probe sonication (450 watts, 80%) for 1 min. The mixture was stable for about a week.

Oil/water filtration tests. To filter oil/water free mixtures, membranes were sandwiched between two identical glass tubes fixed by a clamp and sealed by an O-ring (Figure 3.6).

The entire setup was then fixed on a support stand vertically with the coated side of the membranes facing up. The dyed mixtures were poured into the top tube and filtrate was collected below the bottom tube. The time was recorded with the volume of the filtrate to calculate the flux. The trans-membrane pressure was calculated by measuring the height of the liquid inside the top tube. For filtering oil/water emulsions, membranes were sandwiched inside O-ring sealed membrane modules (Figure 3.1): one made from 3D-printed for low pressure and an alternative stainless steel filter holder (Whatman 1980-001) for high pressure, with one inlet and two outlets (Figure 3.6a). The inlet was connected to the feed reservoir pressurized by a nitrogen gas cylinder. The outlet on the same side of the inlet was the recycle stream going back to the feed and the other outlet on the opposite side of the membrane was the filtrate and collected in a small vial. There were two pressure gauges measuring the pressure in the feed stream and permeate stream, respectively. One pressure regulator was used to control the supplying pressure to the feed reservoir. Same as the free mixture case, the time was recorded with the volume of the filtrate to calculate the flux. The oil concentration inside the filtrate was measured using chemical oxygen demand (COD) method.

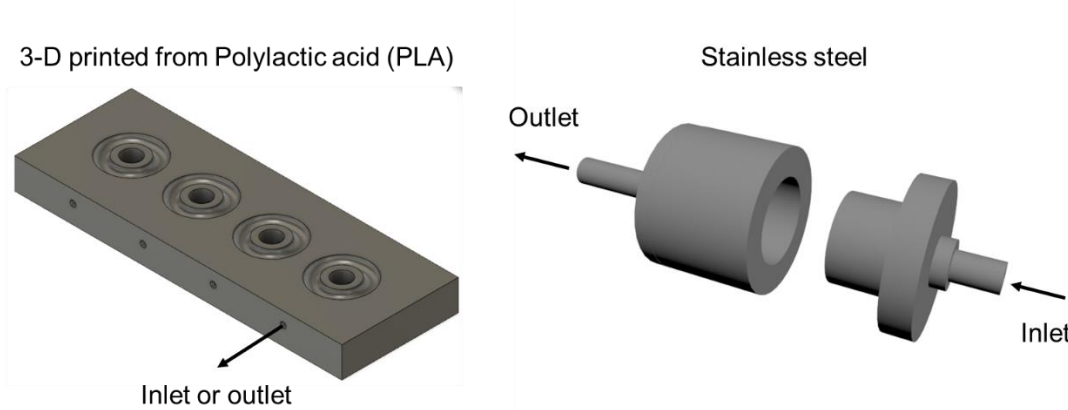


Figure 3. 1 Schematics of the membrane module used for sandwiching membranes during emulsion separation under (left) low pressure and (right) high pressure.

Measuring breakthrough pressure. Before the test, each membrane was pre-wetted by ethanol followed by DI water to ensure a completely wetting and forming of a continuous layer of water film on membrane surface. similar to the filtration experiments, the membrane was sandwiched by two glass tubes sealed by an O-ring (Figure 3.8a). Then about 5 mL of hexadecane was injected inside the top tube supported by the water pre-wetted membrane. The system was then sealed by a rubber cap. The bottom tube was still open to the atmosphere. When the experiment starts, air was injected through a needle and the pressure inside the top tube was measured by a pressure gauge. As the air continues to be pumped in, the pressure above the membrane continues to build up until it reaches the breakthrough pressure. Above the breakthrough pressure, oil was pushed through membranes and the pressure was recorded.

Characterization. Morphologies of the membranes and the coatings were characterized by scanning electron microscopy (SEM) using the JEOL 7500F HRSEM at an acceleration

voltage of 5 kV and emission current of 20 μ A. The static water contact angles and DCE contact angles in air were measured using the ramé-hart goniometer (Model 200) and Biolin Scientific Attension goniometer, respectively. The corresponding pictures capturing oil drops on coating surfaces were taken using the same goniometers. The dynamic light scattering (DLS) was performed using a Zetasizer Nano S (Marvern Instruments, UK). COD measurements are performed using the reaction digestion vial (low range 3-150 mg/L, high range 20-1500 mg/L, Hach USA), the reactor block (16 wells, Hach USA), and the spectrophotometer (DR/2000, Hach USA).

3.3 Results and Discussion

As demonstrated in Figure 3.2, membranes coated with PAA-grafted SiO₂ nanochains are made by spraying the particle solution using an airbrush (see details in Experimental Section), similar to our previous study.³² Different from spraying NPs on a smooth solid substrate, we expect variable surface topography depending on the pore size and morphology of the porous support substrates. When the pore size of the substrate is small ($\sim 1 \mu\text{m}$ in diameter), the nanochains should be able to form a continuous network above the pores without collapsing. Therefore, coating of nanochains should reduce the pore size of the integrated membrane. When the pore size of the support substrate is too large ($\sim 30 \mu\text{m}$) with respect to the particle size, sprayed nanochains should only decorate on actual substrate surfaces and does not affect the pore size of the final membranes. However, no matter which scenario, all particle coated area should have grafted-PAA exposed as shown in Figure 3.2. To demonstrate this unique feature as well as the versatility of the coating,

we used 3 different types of membranes as the porous substrates: the polycarbonate track-etched membrane (PC), the mix cellulose ester membrane (MCE), and the stainless steel mesh (SSM).

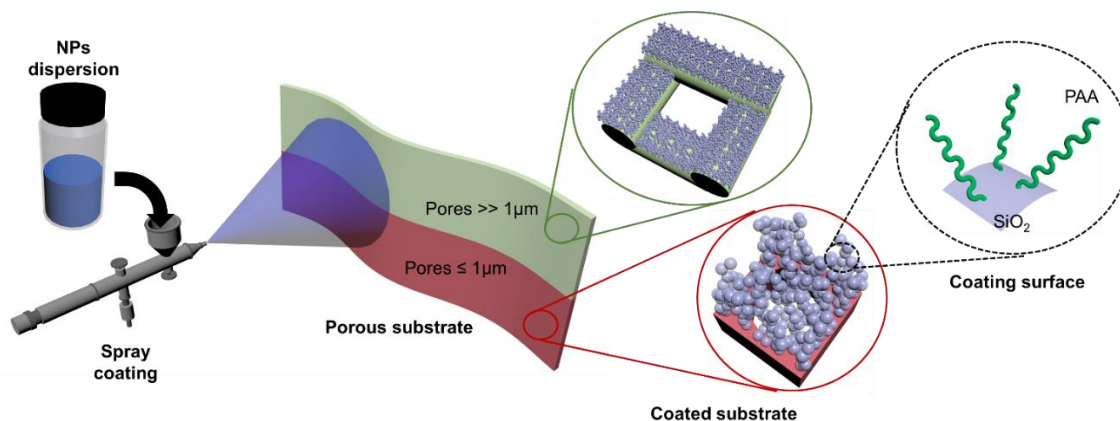


Figure 3. 2 Schematic of the fabrication steps and close-up of PAA-grafted nanochains coated the porous membranes.

Before coating, the surface of PC is relatively smooth with low pore density. The pore size is rather uniform, $\sim 1 \mu\text{m}$ in diameter (Figure 3.3a). The surface of MCE has less uniform pores, diameter ranging from sub-micron to about $2 \mu\text{m}$ (Figure 3.3c). The SSM had the largest pore size among the three. The rectangular aperture of the mesh is $\sim 30 \mu\text{m}$. Each SS wire is also about $30 \mu\text{m}$ in diameter and they are twill weaved together to form the mesh (Figure 3.3e).

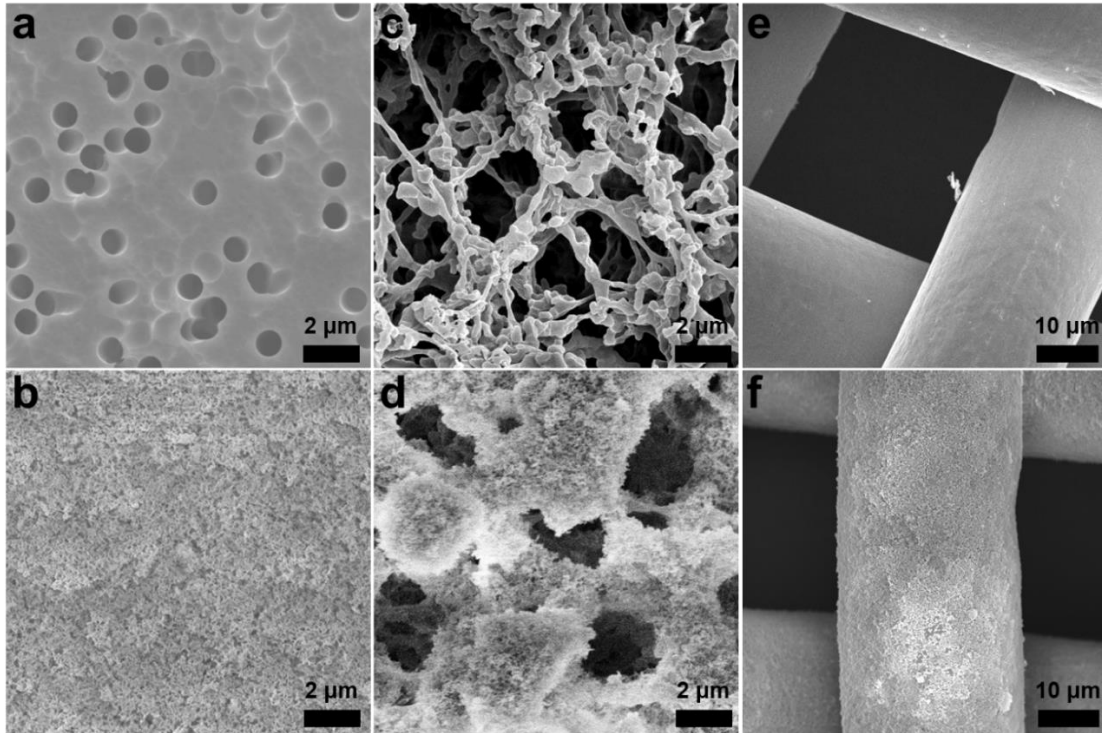


Figure 3. 3 Top-view SEM images of (a) pristine and (b) PAA-grafted nanochain coated PC, (c) pristine and (d) PAA-grafted nanochain coated MCE membranes, (e) pristine and (f) PAA-grafted nanochain coated SSM, respectively.

After the coating, the surface of PC membranes is completely covered by the nanochains (Figure 3.3b) with pore size reduced to nano-scale. The surface of MCE membranes is fully decorated by the nanochains with nanoporosity and roughness. The nanochains branches out and bridge the nearby neighbors, some smaller pores on the support substrate would be blocked by the nanochains (Figure 3.3d). The larger pores (with a diameter about 2 μm or larger) remains. The SSM is like the extreme case of the MCE. Since the pore size of the SSM is $\gg 1 \mu\text{m}$, the nanochains can only decorate the mesh surface and barely affect the pore size. However, it is worth to note that the nanochains could not only be formed on the

top surface, but also the sides, indicating the inter-stacking and bridging between nanochains. SEM images shown in Figure 3.3b, 3.3d and 3.3f confirm different morphologies after nanochain coating.

Since our goal is to enhance oil/water separation, the improved wettability on the membrane surface after the coating will be critical. According to our previous study on nanochains formed on a smooth solid substrate,³² we expect a decrease in water contact angle in air and increase in underwater oil contact angle. As shown in Figure 3.4a and 3.3c, the water contact angles (WCAs) of PC and SSM were reduced from 78° and 127° to 33° and 29°, respectively after coating. It is worth to note that WCAs is measured right after the drop contacting the surface and forming the sessile drop. WCAs eventually becomes ~ 0° due to capillary action. The pristine MCE has WCA of 0° due to its hydrophilicity of the cellulose ester and its pristine high porosity with interconnected structures. After the coating, WCA remains 0°.

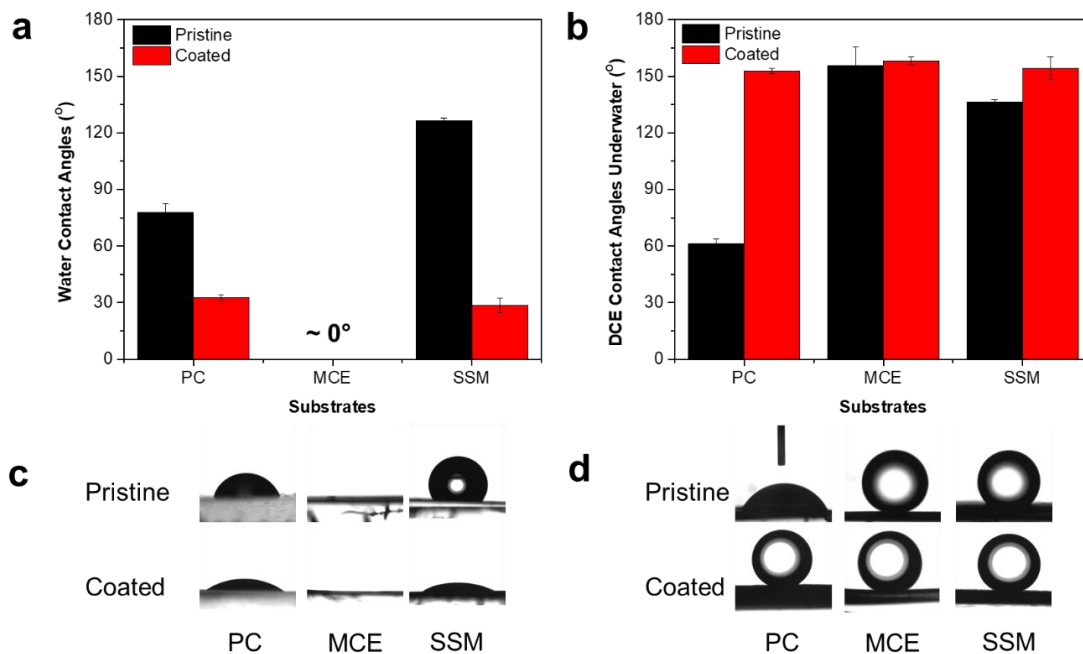


Figure 3. 4 (a, c) Water contact angles measured in air. (b, d) Underwater contact angles of dichloroethane on pristine and PAA-grafted nanochain coated PC, MCE, and SSM.

We choose the dichloroethane as the oil for the wetting tests since it has higher density than water, which is important to measure underwater contact angles. It also allows us to compare data with our previous study. From Figure 3.4b and 3.4d, the underwater oil contact angles (OCAs) of PC and SSM increased from 61° and 137° to 153° and 155° , respectively, after coating. Similar to the WCA, the OCA of MCE remained unchanged, from 156° to 158° after coating. the results confirmed that the nanochain coating could make existing commercial membranes underwater superoleophobic (e.g. in the case of PC membrane and SSM). For a membrane that is already underwater superoleophobic like MCE, coating does not alter wettability. However, the coating increased surface topography, which is an important parameter that determines wettability. As shown in

Figure 3.5, the oil drop is sticky on the pristine MCE surface despite of the high OCA. After the coating, the oil drop is mobile and easily rolls off from the membrane surface, suggesting very low contact angle hysteresis. This significant decrease of contact hysteresis and adhesion force may be contributed to the reduction of actual oil-surface contacts, benefited from the surface roughness originated from the nanochain assembly and extended hydration shell from the readily hydrated PAA grafted on the nanochains.

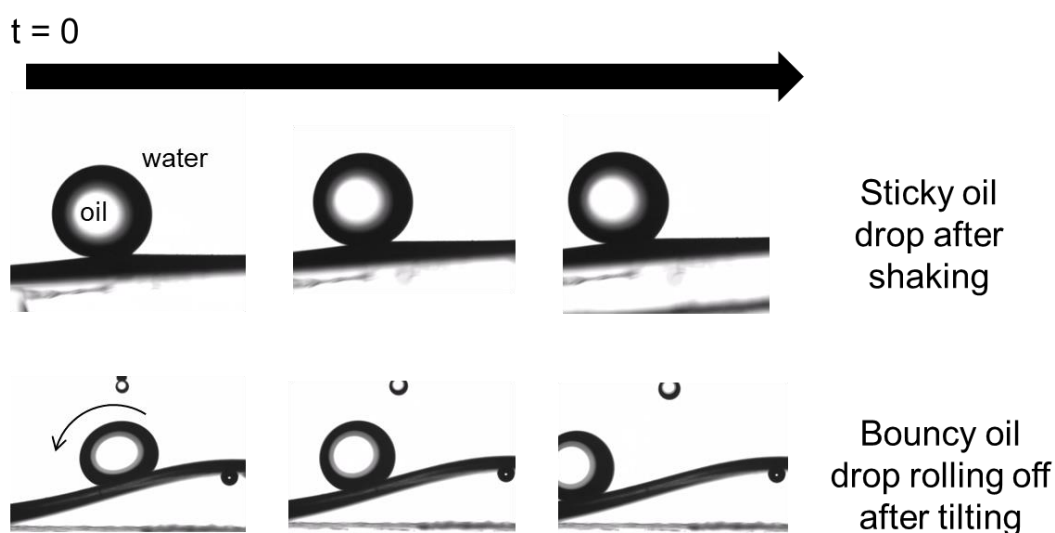


Figure 3. 5 Image captures of the sticky dichloroethane drop on pristine MCE under water during shaking (top), and the bouncy dichloroethane drop rolling off from a tilted coated MCE (bottom).

With improved surface wettability, we next test the performance of the coated membranes to filter oil/water free mixtures driven by gravity. Since oil/water free mixture is thermodynamically unstable and it usually stratify by itself at the beginning of the

separation. As shown in Figure 3.6a-d, the PC and MCE membranes can separate oil from water in the free mixtures both before and after the coating. This is not surprising since they are both hydrophilic. The flux of MCE is higher than that of PC due to higher water affinity from MCE and its interconnecting pores. However, only coated SSM could separate the oil/water free mixture (Figure 3.6e and 3.6f). Without the coating, due to the large pore size in SSM, oil followed water and easily permeated through the membrane. Since the coating barely affects the pore size of the underlying support substrate (Figure 3.3f), the ability to separate the oil/water free mixture clearly is due to the change of surface wettability introduced by the coating.

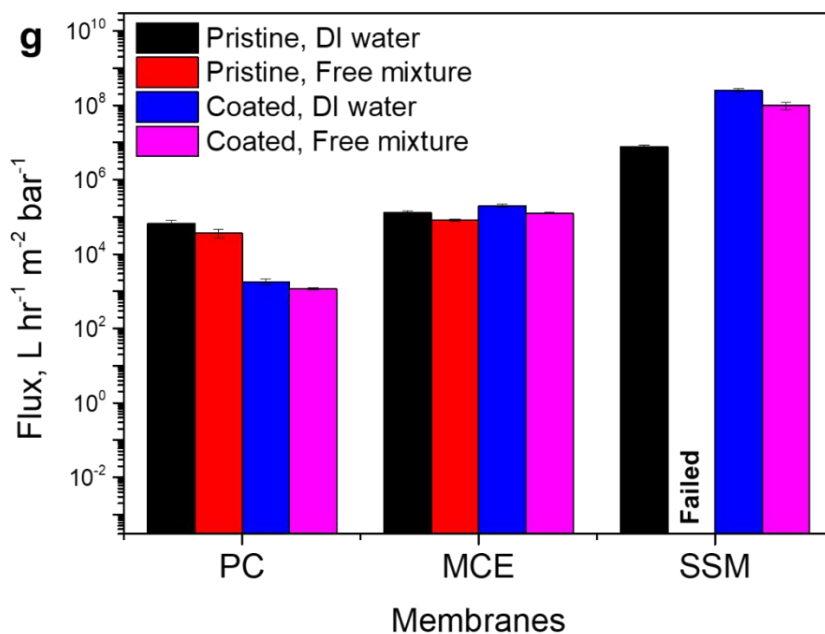
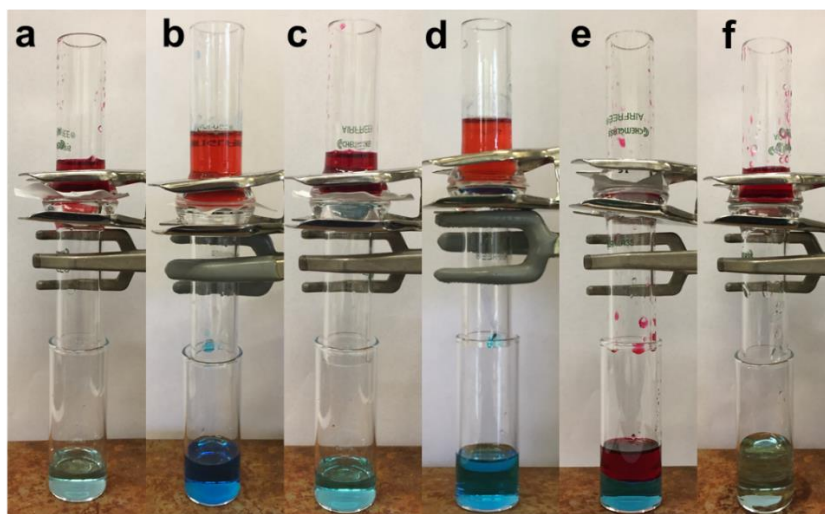


Figure 3. 6 Optical images of dead-end gravity driven filtration of hexadecane-water free mixtures on (a) pristine and (b) PAA-grafted nanochain coated PC membrane, (c) pristine and (d) PAA-grafted nanochain coated MCE membrane, (e) pristine and (f) PAA-grafted nanochain coated SSM, respectively. (g) Average flux of dead-end gravity driven filtration of hexadecane-water free mixtures.

On the aspect of flux change, the coated PC, MCE, and SSM has flux of $0.002 \text{ L m}^{-2} \text{ s}^{-1}$, $0.2 \text{ L m}^{-2} \text{ s}^{-1}$, and $19 \text{ L m}^{-2} \text{ s}^{-1}$ filtrating oil/water free mixture, respectively. Recent studies on superhydrophilic membranes reported wide range of flux from $0.0015 \text{ L m}^{-2} \text{ s}^{-1}$ to $133.4 \text{ L m}^{-2} \text{ s}^{-1}$.^{65,125–128} The coated PC and MCE is in the lower end and coated SSM is in the higher end of this flux range, and this is not surprising because coated SSM has much larger pore size. When comparing the membrane itself before and after the coating, the coating has no significant effect on MCE membranes before and after the coating. This is very interesting when it is compared with the case of PC membranes, which had similar flux before the coating. For coated PC membrane, the flux is decreased by an order of magnitude (Figure 3.6g). This flux drop is quite significant and most likely caused by the reduction of the pore size due to coating of nanochains (Figure 3.3b). According to equation (1-6) (Darcy's law), the flux is inverse proportional to the membrane thickness ($j \sim L^{-1}$) and strongly affected by the pore size ($j \sim r^4$). Therefore, when the pore size is decreased from several microns to tens of nanometers as well as when increasing the membrane thickness, the flux should decrease by at least four orders of magnitude instead of just one order. The apparent disagreement between theoretical estimation and experimental observation could be attributed to the highly porous nature of the nanochain coating, forming fractal structures. This is consistent with our previous study of nanochain coating on smooth surfaces, which is one advantage of using nanochains.³² For the MCE case, the coated membranes still preserve its large pores which contributes the majority of the water transport during filtration. Therefore, the flux is barely changed before and after the coating. The cases for SSM is even more interesting. The flux actually increases (Figure

3.6g) after the coating was applied even though the coating barely affected the mesh size in SSM (Figure 3.3e and 3.3f). Given the poor water wetting properties on the pristine SSM (see Figure 3a and 3c), it is possible that some apertures of the pristine SSM were occupied by air, preventing water to permeate through during filtration. After the coating, these previously non-wetted regions became wetted by water, providing additional water channels to transport water, thus, increasing the water flux.

As mentioned earlier, low flux when separating emulsions has always been a challenge. Maximizing the flux while maintaining the transmembrane pressure below the breakthrough to ensure good selectivity is also important. To separate the oil stabilized by surfactants in OIW emulsions, it requires the membrane to have relatively small pore size, since the main mechanism of filtration is size exclusion which the membrane pores excludes all the oil drops that is larger than its diameter, while allows continuous water permeate through. Due to this reason, we chose to use the PC membrane as our testing substrate, since it has the smallest pores before and after coating. The emulsion we used is 1 vol% hexadecane in water stabilized by sodium dodecyl sulfate (SDS) and the separation setup is shown in Figure 3.7a (see detailed description in Experimental Section). As shown in Figure 3.7b and 3.7d, the feed contained both micron-sized and nanometer-sized oil droplets in the mixture, displaying a very strong light scattering effect (Figure 3.7b inset). After the feed is filtrated by the coated PC membrane, the filtrate is free of oil drops under optical microscopy (Figure 3.7c) and all micron-sized oil drops are excluded (Figure 3.7d). There is also no light scattering observed in the filtrate (Figure 3.7c inset), indicating great reduction of oil droplets in terms of both concentration and sizes.

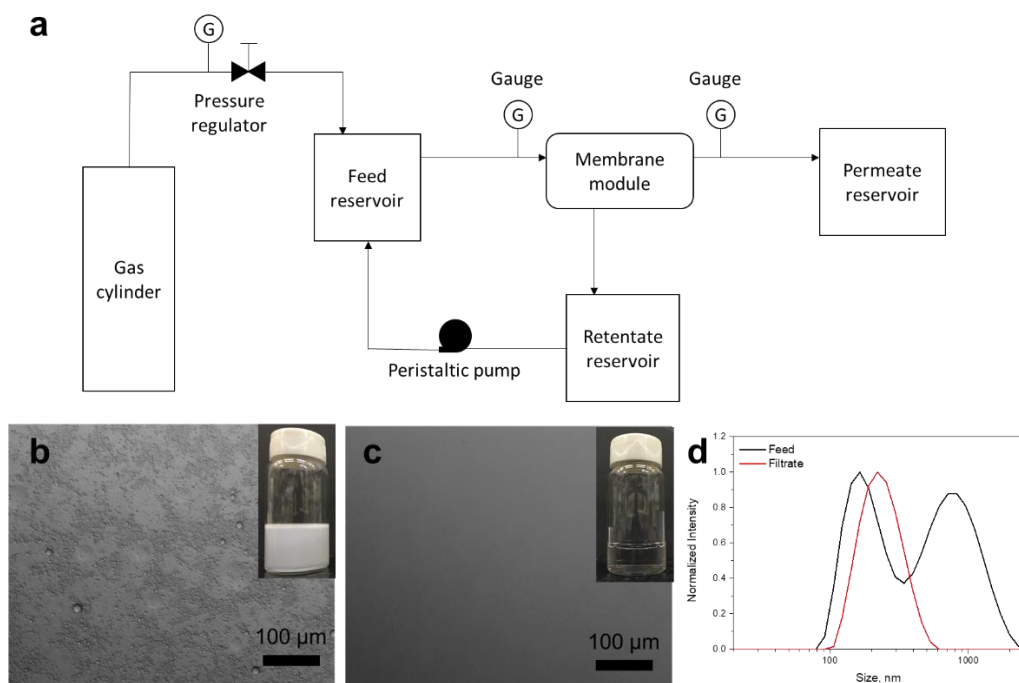


Figure 3. 7 (a) A flowchart of the pressure driven filtration for hexadecane-water emulsions using PAA-grafted nanochain coated PC membrane: (b) feed and (c) filtrate. (d) size distribution of the oil drop from DLS.

If the filtration is performed using pristine PC membrane at a very low pressure ($\ll 1$ psi), the oil rejection is quite high ($> 95\%$). As a result, the filtration flux is very low (Figure 3.8a). However, as the trans-membrane pressure is increased to 3.6 psi, the oil rejection drops dramatically to 60%. In comparison, the coated PC has the oil rejection above 97% at the low pressure. At the pressure of 3.6 psi, oil rejection remains above 90%. More importantly, the normalized flux is one order of magnitude higher than that of the pristine PC. Figure 3.8b and 3.8c confirms that there is still large amount of micron-sized oil drops observed under optical microscope and in the DLS scan after filtration using the pristine PC membrane, indicating both high concentration and large droplet size of the oil presented

in the filtrate. Therefore, the coated PC significantly outperform the pristine PC in pressurized oil/water emulsion separation.

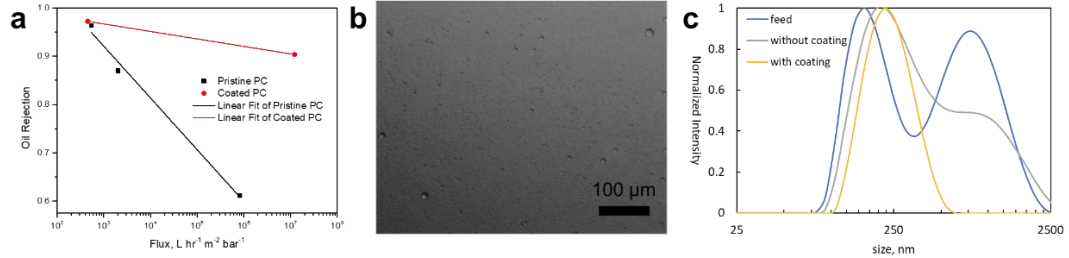


Figure 3. 8 (a) Relation of oil rejection and flux normalized by transmembrane pressure for emulsion separation using pristine and coated PC. (b) Optical microscope image of the filtrate from emulsion separation using PC membrane. (c) DLS result of the feed and the filtrate from emulsion separation using PC with and without the coating.

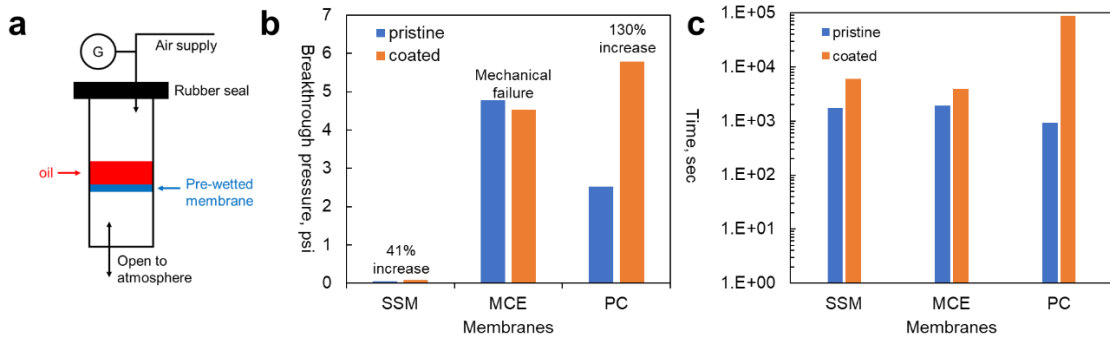


Figure 3. 9 (a) Schematic illustration of the setup used for measuring the breakthrough pressures for completely water pre-wetted membranes. (b) Measured breakthrough pressures for pristine and coated SSM, MCE, and PC. (c) The preservation time of the continuous water film on completely water pre-wetted membranes.

Besides the reduction of the pore size and improved surface wettability due to the coating, we speculate this also results an enhanced breakthrough pressure that ultimately leads to greatly improved separation efficiency in terms of both the oil rejection and normalized flux. To investigate this, we designed a setup (see Figure 3.8a) to measure breakthrough pressure (see details in Experimental Section). As shown in Figure 3.8b, both coated PC membrane and SSM have significantly increased breakthrough pressure by 130% and at least 41% (which is limited by the height of the tube), respectively. The absolute value for the SSM case is much lower than PC is because its pore size is much larger than PC. This also tells that the increased breakthrough pressure for SSM might be solely resulted from improved surface wettability. For PC membranes, a reduction of pore size might also play a role in increased breakthrough pressure. Due to the limitation of the setup, the MCE mechanically failed (membranes tear apart) without reaching the breakthrough pressure. Therefore, we expect with proper secondary mechanical supports, the pristine and coated PC might have breakthrough pressure much higher than its mechanical threshold. Finally, the level of water affinity can also be tested through how long the pre-wetted water film on membranes can be preserved before drying up. All coated membranes have improved their duration of preserving the continuous water layer, which is critical to keep membrane surface free of oil and lubricated to reduce hysteresis. This piece of information may also be useful for some time-sensitive scenarios in during separation operation such as emergency shutdown and scheduled cleaning.

3.4 Conclusion

In summary, we demonstrate the spray coating of PAA-grafted SiO₂ nanochains can also be applied onto different porous substrates and create robust superhydrophilic porous membranes. Furthermore, the resulting surface topology varies for substrates with different pore sizes. For coated membranes, they can be significantly better than pristine counterpart when dealing with oil/water free mixtures and emulsions, altering pore size and improving surface wettability. We also show that the trans-membrane pressure strongly affects the oil rejection and separation flux. It should be considered as a key parameter and not overlooked when testing oil/water separation. In addition, increased breakthrough pressure might play a major role of enhancing the oil/water filtration for our coated membrane system. While there are still rooms to improve the coated membrane such as mechanical durability and choice and types of support substrates, here, we demonstrate a simple yet versatile approach to improve existing membranes for oil/water filtration applications.

CHAPTER 4. Fabricating Janus Membranes via Immersion Precipitation of Polymers on Nanoparticle Packings

4.1 Introduction

In ancient Roman mythology, Janus is the name of god with two faces that see the future and the past.¹³⁵ In material sciences, Janus is used to describe materials that possess asymmetric properties, such as Janus particles.¹³⁶ Janus membranes that have opposite surface wettability on the two sides due to different chemical composition, surface structure, or the combination of the two.¹³⁷ Depending on specific applications and with proper designs, two opposite sides of Janus membranes can work cooperatively to facilitate or impede liquid transport through the membrane.¹³⁸ These properties that derive from the unique structure of Janus membranes make them useful in several applications such as water harvesting,¹³⁹ oil/water separation,¹⁴⁰ and wetting-controllable sensors¹⁴¹

One common approach to make Janus membranes is to sequentially fabricate each side of the membrane separately and then joining them. For examples, Janus membranes have been fabricated by sequentially depositing hydrophobic and hydrophilic nanotubes through filtration.¹⁴² Janus membranes can also be made by sequentially electrospinning hydrophilic poly(vinyl alcohol) and hydrophobic polyurethane fibers.¹⁴³ Another approach is to modify the surface wettability of one side of an existing membrane. Surface modification can be achieved through vacuum filtration of carbon nanotubes onto polypropylene substrates,¹⁴⁴ chemically grafting hydrophilic poly(N,N-dimethylaminoethyl methacrylate) onto cotton fabric,¹⁴⁰ or depositing inorganic materials

such as titanium oxide or zinc oxide on hydrophobic membranes.^{145,146} Despite these advances, there are several challenges associated with the fabrication of Janus membranes; for example, selective modification of one side of the membrane can be difficult due to the permeation of the surface modifying agent through the membrane to the other side.¹³⁷ Also large-scale production of Janus membranes remain a challenge.

A phase separation-based method, which is a common approach to produce porous polymer membranes, has also been used for fabricating Janus membranes. In this method, a porous membrane is made by casting a film of a homogenous polymer solution onto a substrate and inducing phase separation by exposing the solution film to a non-solvent (typically water) for the polymer. Janus structures can be formed by inducing migration or phase separation of a component on one side of the membrane. For example, Janus membranes have been formed by triggering phase separation via solvent evaporation which in turn induced migration of hydrophilic PEG-diamines to one side and hydrophobic alkane-diamine blends to the opposite side of the membrane.¹⁴⁷ Hydrophilic nanoparticles and hydrophobic polymer can also be a good combination as the casting blend for making Janus membranes. However, it is hard to make well suspended blends with the hydrophobic polymer solution and high loading of silica nanoparticles. The increase of viscosity might also make it more difficult to process. A fabrication approach that can avoid these limitations would be worthwhile to pursue. Moreover, as described in prior chapters, fabrication of a highly porous layer made of stringy nanoparticle or nanochains on one side of the membrane could lead to Janus membranes with excellent anti-fouling properties that could be used in oil-water separations.¹⁴⁸

In this work, we explore the possibility of making Janus membranes by pre-depositing nanoparticle (NPs) onto a solid surface and inducing phase separation of polymer by immersion precipitation on top of the pre-deposited nanoparticle layer. By inducing delamination of the composite bilayer structure, we hypothesize that it will be possible to produce Janus membranes with one side fully covered with NPs and a pure polymer phase on the other side. We successfully fabricate a free standing Janus membrane using silica nanoparticles (SiO_2 NPs) and polyvinylidene fluoride (PVDF). The SiO_2 NP side of the membrane becomes more hydrophilic. In water, the SiO_2 NPs side of the membrane is underwater superoleophobicity. The change of the final membrane morphology is also investigated through changing the blade casting speed, the casting method, and the particle shape of the pre-deposit NP packings. Even though the method still requires more work to optimize the fabrication and solving some issues such as incomplete transferring of NPs in some conditions and formation of cracks. This new approach allows loading a large quantity of NPs on one side and avoid their migration to the other side during the membrane formation, enabling scalable manufacturing of Janus membranes.

4.2 Experimental Section

Materials. Polyvinylidene fluoride (PVDF, average Mw ~534,000), n-hexadecane (ReagentPlus, 99%), oil red-O (red dye), poly(acrylic acid) (PAA, average Mv ~450000), and dimethylformamide (DMF, anhydrous, 99.8%), were purchased from Sigma-Aldrich and used as received. Silica nanoparticles (SiO_2 NPs) solutions ORGANOSILICASOL™

IPA-ST-UP, IPA-ST-ZL) were purchased from Nissan Chemical America Corporation and used as received. Ethanol 200 proof (100%), 2-Propanol (IPA, Certified ACS), and 1,2-dichloroethane (DCE, $\geq 99\%$) were purchased from Fisher Scientific and used as received.

Preparation of solutions and substrates. The PAA aqueous solution (5 wt%) was prepared by mixing PAA and DI water in a glass vial through magnetic stirring for 2 hours. Purchased SiO₂ NPs solutions (in IPA) were diluted to 15 wt% and sonicated for 15 min in sonication bath before using. The PVDF solution (10 wt%) was prepared by mixing PVDF and DMF through magnetic stirring in a glass vial overnight. The casting substrates were glass slides and cleaned by rubbing with acetone followed by oxygen plasma treatment (Harrick PDC-001, high RF level) for 1 min.

Preparation of Janus membranes. There are 4 major steps to fabricate the membrane as shown in Figure 4.1. First the PAA solution was coated onto the glass slide using a flow coater (THORLABS, NRT100) with the casting speed of 20 mm/s, the blade angle of 30° and gap space of 400 μm between the blade and the substrate. After flow coated PAA was dried in air, the second step was to coat SiO₂ NPs solutions on top of the PAA layer using the same flow coating procedure with the same the speed, blade angle, and the gap space. After the coated NPs layer was also dried in air, the PVDF solution was manually casted using a doctor blade (200- μm gap space between the blade and the substrate) on top of the NP layer. As the final step, the PVDF casted substrate was immediately immersed into the DI water bath to induce phase inversion. After 2 hours, the membrane was collected.

Characterization. Water contact angles were obtained by dropping 4- μ L DI water onto the membrane in air and the static contact angle was measured based on the sessile drop method using a goniometer (Attention, Biolin Scientific). The underwater oil contact angle was obtained by dropping 4- μ L dichloroethane (DCE, $\gamma = 33.3 \text{ mN m}^{-1}$) onto the membrane which was placed in a cubic glass container filled with DI water using the same goniometer. Morphologies of the membranes were characterized by scanning electron microscopy (SEM) using the JEOL 7500F HRSEM at an acceleration voltage of 5 kV and emission current of 20 μ A.

4.3 Results and Discussion

The fabrication procedure of the Janus membrane consists of 4 steps (Figure 4.1): first three steps involve formation of a PAA-NPs-PVDF multilayer onto a substrate and one final step to immerse the substrate in water to induce phase inversion to form the membrane. The purpose of the PAA bottom layer is to serve as a sacrificial layer to induce delamination of the membrane upon formation. Because PAA is soluble in water, it helps the detachment of the final membrane. It also helps to transfer more NPs onto the final membrane by separating the substrate and the NP layer. The sequential deposition of the NP layer and the PVDF layer is to form the hydrophilic and hydrophobic side of the membrane. Immersion precipitation to make the final PVDF is porous.

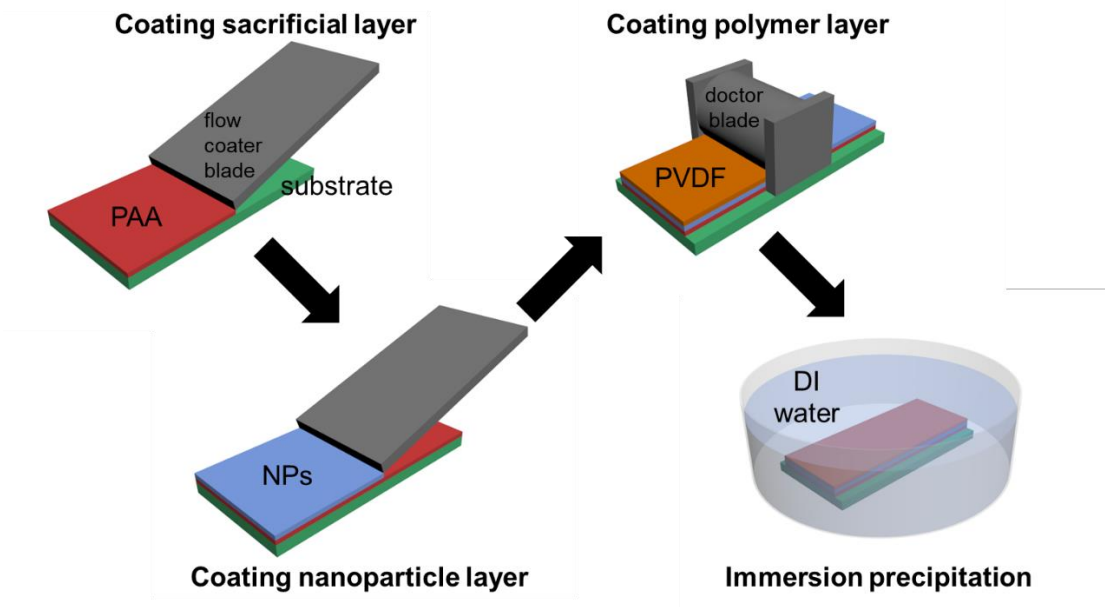


Figure 4. 1 Schematic of each steps to fabricate the membrane.

The SEM images from Figure 4.2a to 4.2d illustrate the morphology of the Janus membrane made using the steps in Figure 4.1. The Janus membrane formed is a free-standing membrane with two distinctive layers successfully attached together. In Figure 4.2a, the layer on top is the SiO₂ NPs layer with the thickness of 10 μm and the bottom is the PVDF with the thickness of 25 μm. The PVDF layer have two main characteristics: smaller cellular pore networks (diameter of 1 to 2 μm) with some larger micro-voids (diameter of 10 to 20 μm) embedded. Figure 4.2b shows a closer look at the interface of the two layers and the nanoparticles are very closely packed together. However, it is unclear to determine if there are any polymers that are infiltrated into the interspacing between particles due to limited resolution. Nevertheless, the NP layer is still porous and has pores with diameter about 14 nm according to the SEM image in Figure 4.2c. On the other side show in Figure

4.2d, it is the PVDF side. It has larger pores with wider range of diameters from 50 to 500 nm.

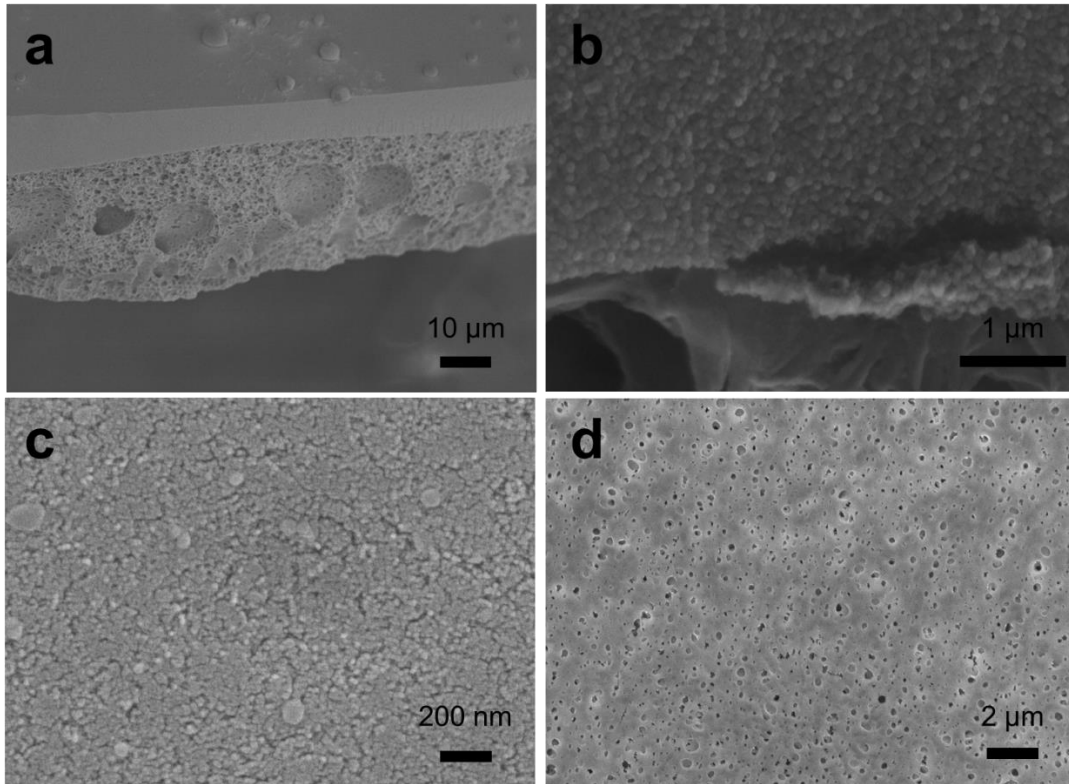


Figure 4. 2 (a) Cross-sectional SEM image of the Janus membrane. (b) Zoomed-in image of the membrane area at the NP-PVDF interface. (c, d) Top-view SEM image of the Janus membrane surface on the side with (c) SiO₂ NPs and the side with (d) PVDF, respectively.

Water contact angles in air and dichloroethane contact angles under water are measured on both side of the membrane to show the membrane is Janus. According to Figure 4.3a, The NP side and the PVDF side of the membrane has a water contact angle of 16.9° and 79.7°, respectively, showing the NP side is much more hydrophilic than the PVDF side. It is consistent with what we observed in the Figure 4.2c showing the hydrophilic SiO₂ NPs are

fully exposed on one side of the membrane. The NP side of the membrane also has a contact angle of dichloroethane of 158° under water. It is much larger than the PVDF side of 22.5° , showing the NP side has even larger contrast in underwater oleophobicity than the hydrophilicity comparing with the PVDF side. The top 3 images in Figure 4.3b show when a dichloroethane droplet is compressed onto the NP side of the membrane, the droplet does not adhere onto the surface. On the contrary, when the dichloroethane droplet touches the PVDF side of the membrane, it spreads onto the membrane like the bottom 3 images in Figure 3b. Figure 4.3c gives a more visual demonstration. Drops of dichloroethane dyed by oil red are dispensed onto the NP side of the membrane and it remains spherical and rolls to the edge of the membrane. When the dichloroethane drop contacts the PVDF side, it wets the membrane and spreads. Figure 4.3d shows the Janus membrane is water-permeable under gravity from the direction of the NP side to the PVDF side. Also using the same direction loadout, it separates the free mixture of DI water and hexadecane (dyed in oil red), allowing water to go through but not the oil.

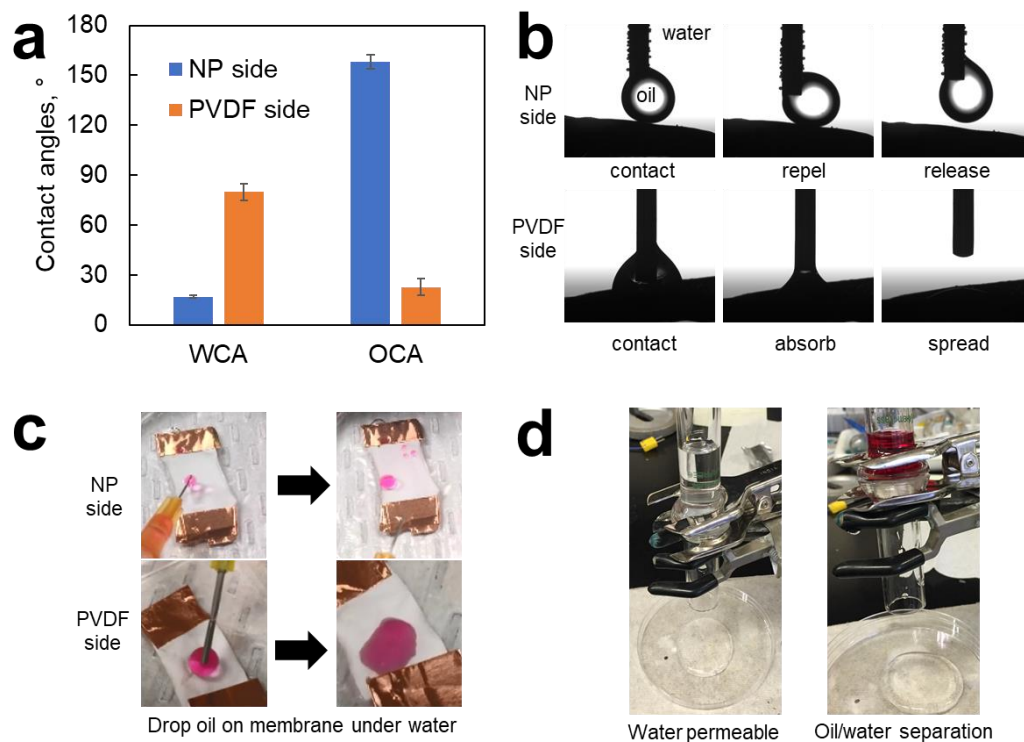


Figure 4. 3 (a) Contact angles of water (WCA) in air and dichloroethane (OCA) under water on nanoparticle (NP) side of the membrane and PVDF side of the membrane. (b) Goniometer captured images of a pendent drop of dichloroethane in water contacting the NP side (top) and PVDF side (bottom) of the membrane. (c) Visual images of dispensing drops of dichloroethane dyed by oil red under water onto the NP side (top) and the PVDF side (bottom) of the membrane. (d) Visual image captures of the Janus membrane (left) during filtrating the DI water and (right) at the end of filtrating the hexadecane/water free mixture.

As the Janus property is demonstrated, next we adjusted some parameters in our fabrication procedure to further investigate and to have better understanding how these parameter affects the final morphology of the Janus membrane. We first look at the thickness of the

NP layer as the thickness (or the mass per unit area) of the hydrophilic layer is one of the key parameters affecting surface wettability of the Janus membrane.¹⁴⁴ To control this in our procedure is to control the blade casting speed of the NP solution during the flow coating, since the blade speed is the one of the major factors that determines the final thickness of the deposited layer in flow coating.¹⁴⁹ Figure 4.4a shows that as we increase the blade speed of the flow coating, the thickness of the nanoparticle layer deposited on the sacrificial layer increases. This positive correlation is consistent with the flow coating in Landau-Levich regime in literature since our blade speeds are much higher than 100 $\mu\text{m/s}$.¹⁵⁰ We switched to using NPs with larger size (average diameter of 114 nm instead of 25 nm) to visualize NPs and their interspacing. From Figure 4.4b and 4.4c, we can see that at relatively low blade speed of 0.5 mm/s and 1 mm/s, the thickness of the NP layer is about 576 nm and 712nm, respectively. In these two cases, the PAA sacrificial layer infiltrates through the NP packing and fills the interparticle spacing. This might be caused by unintentionally solvent annealing of the PAA film using the IPA from the NP solution during the flow coating. At higher blade speed of 5 mm/s, 10 mm/s, and 20 mm/s, the thickness of the NP layer is about 1760 nm, 1929 nm, and 2694 nm, respectively. There is PAA presented in the interparticle spacing in the lower part of the NP packing but the top part is free of PAA as show in Figure 4.4d, 4.4e, and 4.4f.

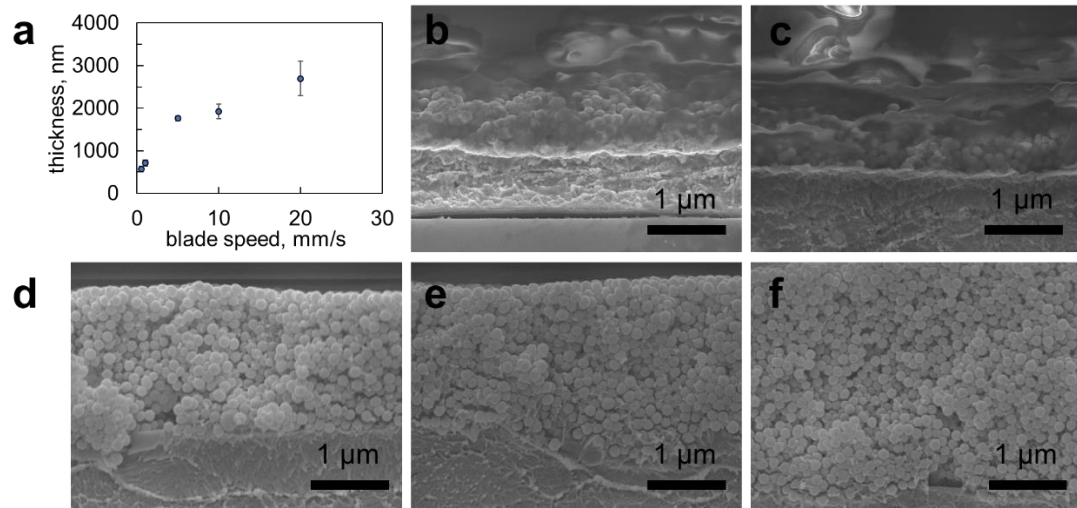


Figure 4. 4 (a) The correlation between the thickness of the NP layer on top of the sacrificial layer after the flow coating versus the blade casting speed during the flow coating. (b-f) Cross-sectional SEM images of the NP layer deposited on the sacrificial layer using flow coating with blade speed of (b) 0.5 mm/s, (c) 1 mm/s, (d) 5 mm/s, (e) 10 mm/s, and (f) 20 mm/s, respectively.

Figure 4.5 summarizes the surface morphology difference of membranes fabricated using different blade speeds during the flow coating. When the blade casting speed is 5 mm/s or lower, the resulted membrane surface rarely catching any NPs on the final membrane surface and only a few are observed (Figure 4.5a and 4.5d). When the blade speed is 10 mm/s, the resulted membrane surface consists a mixture of PVDF and NP regions with about 1:1 ration on the surface as shown in Figure 4.5b and 4.5c. When the blade speed is 20mm/s, the fabricated membrane surface has fully covered NP layer (Figure 4.5c and 4.5f). Since higher blade speed results thicker NP layer after the flow coating, we think there is a critical NP layer thickness need to be reached to allow a fully cover of NPs onto

the final phase inverted membrane. In this case, the thickness is about $2.7\ \mu\text{m}$ to ensure a fully NP covered membrane. We speculate below this thickness, the structural integrity of the deposited NP layer might be affected during the PAA dissolving in the final immersion precipitation step, resulting an incomplete transfer of the NP layer onto the final membrane showed in Figure 4.5a and 4.5b.

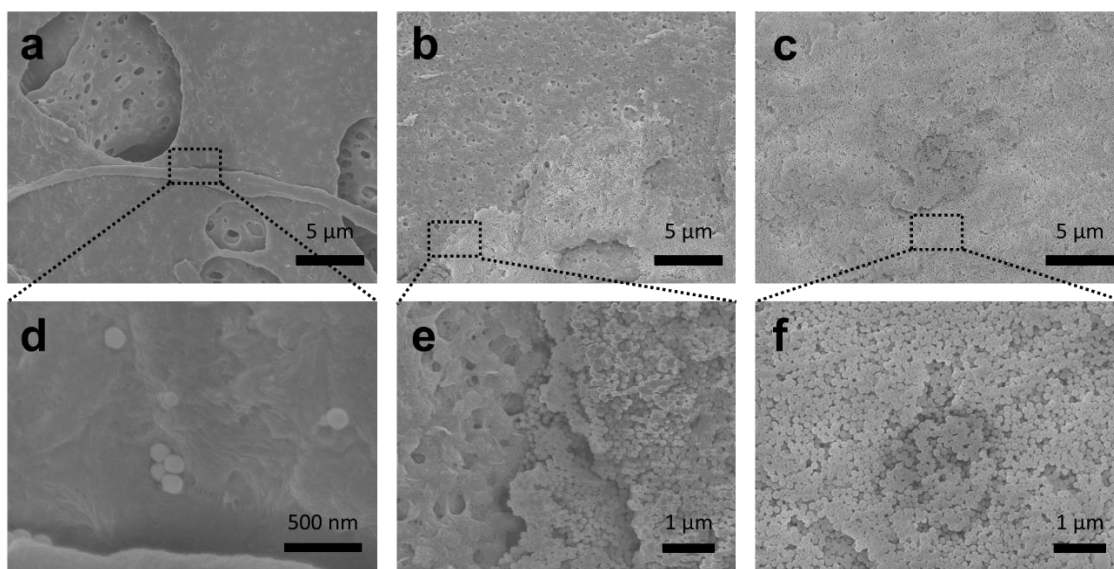


Figure 4. 5 (a, b, c) Top-view and (d, e, f) zoomed-in SEM images of the NP side of the final Janus membrane with blade speed of (a, d) 5 mm/s, (b, e) 10mm/s, and (c, f) 20 mm/s during the flow coating step of the fabrication procedure, respectively.

To see if other NP deposition method can also be incorporated into this fabrication procedure, the flow coating is replaced with spray coating of NPs in the second steps (Figure 4.6a). We keep out sprayed thickness to be about $2.5\ \mu\text{m}$ on the initial substrate based on the relation we reported reviously.³² As we can see in the cross-sectional SEM image in Figure 4.6b and 4.6c, the NP is fully covered and attached to the final membrane

with thickness about 1.1 μm . Comparing it with the NP side of the membrane formed using flow coating, the membrane surface from using spray the coated NP layer is more distorted and less smooth. This might be an indicator of the presence of infiltrated PVDF into the nanoparticle packing. The PVDF is easier to infiltrate to the NP packing from since the spray coated NPs are packed more loosely and offers less resistance for the PVDF (Figure 4.6c and 4.6d). If we take closer look at the NP side surface of the membrane in Figure 4.6d, we can observe some PVDF bridging between NPs. We believe this PVDF bridging attaches the NP layer firmly to the PVDF layer, and the rest of the NP packing might be lost during immersion precipitation bath due to loose packing, resulting the thinner final NP thickness in the membrane (1.1 μm instead of 2.5 μm). However, the overall mechanical integrity of the remaining NP layer might be greatly enhanced.

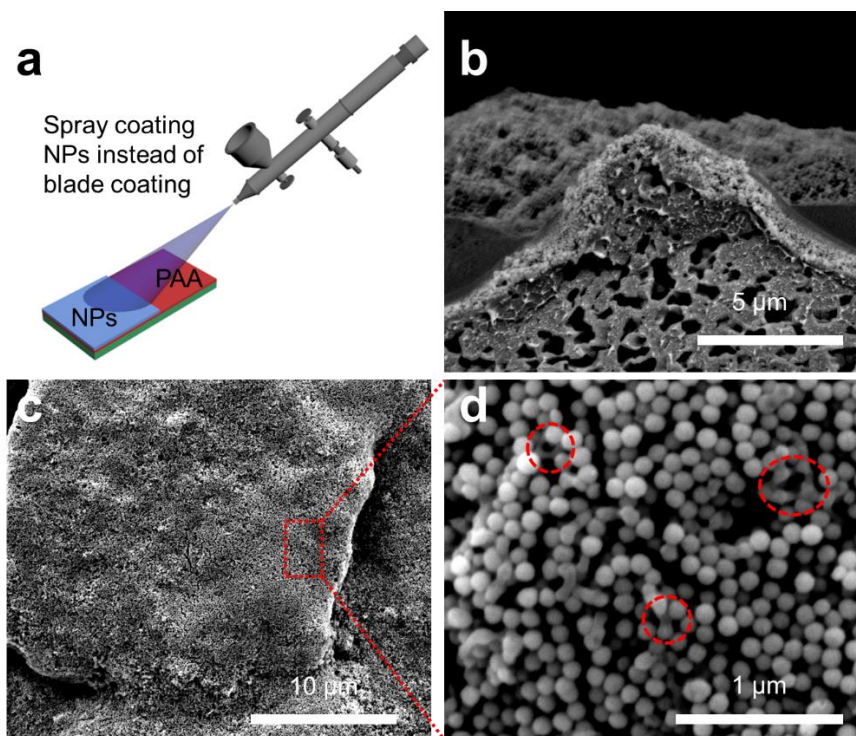


Figure 4. 6 (a) Schematic illustration of the spray coating step for the NP layer replacing the second step, flow coating NPs, of the fabrication procedure in Figure 4.1. (b) Cross-sectional and (c, d) top-view SEM images of the final Janus membrane when the NP layer is spray coated instead of flow coated during the second step of the fabrication. Note: red circles in dashed line indicates the PVDF bridging between NPs.

According to our previous study, spraying chain-linked NPs instead of spherical NPs gives NP packings with higher porosity. This further increase of porosity might facilitate the infiltration of PVDF further into the packing during the immersion precipitation. To test this idea, we switched the NPs from spherical to chain-like shaped illustrated in Figure 4.7a. The chain-linked NP is prepared following the protocol in our previous study.³² The membrane surface has three different types of surface morphologies (Figure 4.7b). The first type is the NP layer but covered with a thin layer of PVDF (Figure 4.7c and Figure 4.7d).

The beneath NP layer has thickness about 2.6 μm and the thin layer of PVDF on top is about 100 nm thick. We believe this is caused by the overly infiltrated PVDF. Within the PVDF covered region, there are some areas that have the chain-like NP layer fully exposed (Figure 4.7e), which is the second type of the surface morphology. The third type of the morphology is the fully porous PVDF region in Figure 4.7f. This is similar to what we observed in Figure 4.5e of the possibly due to the insufficient thickness of the NP layer. Therefore, we believe that if the NP packing is more loosely packed and have larger interparticle spacing, the critical thickness of the deposited NP layer should also be higher to ensure a fully NP covered morphology in the final membrane.

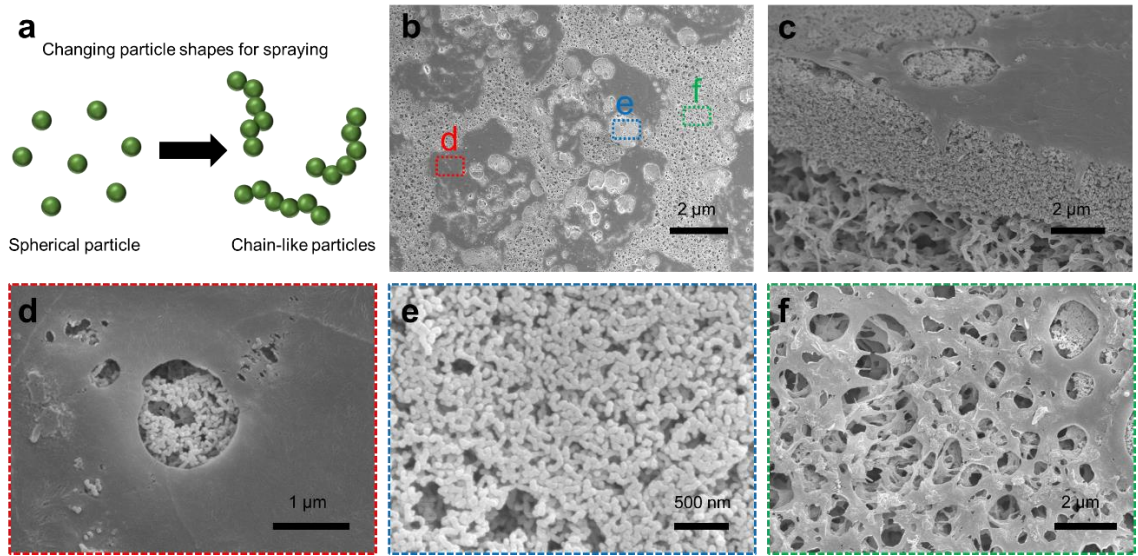


Figure 4. 7 (a) Schematic illustration of the particle shape changes from spherical NPs to chain-like shaped NPs. (b) Top-view and (c) cross-sectional SEM images of the NP side of the final Janus membrane when the spray coated NP is chain-like shaped instead of spherical during the NP coating step of the fabrication. (d, e, f) Zoomed-in SEM images of

three distinctive regions of the membrane surface showed in Figure 4.7b. Note: the red, blue, green colored letters and markers in (b) corresponds (d), (e), and (f), respectively.

Finally, we will discuss some observations that brings problems that needs more investigations to understand. Figure 4.8a shows if the concentration of the NP solution drops to 10 wt% from 15 wt% used in flow coating, the transfer of NP layer can be incomplete. The resulting membrane surface (Figure 4.8b) is very similar to the membrane surface formed without NP packing (Figure 4.8c). The membrane affected by the incomplete transferring of the NP layer has slightly rougher surface with larger pores ranging from 0.4 to 3.6 μm (Figure 4.8b), while the membrane from no NP layer at all has smoother surface with smaller pores ranging from 0.4 to 1.7 μm (Figure 4.8c). In addition, there are cracks observed in the NP layer of the final membrane (Figure 4.8d). Between these cracks, there is infiltrated PVDF presented (Figure 4.8e and Figure 4.8f). These cracks might be the original cracks formed after the flow coating or later formed and propagated from the infiltration of PVDF during the immersion precipitation step. Being able to reduce the number of cracks or producing a crack free NP layer during the flow coating might improve the hydrophilicity of the surface further. However, it is possible that the infiltrated PVDF in the crack enhances helps attaching the NP layer more firmly to the PVDF layer, which might be beneficial to the overall mechanical durability of the membrane.

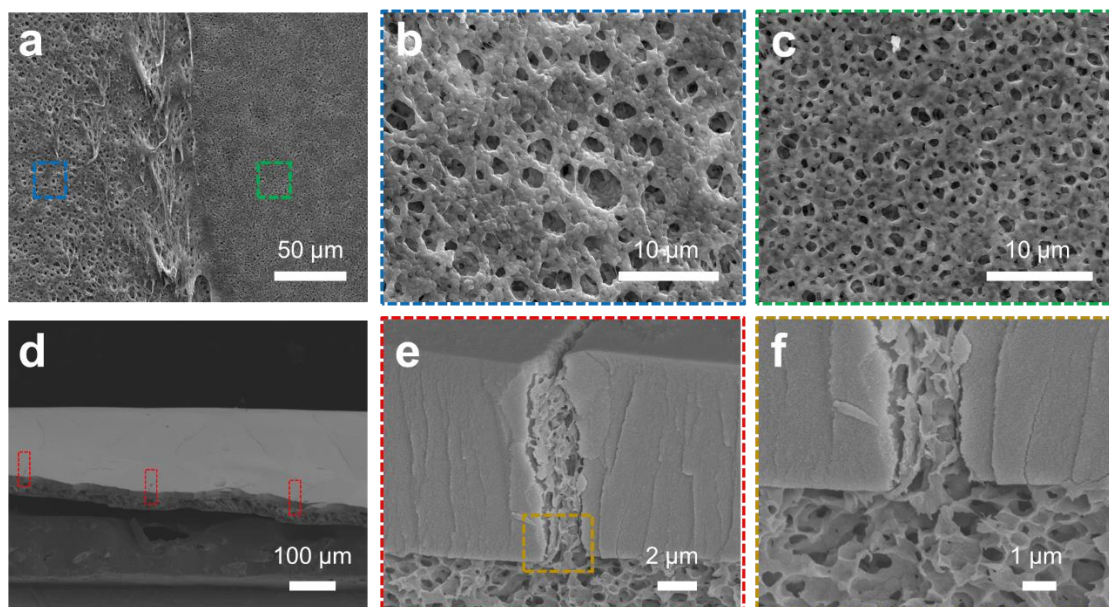


Figure 4. 8 (a) Top-view SEM image of the PVDF membrane surface at an interface with the left-hand side of the membrane in the image formed using the procedure in Figure 4.2 with 10 wt% of NP solution during the flow coating, and the right-hand side of the membrane in the image formed without any NP solution coating in the fabrication procedure. (b) Zoomed-in SEM image of the left-hand side of the membrane in Figure 4.8a. (c) Zoomed-in SEM image of the right-hand side of the membrane in Figure 4.8a. (d) Cross-sectional SEM image of the Janus membrane with visual cracks on the NP layer and (e, f) their zoomed-in SEM images.

4.4 Conclusion

In summary, by utilizing the flow coating to fast deposit SiO₂ NP packing and immersion precipitation to form porous PVDF, we successfully fabricated a Janus membrane. The hydrophilicity and underwater oleophobicity contrast between two sides is achieved. The

membrane is also water permeable and has potential to be further developed for applications. We also manage to the thickness and the porosity of the deposited NP packing before applying PVDF affects the final membrane morphology on the NP side, which might lead to incomplete transfer of NP packing, formation of mixture regions, or a fully NP covered surfaces. We also observed there is PVDF bridging presented between particles when the NPs packed more loosely and PVDF tends to infiltrate into cracks. We think this might improve the mechanical durability of the NP layer in the Janus membrane, but more work is needed in the future to further investigate the mechanical enhancement and cracks.

Chapter 5. Conclusion and Outlook

5.1 Conclusion

In *chapter 1*, the fundamental of the controlling surface wettability through tuning the surface chemistry and manipulation of surface structures are introduced. In addition, superhydrophilic/underwater superoleophobic surfaces are further discussed focusing on different fabrication methods and its application potentials on improving oil/water separation membranes.

Chapter 2 demonstrates a simple yet versatile approach to create an ultrastable superhydrophilic coatings with excellent anti-oil fouling property via a scalable manufacturing scalable method. The coating is made by spray coating PAA-grafted SiO₂ nanochains onto solid surface substrates. The coating is superhydrophilic/underwater superoleophobic. It is very robust that even the coating is purposely fouled by oil, oil can be readily and completely expelled and lifted-off from the coating within 10 s when placed under water. Comparisons with other hydrophilic and superhydrophilic surfaces are made to show both the unique structure of spray-assembled nanochains and the hygroscopic nature of PAA are essential to enable ultrastable anti-oil fouling. In addition, we show our coating retains underwater superoleophobicity even after being subjected to shearing under water for more than 168 hours.

Chapter 3 shows the application potential of the newly developed superhydrophilic PAA-grafted SiO₂ nanochain coating described in the previous chapter by testing the coating deposited on commercially available porous membranes instead of smooth solid substrates.

The coatings are applied onto three types of membranes (PC, MCE, and SSM) with different morphologies and pore sizes are tested as substrates, and different surface morphologies are also obtained after the coating. Comparing with pristine membranes, all coated membranes demonstrate improved hydrophilicity and underwater oleophobicity by showing reduced water contact angles in air, increased oil contact angles under water, and reduced oil adhesion. Drastic enhancements in oil/water filtration after the coating are observed for SSM dealing with free mixtures and PC for emulsions, due to the significantly increased breakthrough pressure after the coating.

Chapter 4 describes a new procedure to fabricate Janus membranes for the purpose of developing a simple but effective fabrication approach that possess advantages over current fabrication alternatives. The new approach combines the immersion precipitation of hydrophobic PVDF on pre-deposited hydrophilic silica nanoparticles, forming a freestanding porous Janus membrane with a distinctive hydrophilic layer and hydrophobic layer on each side of the membrane attached together. Both layers are porous with asymmetric porous morphologies. Contact angles of each side of the membrane display large wettability contrast with over 60° in hydrophilicity and over 130° in underwater oleophobicity. The final morphology of the membrane is largely affected by the pre-deposited nanoparticle films when caused by changing deposition methods and parameters, particle size, or particle shapes. When the film is below a critical thickness which might vary depending on particle size and shape, the final membrane might not have the hydrophilic layer. When the interspacing of the pre-deposited nanoparticle packing is too large or there are cracks appeared in the packing, the PVDF might also appear in the

nanoparticle layer. There are still lots of work are needed in the future to fully explore and optimize this new approach to make it more robust to fabricate Janus membranes.

5.2 Outlook for Future Research

5.2.1 SiO₂ nanochain coatings grafted with other polyelectrolytes

The coating with excellent anti-fouling property demonstrated in *Chapter 2* are made from poly(acrylic acid)-grafted SiO₂ nanochains. The grafting of poly(acrylic acid) is necessary to ensure fast and complete lifting of oil trapped inside the coating by immersing into water. This coating system can be further expanded by switching attached poly(acrylic acid) with other types of polyelectrolytes with different charges, molecular weight, and grafting density to further investigate their effects on the oil-lifting behavior on the nanochain coating and better understand the mechanism. In the study, different types of oil are tested, and their surface tensions are considered as one of major factors for the wetting behavior. Wider range of oils with different viscosity, density, and polarity can also be tested along with different grafted polyelectrolytes to explore the oil-lifting effect more systematically.

5.2.2 Effectiveness of the coating in harsh environments

The coating in *Chapter 2* and *Chapter 3* is nanoparticle-based with nano-scale surface textures. We are able to show it is effective and long-lasting in neutral aqueous environment under shearing. In actual application environment, the coating might encounter harsh environment such as high salt concentration, suspended solids, acidic or

basic environment. The harsh environment might chemically or physically affect the composition or structural integrity of the coating, resulting a change in the wettability. Being able to improve the coating and show that it can survive the harsh environment will surely make it more competitive and suitable for broader range of applications.

5.2.3 Optimizing the tunability of the Janus membrane

The fabrication procedure described in *Chapter 4* can be utilized to make Janus membranes using the right combination of hydrophilic nanoparticles and hydrophobic polymers. Underwater oleophilicity and underwater superoleophobicity can be achieved using this approach. Attempts to gradually reduce the thickness of hydrophilic nanoparticle layer of the Janus membrane are made by reducing the particle concentration or blade speed during particle deposition to tune the wettability of the membrane to somewhere between underwater oleophilic and superoleophobic. However, it only results a lost or incomplete transfer of nanoparticle layer in the final membrane. Being able to tune the wettability of the Janus membrane further through controlling the NP layer thickness via the current method allows the membrane to deal with separating oil/water emulsion more effectively through demulsification and it is worthy to pursuit further.¹⁴⁴

BIBLIOGRAPHY

- (1) Bonn, D.; Eggers, J.; Indekeu, J.; Meunier, J.; Rolley, E. Wetting and Spreading. *Rev. Mod. Phys.* **2009**, *81* (2), 739–805. <https://doi.org/10.1103/RevModPhys.81.739>.
- (2) Bertrand, E.; Bonn, D.; Broseta, D.; Dobbs, H.; Indekeu, J. O.; Meunier, J.; Ragil, K.; Shahidzadeh, N. Wetting of Alkanes on Water. *Journal of Petroleum Science and Engineering* **2002**, *33* (1), 217–222. [https://doi.org/10.1016/S0920-4105\(01\)00191-7](https://doi.org/10.1016/S0920-4105(01)00191-7).
- (3) de Gennes, P. G. Wetting: Statics and Dynamics. *Rev. Mod. Phys.* **1985**, *57* (3), 827–863. <https://doi.org/10.1103/RevModPhys.57.827>.
- (4) Young, T. III. An Essay on the Cohesion of Fluids. *Philosophical Transactions of the Royal Society of London* **1805**, *95*, 65–87. <https://doi.org/10.1098/rstl.1805.0005>.
- (5) Berg, J. *An Introduction to Interfaces & Colloids The Bridge to Nanoscience*; World Scientific Publishing Co. Pte. Ltd., 2010.
- (6) Wenzel, R. N. RESISTANCE OF SOLID SURFACES TO WETTING BY WATER. *Ind. Eng. Chem.* **1936**, *28* (8), 988–994. <https://doi.org/10.1021/ie50320a024>.
- (7) Cassie, A. B. D.; Baxter, S. Wettability of Porous Surfaces. *Trans. Faraday Soc.* **1944**, *40* (0), 546–551. <https://doi.org/10.1039/TF94444000546>.
- (8) Eral, H. B.; 't Mannetje, D. J. C. M.; Oh, J. M. Contact Angle Hysteresis: A Review of Fundamentals and Applications. *Colloid Polym Sci* **2013**, *291* (2), 247–260. <https://doi.org/10.1007/s00396-012-2796-6>.
- (9) Drelich, J.; Chibowski, E. Superhydrophilic and Superwetting Surfaces: Definition and Mechanisms of Control. *Langmuir* **2010**, *26* (24), 18621–18623. <https://doi.org/10.1021/la1039893>.
- (10) Ahmad, D.; Boogaert, I. van den; Miller, J.; Presswell, R.; Jouhara, H. Hydrophilic and Hydrophobic Materials and Their Applications. *Energy Sources, Part A: Recovery, Utilization, and Environmental Effects* **2018**, *40* (22), 2686–2725. <https://doi.org/10.1080/15567036.2018.1511642>.
- (11) Feng, X. J.; Jiang, L. Design and Creation of Superwetting/Antiwetting Surfaces. *Advanced Materials* **2006**, *18* (23), 3063–3078. <https://doi.org/10.1002/adma.200501961>.
- (12) Asmatulu, R. Highly Hydrophilic Electrospun Polyacrylonitrile/Polyvinylpyrrolidone Nanofibers Incorporated with Gentamicin as Filter Medium

- for Dam Water and Wastewater Treatment. *J. Memb. Separ. Tech.* **2016**, *5* (2), 38–56. <https://doi.org/10.6000/1929-6037.2016.05.02.1>.
- (13) Quéré, D. Non-Sticking Drops. *Rep. Prog. Phys.* **2005**, *68* (11), 2495–2532. <https://doi.org/10.1088/0034-4885/68/11/R01>.
- (14) Smith, T. The Hydrophilic Nature of a Clean Gold Surface. *Journal of Colloid and Interface Science* **1980**, *75* (1), 51–55. [https://doi.org/10.1016/0021-9797\(80\)90348-3](https://doi.org/10.1016/0021-9797(80)90348-3).
- (15) Gentleman, M. M.; Ruud, J. A. Role of Hydroxyls in Oxide Wettability. *Langmuir* **2010**, *26* (3), 1408–1411. <https://doi.org/10.1021/la903029c>.
- (16) Harju, M.; Levänen, E.; Mäntylä, T. Wetting Behaviour of Plasma Sprayed Oxide Coatings. *Applied Surface Science* **2006**, *252* (24), 8514–8520. <https://doi.org/10.1016/j.apsusc.2005.11.065>.
- (17) Drelich, J.; Chibowski, E.; Meng, D. D.; Terpilowski, K. Hydrophilic and Superhydrophilic Surfaces and Materials. *Soft Matter* **2011**, *7* (21), 9804–9828. <https://doi.org/10.1039/C1SM05849E>.
- (18) Yeh, K.-Y.; Chen, L.-J.; Chang, J.-Y. Contact Angle Hysteresis on Regular Pillar-like Hydrophobic Surfaces. *Langmuir* **2008**, *24* (1), 245–251. <https://doi.org/10.1021/la7020337>.
- (19) Solomon, B. R.; Hyder, M. N.; Varanasi, K. K. Separating Oil-Water Nanoemulsions Using Flux-Enhanced Hierarchical Membranes. *Scientific Reports* **2014**, *4*, 5504. <https://doi.org/10.1038/srep05504>.
- (20) Onda, T.; Shibuichi, S.; Satoh, N.; Tsujii, K. Super-Water-Repellent Fractal Surfaces. *Langmuir* **1996**, *12* (9), 2125–2127. <https://doi.org/10.1021/la950418o>.
- (21) Shibuichi, S.; Onda, T.; Satoh, N.; Tsujii, K. Super Water-Repellent Surfaces Resulting from Fractal Structure. *J. Phys. Chem.* **1996**, *100* (50), 19512–19517. <https://doi.org/10.1021/jp9616728>.
- (22) Liu, M.; Wang, S.; Wei, Z.; Song, Y.; Jiang, L. Bioinspired Design of a Superoleophobic and Low Adhesive Water/Solid Interface. *Advanced Materials* **2009**, *21* (6), 665–669. <https://doi.org/10.1002/adma.200801782>.
- (23) Wu, D.; Wu, S.; Chen, Q.-D.; Zhao, S.; Zhang, H.; Jiao, J.; A. Piersol, J.; Wang, J.-N.; Sun, H.-B.; Jiang, L. Facile Creation of Hierarchical PDMS Microstructures with Extreme Underwater Superoleophobicity for Anti-Oil Application in Microfluidic Channels. *Lab on a Chip* **2011**, *11* (22), 3873–3879. <https://doi.org/10.1039/C1LC20226J>.
- (24) Yong, J.; Chen, F.; Yang, Q.; Zhang, D.; Farooq, U.; Du, G.; Hou, X. Bioinspired Underwater Superoleophobic Surface with Ultralow Oil-Adhesion Achieved by

- Femtosecond Laser Microfabrication. *Journal of Materials Chemistry A* **2014**, *2* (23), 8790–8795. <https://doi.org/10.1039/C4TA01277A>.
- (25) Zhang, F.; Zhang, W. B.; Shi, Z.; Wang, D.; Jin, J.; Jiang, L. Nanowire-Haired Inorganic Membranes with Superhydrophilicity and Underwater Ultralow Adhesive Superoleophobicity for High-Efficiency Oil/Water Separation. *Advanced Materials* **2013**, *25* (30), 4192–4198. <https://doi.org/10.1002/adma.201301480>.
- (26) Gao, X.; Xu, L.-P.; Xue, Z.; Feng, L.; Peng, J.; Wen, Y.; Wang, S.; Zhang, X. Dual-Scaled Porous Nitrocellulose Membranes with Underwater Superoleophobicity for Highly Efficient Oil/Water Separation. *Advanced Materials* **2014**, *26* (11), 1771–1775. <https://doi.org/10.1002/adma.201304487>.
- (27) Yong, J.; Chen, F.; Yang, Q.; Du, G.; Shan, C.; Bian, H.; Farooq, U.; Hou, X. Bioinspired Transparent Underwater Superoleophobic and Anti-Oil Surfaces. *J. Mater. Chem. A* **2015**, *3* (18), 9379–9384. <https://doi.org/10.1039/C5TA01104C>.
- (28) Yong, J.; Chen, F.; Yang, Q.; Farooq, U.; Hou, X. Photoinduced Switchable Underwater Superoleophobicity–Superoleophilicity on Laser Modified Titanium Surfaces. *J. Mater. Chem. A* **2015**, *3* (20), 10703–10709. <https://doi.org/10.1039/C5TA01782C>.
- (29) Ding, C.; Zhu, Y.; Liu, M.; Feng, L.; Wan, M.; Jiang, L. PANI Nanowire Film with Underwater Superoleophobicity and Potential-Modulated Tunable Adhesion for No Loss Oil Droplet Transport. *Soft Matter* **2012**, *8* (35), 9064–9068. <https://doi.org/10.1039/C2SM25987G>.
- (30) Cheng, Z.; Lai, H.; Du, Y.; Fu, K.; Hou, R.; Zhang, N.; Sun, K. Underwater Superoleophilic to Superoleophobic Wetting Control on the Nanostructured Copper Substrates. *ACS Appl. Mater. Interfaces* **2013**, *5* (21), 11363–11370. <https://doi.org/10.1021/am403595z>.
- (31) Cai, Y.; Lin, L.; Xue, Z.; Liu, M.; Wang, S.; Jiang, L. Filefish-Inspired Surface Design for Anisotropic Underwater Oleophobicity. *Advanced Functional Materials* **2013**, *24* (6), 809–816. <https://doi.org/10.1002/adfm.201302034>.
- (32) Liao, Z.; Wu, G.; Lee, D.; Yang, S. Ultrastable Underwater Anti-Oil Fouling Coatings from Spray Assemblies of Polyelectrolyte Grafted Silica Nanochains. *ACS Appl. Mater. Interfaces* **2019**, *11* (14), 13642–13651. <https://doi.org/10.1021/acsami.8b19310>.
- (33) Zhang, W.; Zhu, Y.; Liu, X.; Wang, D.; Li, J.; Jiang, L.; Jin, J. Salt-Induced Fabrication of Superhydrophilic and Underwater Superoleophobic PAA-g-PVDF Membranes for Effective Separation of Oil-in-Water Emulsions. *Angew. Chem. Int. Ed.* **2014**, *53* (3), 856–860. <https://doi.org/10.1002/anie.201308183>.

- (34) Panatdasirisuk, W.; Liao, Z.; Vongsetskul, T.; Yang, S. Separation of Oil-in-Water Emulsions Using Hydrophilic Electrospun Membranes with Anisotropic Pores. *Langmuir* **2017**, *33* (23), 5872–5878. <https://doi.org/10.1021/acs.langmuir.7b01138>.
- (35) Yong, J.; Yang, Q.; Chen, F.; Du, G.; Shan, C.; Farooq, U.; Wang, J.; Hou, X. Using an “Underwater Superoleophobic Pattern” to Make a Liquid Lens Array. *RSC Advances* **2015**, *5* (51), 40907–40911. <https://doi.org/10.1039/C5RA04671H>.
- (36) Yong, J.; Chen, F.; Yang, Q.; Hou, X. Femtosecond Laser Controlled Wettability of Solid Surfaces. *Soft Matter* **2015**, *11* (46), 8897–8906. <https://doi.org/10.1039/C5SM02153G>.
- (37) Lin, L.; Liu, M.; Chen, L.; Chen, P.; Ma, J.; Han, D.; Jiang, L. Bio-Inspired Hierarchical Macromolecule–Nanoclay Hydrogels for Robust Underwater Superoleophobicity. *Advanced Materials* **2010**, *22* (43), 4826–4830. <https://doi.org/10.1002/adma.201002192>.
- (38) Liu, X.; Zhou, J.; Xue, Z.; Gao, J.; Meng, J.; Wang, S.; Jiang, L. Clam’s Shell Inspired High-Energy Inorganic Coatings with Underwater Low Adhesive Superoleophobicity. *Advanced Materials* **2012**, *24* (25), 3401–3405. <https://doi.org/10.1002/adma.201200797>.
- (39) Liu, X.; Gao, J.; Xue, Z.; Chen, L.; Lin, L.; Jiang, L.; Wang, S. Bioinspired Oil Strider Floating at the Oil/Water Interface Supported by Huge Superoleophobic Force. *ACS Nano* **2012**, *6* (6), 5614–5620. <https://doi.org/10.1021/nn301550v>.
- (40) Min, Y.; Tian, X.; Jing, L.; Chen, S. Controllable Vertical Growth onto Anatase TiO₂ Nanoparticle Films of ZnO Nanorod Arrays and Their Photoluminescence and Superhydrophilic Characteristics. *Journal of Physics and Chemistry of Solids* **2009**, *70* (5), 867–873. <https://doi.org/10.1016/j.jpcs.2009.04.008>.
- (41) Song, S.; Jing, L.; Li, S.; Fu, H.; Luan, Y. Superhydrophilic Anatase TiO₂ Film with the Micro- and Nanometer-Scale Hierarchical Surface Structure. *Materials Letters* **2008**, *62* (20), 3503–3505. <https://doi.org/10.1016/j.matlet.2008.03.005>.
- (42) Liu, H.; Feng, L.; Zhai, J.; Jiang, L.; Zhu, D. Reversible Wettability of a Chemical Vapor Deposition Prepared ZnO Film between Superhydrophobicity and Superhydrophilicity. *Langmuir* **2004**, *20* (14), 5659–5661. <https://doi.org/10.1021/la036280o>.
- (43) Du, X.; Huang, X.; Li, X.; Meng, X.; Yao, L.; He, J.; Huang, H.; Zhang, X. Wettability Behavior of Special Microscale ZnO Nail-Coated Mesh Films for Oil–Water Separation. *Journal of Colloid and Interface Science* **2015**, *458*, 79–86. <https://doi.org/10.1016/j.jcis.2015.07.040>.

- (44) Ge, D.; Yang, L.; Wang, C.; Lee, E.; Zhang, Y.; Yang, S. A Multi-Functional Oil–Water Separator from a Selectively Pre-Wetted Superamphiphobic Paper. *Chem. Commun.* **2015**, *51* (28), 6149–6152. <https://doi.org/10.1039/C4CC09813G>.
- (45) Ge, D.; Yang, L.; Zhang, Y.; Rahmawan, Y.; Yang, S. Transparent and Superamphiphobic Surfaces from One-Step Spray Coating of Stringed Silica Nanoparticle/Sol Solutions. *Particle & Particle Systems Characterization* **2014**, *31* (7), 763–770. <https://doi.org/10.1002/ppsc.201300382>.
- (46) Ge, D.; Yang, L.; Wu, G.; Yang, S. Spray Coating of Superhydrophobic and Angle-Independent Coloured Films. *Chem. Commun.* **2014**, *50* (19), 2469–2472. <https://doi.org/10.1039/C3CC48962K>.
- (47) Sasaki, K.; Tenjimbayashi, M.; Manabe, K.; Shiratori, S. Asymmetric Superhydrophobic/Superhydrophilic Cotton Fabrics Designed by Spraying Polymer and Nanoparticles. *ACS Appl. Mater. Interfaces* **2016**, *8* (1), 651–659. <https://doi.org/10.1021/acsami.5b09782>.
- (48) Gondal, M. A.; Sadullah, M. S.; Dastageer, M. A.; McKinley, G. H.; Panchanathan, D.; Varanasi, K. K. Study of Factors Governing Oil–Water Separation Process Using TiO₂ Films Prepared by Spray Deposition of Nanoparticle Dispersions. *ACS Appl. Mater. Interfaces* **2014**, *6* (16), 13422–13429. <https://doi.org/10.1021/am501867b>.
- (49) Liu, X.; He, J. Superhydrophilic and Antireflective Properties of Silica Nanoparticle Coatings Fabricated via Layer-by-Layer Assembly and Postcalcination. *J. Phys. Chem. C* **2009**, *113* (1), 148–152. <https://doi.org/10.1021/jp808324c>.
- (50) Lee, K. K.; Ahn, C. H. Superhydrophilic Multilayer Silica Nanoparticle Networks on a Polymer Microchannel Using a Spray Layer-by-Layer Nanoassembly Method. *ACS Appl. Mater. Interfaces* **2013**, *5* (17), 8523–8530. <https://doi.org/10.1021/am401945w>.
- (51) Lee, D.; Rubner, M. F.; Cohen, R. E. All-Nanoparticle Thin-Film Coatings. *Nano Lett.* **2006**, *6* (10), 2305–2312. <https://doi.org/10.1021/nl061776m>.
- (52) Cebeci, F. Ç.; Wu, Z.; Zhai, L.; Cohen, R. E.; Rubner, M. F. Nanoporosity-Driven Superhydrophilicity: A Means to Create Multifunctional Antifogging Coatings. *Langmuir* **2006**, *22* (6), 2856–2862. <https://doi.org/10.1021/la053182p>.
- (53) Zhu, Y.; Xie, W.; Zhang, F.; Xing, T.; Jin, J. Superhydrophilic In-Situ-Cross-Linked Zwitterionic Polyelectrolyte/PVDF-Blend Membrane for Highly Efficient Oil/Water Emulsion Separation. *ACS Appl. Mater. Interfaces* **2017**, *9* (11), 9603–9613. <https://doi.org/10.1021/acsami.6b15682>.

- (54) Gao, S.; Sun, J.; Liu, P.; Zhang, F.; Zhang, W.; Yuan, S.; Li, J.; Jin, J. A Robust Polyionized Hydrogel with an Unprecedented Underwater Anti-Crude-Oil-Adhesion Property. *Advanced Materials* **2016**, *28* (26), 5307–5314. <https://doi.org/10.1002/adma.201600417>.
- (55) Li, G.; Zhao, Y.; Lv, M.; Shi, Y.; Cao, D. Super Hydrophilic Poly(Ethylene Terephthalate) (PET)/Poly(Vinyl Alcohol) (PVA) Composite Fibrous Mats with Improved Mechanical Properties Prepared via Electrospinning Process. *Colloids and Surfaces A: Physicochemical and Engineering Aspects* **2013**, *436*, 417–424. <https://doi.org/10.1016/j.colsurfa.2013.07.014>.
- (56) Higaki, Y.; Kobayashi, M.; Murakami, D.; Takahara, A. Anti-Fouling Behavior of Polymer Brush Immobilized Surfaces. *Polymer Journal* **2016**, *48* (4), 325–331. <https://doi.org/10.1038/pj.2015.137>.
- (57) Kobayashi, M.; Terayama, Y.; Yamaguchi, H.; Terada, M.; Murakami, D.; Ishihara, K.; Takahara, A. Wettability and Antifouling Behavior on the Surfaces of Superhydrophilic Polymer Brushes. *Langmuir* **2012**, *28* (18), 7212–7222. <https://doi.org/10.1021/la301033h>.
- (58) Muller, P.; Sudre, G.; Théodoly, O. Wetting Transition on Hydrophobic Surfaces Covered by Polyelectrolyte Brushes. *Langmuir* **2008**, *24* (17), 9541–9550. <https://doi.org/10.1021/la801406x>.
- (59) Murakami, D.; Kobayashi, M.; Moriwaki, T.; Ikemoto, Y.; Jinnai, H.; Takahara, A. Spreading and Structuring of Water on Superhydrophilic Polyelectrolyte Brush Surfaces. *Langmuir* **2013**, *29* (4), 1148–1151. <https://doi.org/10.1021/la304697q>.
- (60) Klein, J.; Kumacheva, E.; Mahalu, D.; Perahia, D.; Fetters, L. J. Reduction of Frictional Forces between Solid Surfaces Bearing Polymer Brushes. *Nature* **1994**, *370* (6491), 634–636. <https://doi.org/10.1038/370634a0>.
- (61) Raviv, U.; Giasson, S.; Kampf, N.; Gohy, J.-F.; Jérôme, R.; Klein, J. Lubrication by Charged Polymers. *Nature* **2003**, *425* (6954), 163–165. <https://doi.org/10.1038/nature01970>.
- (62) Higaki, Y.; Inutsuka, Y.; Sakamaki, T.; Terayama, Y.; Takenaka, A.; Higaki, K.; Yamada, N. L.; Moriwaki, T.; Ikemoto, Y.; Takahara, A. Effect of Charged Group Spacer Length on Hydration State in Zwitterionic Poly(Sulfobetaine) Brushes. *Langmuir* **2017**, *33* (34), 8404–8412. <https://doi.org/10.1021/acs.langmuir.7b01935>.
- (63) Sholl, D. S.; Lively, R. P. Seven Chemical Separations to Change the World. *Nature News* **2016**, *532* (7600), 435. <https://doi.org/10.1038/532435a>.
- (64) Geise, G. M.; Lee, H.-S.; Miller, D. J.; Freeman, B. D.; McGrath, J. E.; Paul, D. R. Water Purification by Membranes: The Role of Polymer Science. *Journal of*

- Polymer Science Part B: Polymer Physics* **2010**, 48 (15), 1685–1718. <https://doi.org/10.1002/polb.22037>.
- (65) Chen, C.; Weng, D.; Mahmood, A.; Chen, S.; Wang, J. Separation Mechanism and Construction of Surfaces with Special Wettability for Oil/Water Separation. *ACS Appl. Mater. Interfaces* **2019**, 11 (11), 11006–11027. <https://doi.org/10.1021/acsami.9b01293>.
- (66) Xue, Z.; Cao, Y.; Liu, N.; Feng, L.; Jiang, L. Special Wettable Materials for Oil/Water Separation. *J. Mater. Chem. A* **2014**, 2 (8), 2445–2460. <https://doi.org/10.1039/C3TA13397D>.
- (67) Zarghami, S.; Mohammadi, T.; Sadrzadeh, M.; Van der Bruggen, B. Superhydrophilic and Underwater Superoleophobic Membranes - A Review of Synthesis Methods. *Progress in Polymer Science* **2019**, 98, 101166. <https://doi.org/10.1016/j.progpolymsci.2019.101166>.
- (68) Gao, S. J.; Shi, Z.; Zhang, W. B.; Zhang, F.; Jin, J. Photoinduced Superwetting Single-Walled Carbon Nanotube/TiO₂ Ultrathin Network Films for Ultrafast Separation of Oil-in-Water Emulsions. *ACS Nano* **2014**, 8 (6), 6344–6352. <https://doi.org/10.1021/nn501851a>.
- (69) Wang, J.-H.; Zhu, L.-P.; Zhu, B.-K.; Xu, Y.-Y. Fabrication of Superhydrophilic Poly(Styrene-Alt-Maleic Anhydride)/Silica Hybrid Surfaces on Poly(Vinylidene Fluoride) Membranes. *Journal of Colloid and Interface Science* **2011**, 363 (2), 676–681. <https://doi.org/10.1016/j.jcis.2011.07.052>.
- (70) Choi, M.; Xiangde, L.; Park, J.; Choi, D.; Heo, J.; Chang, M.; Lee, C.; Hong, J. Superhydrophilic Coatings with Intricate Nanostructure Based on Biotic Materials for Antifogging and Antibiofouling Applications. *Chemical Engineering Journal* **2017**, 309, 463–470. <https://doi.org/10.1016/j.cej.2016.10.052>.
- (71) Léonard, G. L.-M.; Remy, S.; Heinrichs, B. Overview of Superhydrophilic, Photocatalytic and Anticorrosive Properties of TiO₂ Thin Films Doped with Multi-Walled Carbon Nanotubes and Deposited on 316L Stainless Steel. *Materials Today: Proceedings* **2016**, 3 (2), 434–438. <https://doi.org/10.1016/j.matpr.2016.01.037>.
- (72) Howarter J. A.; Youngblood J. P. Self-Cleaning and Anti-Fog Surfaces via Stimuli-Responsive Polymer Brushes. *Advanced Materials* **2007**, 19 (22), 3838–3843. <https://doi.org/10.1002/adma.200700156>.
- (73) Brown, P. S.; Atkinson, O. D. L. A.; Badyal, J. P. S. Ultrafast Oleophobic–Hydrophilic Switching Surfaces for Antifogging, Self-Cleaning, and Oil–Water Separation. *ACS Appl. Mater. Interfaces* **2014**, 6 (10), 7504–7511. <https://doi.org/10.1021/am500882y>.

- (74) Otitoju, T. A.; Ahmad, A. L.; Ooi, B. S. Superhydrophilic (Superwetting) Surfaces: A Review on Fabrication and Application. *Journal of Industrial and Engineering Chemistry* **2017**, *47*, 19–40. <https://doi.org/10.1016/j.jiec.2016.12.016>.
- (75) Wang, Y.; Gong, X. Special Oleophobic and Hydrophilic Surfaces: Approaches, Mechanisms, and Applications. *J. Mater. Chem. A* **2017**, *5* (8), 3759–3773. <https://doi.org/10.1039/C6TA10474F>.
- (76) Xue Zhongxin; Liu Mingjie; Jiang Lei. Recent Developments in Polymeric Superoleophobic Surfaces. *Journal of Polymer Science Part B: Polymer Physics* **2012**, *50* (17), 1209–1224. <https://doi.org/10.1002/polb.23115>.
- (77) Gu, C.; Zhang, J.; Tu, J. A Strategy of Fast Reversible Wettability Changes of WO₃ Surfaces between Superhydrophilicity and Superhydrophobicity. *Journal of Colloid and Interface Science* **2010**, *352* (2), 573–579. <https://doi.org/10.1016/j.jcis.2010.08.064>.
- (78) Cai, Y.; Lin, L.; Xue, Z.; Liu, M.; Wang, S.; Jiang, L. Filefish-Inspired Surface Design for Anisotropic Underwater Oleophobicity. *Adv. Funct. Mater.* **2014**, *24* (6), 809–816. <https://doi.org/10.1002/adfm.201302034>.
- (79) Ge, D.; Yang, L.; Wang, C.; Lee, E.; Zhang, Y.; Yang, S. A Multi-Functional Oil–Water Separator from a Selectively Pre-Wetted Superamphiphobic Paper. **2015**, *51* (28), 6149–6152. <https://doi.org/10.1039/C4CC09813G>.
- (80) Ge, D.; Yang, L.; Zhang, Y.; Rahmawan, Y.; Yang, S. Transparent and Superamphiphobic Surfaces from One-Step Spray Coating of Stringed Silica Nanoparticle/Sol Solutions. *Particle & Particle Systems Characterization* **2014**, *31* (7), 763–770. <https://doi.org/10.1002/ppsc.201300382>.
- (81) Gondal, M. A.; Sadullah, M. S.; Dastageer, M. A.; McKinley, G. H.; Panchanathan, D.; Varanasi, K. K. Study of Factors Governing Oil–Water Separation Process Using TiO₂ Films Prepared by Spray Deposition of Nanoparticle Dispersions. *ACS Appl. Mater. Interfaces* **2014**, *6* (16), 13422–13429. <https://doi.org/10.1021/am501867b>.
- (82) Kota, A. K.; Kwon, G.; Choi, W.; Mabry, J. M.; Tuteja, A. Hygro-Responsive Membranes for Effective Oil–Water Separation. *Nature Communications* **2012**, *3*, 1025. <https://doi.org/10.1038/ncomms2027>.
- (83) Yang, J.; Zhang, Z.; Xu, X.; Zhu, X.; Men, X.; Zhou, X. Superhydrophilic–Superoleophobic Coatings. *J. Mater. Chem.* **2012**, *22* (7), 2834–2837. <https://doi.org/10.1039/C2JM15987B>.
- (84) Tripathi, B. P.; Dubey, N. C.; Subair, R.; Choudhury, S.; Stamm, M. Enhanced Hydrophilic and Antifouling Polyacrylonitrile Membrane with Polydopamine

- Modified Silica Nanoparticles. *RSC Adv.* **2016**, *6* (6), 4448–4457. <https://doi.org/10.1039/C5RA22160A>.
- (85) Kobayashi, M.; Terayama, Y.; Yamaguchi, H.; Terada, M.; Murakami, D.; Ishihara, K.; Takahara, A. Wettability and Antifouling Behavior on the Surfaces of Superhydrophilic Polymer Brushes. *Langmuir* **2012**, *28* (18), 7212–7222. <https://doi.org/10.1021/la301033h>.
- (86) Cai, Y.; Lu, Q.; Guo, X.; Wang, S.; Qiao, J.; Jiang, L. Salt-Tolerant Superoleophobicity on Alginate Gel Surfaces Inspired by Seaweed (*Saccharina Japonica*). *Adv. Mater.* **2015**, *27* (28), 4162–4168. <https://doi.org/10.1002/adma.201404479>.
- (87) Ogihara, H.; Xie, J.; Okagaki, J.; Saji, T. Simple Method for Preparing Superhydrophobic Paper: Spray-Deposited Hydrophobic Silica Nanoparticle Coatings Exhibit High Water-Repellency and Transparency. *Langmuir* **2012**, *28* (10), 4605–4608. <https://doi.org/10.1021/la204492q>.
- (88) Zhang, Y.; Ge, D.; Yang, S. Spray-Coating of Superhydrophobic Aluminum Alloys with Enhanced Mechanical Robustness. *Journal of Colloid and Interface Science* **2014**, *423*, 101–107. <https://doi.org/10.1016/j.jcis.2014.02.024>.
- (89) Karunakaran, R. G.; Lu, C.-H.; Zhang, Z.; Yang, S. Highly Transparent Superhydrophobic Surfaces from the Coassembly of Nanoparticles (≤ 100 Nm). *Langmuir* **2011**, *27* (8), 4594–4602. <https://doi.org/10.1021/la104067c>.
- (90) Xu, L.; Karunakaran, R. G.; Guo, J.; Yang, S. Transparent, Superhydrophobic Surfaces from One-Step Spin Coating of Hydrophobic Nanoparticles. *ACS Appl. Mater. Interfaces* **2012**, *4* (2), 1118–1125. <https://doi.org/10.1021/am201750h>.
- (91) Zhou, H.; Wang, H.; Niu, H.; Gestos, A.; Lin, T. Robust, Self-Healing Superamphiphobic Fabrics Prepared by Two-Step Coating of Fluoro-Containing Polymer, Fluoroalkyl Silane, and Modified Silica Nanoparticles. *Adv. Funct. Mater.* **2013**, *23* (13), 1664–1670. <https://doi.org/10.1002/adfm.201202030>.
- (92) Golovin, K.; Lee, D. H.; Mabry, J. M.; Tuteja, A. Transparent, Flexible, Superomniphobic Surfaces with Ultra-Low Contact Angle Hysteresis. *Angew. Chem. Int. Ed.* **2013**, *52* (49), 13007–13011. <https://doi.org/10.1002/anie.201307222>.
- (93) Occhiello, E.; Morra, M.; Morini, G.; Garbassi, F.; Humphrey, P. Oxygen-Plasma-Treated Polypropylene Interfaces with Air, Water, and Epoxy Resins: Part I. Air and Water. *Journal of Applied Polymer Science* **1991**, *42* (2), 551–559. <https://doi.org/10.1002/app.1991.070420228>.
- (94) Ishizaki, T.; Saito, N.; Takai, O. Correlation of Cell Adhesive Behaviors on Superhydrophobic, Superhydrophilic, and Micropatterned

Superhydrophobic/Superhydrophilic Surfaces to Their Surface Chemistry. *Langmuir* **2010**, *26* (11), 8147–8154. <https://doi.org/10.1021/la904447c>.

- (95) Patel, P.; Choi, C. K.; Meng, D. D. Superhydrophilic Surfaces for Antifouling and Antifouling Microfluidic Devices. *JALA: Journal of the Association for Laboratory Automation* **2010**, *15* (2), 114–119. <https://doi.org/10.1016/j.jala.2009.10.012>.
- (96) He, K.; Duan, H.; Chen, G. Y.; Liu, X.; Yang, W.; Wang, D. Cleaning of Oil Fouling with Water Enabled by Zwitterionic Polyelectrolyte Coatings: Overcoming the Imperative Challenge of Oil–Water Separation Membranes. *ACS Nano* **2015**, *9* (9), 9188–9198. <https://doi.org/10.1021/acs.nano.5b03791>.
- (97) Guo, T.; Li, M.; Heng, L.; Jiang, L. Design of Honeycomb Structure Surfaces with Controllable Oil Adhesion Underwater. *RSC Adv.* **2015**, *5* (76), 62078–62083. <https://doi.org/10.1039/C5RA10514E>.
- (98) Chen, K.; Zhou, S.; Wu, L. Self-Healing Underwater Superoleophobic and Antibiofouling Coatings Based on the Assembly of Hierarchical Microgel Spheres. *ACS Nano* **2016**, *10* (1), 1386–1394. <https://doi.org/10.1021/acs.nano.5b06816>.
- (99) Cheng, G.; Liao, M.; Zhao, D.; Zhou, J. Molecular Understanding on the Underwater Oleophobicity of Self-Assembled Monolayers: Zwitterionic versus Nonionic. *Langmuir* **2017**, *33* (7), 1732–1741. <https://doi.org/10.1021/acs.langmuir.6b03988>.
- (100) Liao, M.; Cheng, G.; Zhou, J. Underwater Superoleophobicity of Pseudozwitterionic SAMs: Effects of Chain Length and Ionic Strength. *J. Phys. Chem. C* **2017**, *121* (32), 17390–17401. <https://doi.org/10.1021/acs.jpcc.7b06088>.
- (101) Shi, C.; Yan, B.; Xie, L.; Zhang, L.; Wang, J.; Takahara, A.; Zeng, H. Long-Range Hydrophilic Attraction between Water and Polyelectrolyte Surfaces in Oil. *Angewandte Chemie International Edition* **2016**, *55* (48), 15017–15021. <https://doi.org/10.1002/anie.201608219>.
- (102) Wu, G.; Ge, D.; Zhao, Y.; Yang, S. Ultrathin (Sub-100 Nm) Superhydrophobic and Omni-Transparent Coatings from Chained Nanoparticles with Large Surface Asperity, 2018.
- (103) Heikkinen, J. J.; Heiskanen, J. P.; Hormi, O. E. O. Grafting of Functionalized Silica Particles with Poly(Acrylic Acid). *Polym. Adv. Technol.* **2006**, *17* (6), 426–429. <https://doi.org/10.1002/pat.727>.
- (104) Scott, G. D.; Kilgour, D. M. The Density of Random Close Packing of Spheres. *J. Phys. D: Appl. Phys.* **1969**, *2* (6), 863. <https://doi.org/10.1088/0022-3727/2/6/311>.

- (105) Torquato, S.; Truskett, T. M.; Debenedetti, P. G. Is Random Close Packing of Spheres Well Defined? *Phys. Rev. Lett.* **2000**, *84* (10), 2064–2067. <https://doi.org/10.1103/PhysRevLett.84.2064>.
- (106) Shirtcliffe, N. J.; McHale, G.; Atherton, S.; Newton, M. I. An Introduction to Superhydrophobicity. *Advances in Colloid and Interface Science* **2010**, *161* (1–2), 124–138. <https://doi.org/10.1016/j.cis.2009.11.001>.
- (107) Nosonovsky, M.; Bhushan, B. Hierarchical Roughness Optimization for Biomimetic Superhydrophobic Surfaces. *Ultramicroscopy* **2007**, *107* (10–11), 969–979. <https://doi.org/10.1016/j.ultramic.2007.04.011>.
- (108) Wong, T.-S.; Kang, S. H.; Tang, S. K. Y.; Smythe, E. J.; Hatton, B. D.; Grinthal, A.; Aizenberg, J. Bioinspired Self-Repairing Slippery Surfaces with Pressure-Stable Omniphobicity. *Nature* **2011**, *477* (7365), 443–447. <https://doi.org/10.1038/nature10447>.
- (109) Bormashenko, E. Progress in Understanding Wetting Transitions on Rough Surfaces. *Advances in Colloid and Interface Science* **2015**, *222*, 92–103. <https://doi.org/10.1016/j.cis.2014.02.009>.
- (110) Krupenkin, T. N.; Taylor, J. A.; Schneider, T. M.; Yang, S. From Rolling Ball to Complete Wetting: The Dynamic Tuning of Liquids on Nanostructured Surfaces. *Langmuir* **2004**, *20* (10), 3824–3827. <https://doi.org/10.1021/la036093q>.
- (111) Bormashenko, E.; Gendelman, O.; Whyman, G. Superhydrophobicity of Lotus Leaves versus Birds Wings: Different Physical Mechanisms Leading to Similar Phenomena. *Langmuir* **2012**, *28* (42), 14992–14997. <https://doi.org/10.1021/la303340x>.
- (112) Kleingartner, J. A.; Srinivasan, S.; Mabry, J. M.; Cohen, R. E.; McKinley, G. H. Utilizing Dynamic Tensiometry to Quantify Contact Angle Hysteresis and Wetting State Transitions on Nonwetting Surfaces. *Langmuir* **2013**, *29* (44), 13396–13406. <https://doi.org/10.1021/la4022678>.
- (113) Zhai, L.; Cebeci, F. Ç.; Cohen, R. E.; Rubner, M. F. Stable Superhydrophobic Coatings from Polyelectrolyte Multilayers. *Nano Lett.* **2004**, *4* (7), 1349–1353. <https://doi.org/10.1021/nl049463j>.
- (114) Prakash, S.; Xi, E.; Patel, A. J. Spontaneous Recovery of Superhydrophobicity on Nanotextured Surfaces. *PNAS* **2016**, *113* (20), 5508–5513. <https://doi.org/10.1073/pnas.1521753113>.
- (115) Huber, G.; Mantz, H.; Spolenak, R.; Mecke, K.; Jacobs, K.; Gorb, S. N.; Arzt, E. Evidence for Capillarity Contributions to Gecko Adhesion from Single Spatula Nanomechanical Measurements. *PNAS* **2005**, *102* (45), 16293–16296. <https://doi.org/10.1073/pnas.0506328102>.

- (116) Liu, Q.; Patel, A. A.; Liu, L. Superhydrophilic and Underwater Superoleophobic Poly(Sulfobetaine Methacrylate)-Grafted Glass Fiber Filters for Oil–Water Separation. *ACS Appl. Mater. Interfaces* **2014**, *6* (12), 8996–9003. <https://doi.org/10.1021/am502302g>.
- (117) Joung, Y. S.; Buie, C. R. Antiwetting Fabric Produced by a Combination of Layer-by-Layer Assembly and Electrophoretic Deposition of Hydrophobic Nanoparticles. *ACS Appl. Mater. Interfaces* **2015**, *7* (36), 20100–20110. <https://doi.org/10.1021/acsami.5b05233>.
- (118) Fakhru'l-Razi, A.; Pendashteh, A.; Abdullah, L. C.; Biak, D. R. A.; Madaeni, S. S.; Abidin, Z. Z. Review of Technologies for Oil and Gas Produced Water Treatment. *Journal of Hazardous Materials* **2009**, *170* (2), 530–551. <https://doi.org/10.1016/j.jhazmat.2009.05.044>.
- (119) Etchepare, R.; Oliveira, H.; Azevedo, A.; Rubio, J. Separation of Emulsified Crude Oil in Saline Water by Dissolved Air Flotation with Micro and Nanobubbles. *Separation and Purification Technology* **2017**, *186*, 326–332. <https://doi.org/10.1016/j.seppur.2017.06.007>.
- (120) Kwon, W.-T.; Park, K.; Han, S. D.; Yoon, S. M.; Kim, J. Y.; Bae, W.; Rhee, Y. W. Investigation of Water Separation from Water-in-Oil Emulsion Using Electric Field. *Journal of Industrial and Engineering Chemistry* **2010**, *16* (5), 684–687. <https://doi.org/10.1016/j.jiec.2010.07.018>.
- (121) Koltuniewicz, A. B.; Field, R. W.; Arnot, T. C. Cross-Flow and Dead-End Microfiltration of Oily-Water Emulsion. Part I: Experimental Study and Analysis of Flux Decline. *Journal of Membrane Science* **1995**, *102*, 193–207. [https://doi.org/10.1016/0376-7388\(94\)00320-X](https://doi.org/10.1016/0376-7388(94)00320-X).
- (122) Zhu, Y.; Wang, J.; Zhang, F.; Gao, S.; Wang, A.; Fang, W.; Jin, J. Zwitterionic Nanohydrogel Grafted PVDF Membranes with Comprehensive Antifouling Property and Superior Cycle Stability for Oil-in-Water Emulsion Separation. *Advanced Functional Materials* **2018**, *28* (40), 1804121. <https://doi.org/10.1002/adfm.201804121>.
- (123) Yu, H.; Lian, Z.; Xu, J.; Wan, Y.; Wang, Z.; Li, Y.; Yu, Z.; Weng, Z. Mechanically Durable Underwater Superoleophobic Surfaces Based on Hydrophilic Bulk Metals for Oil/Water Separation. *Applied Surface Science* **2018**, *437*, 400–409. <https://doi.org/10.1016/j.apsusc.2017.08.120>.
- (124) Ma, Q.; Cheng, H.; Yu, Y.; Huang, Y.; Lu, Q.; Han, S.; Chen, J.; Wang, R.; Fane, A. G.; Zhang, H. Preparation of Superhydrophilic and Underwater Superoleophobic Nanofiber-Based Meshes from Waste Glass for Multifunctional Oil/Water Separation. *Small* **2017**, *13* (19), 1700391. <https://doi.org/10.1002/sml.201700391>.

- (125) Dong, Y.; Li, J.; Shi, L.; Wang, X.; Guo, Z.; Liu, W. Underwater Superoleophobic Graphene Oxide Coated Meshes for the Separation of Oil and Water. *Chem. Commun.* **2014**, *50* (42), 5586–5589. <https://doi.org/10.1039/C4CC01408A>.
- (126) Li, J.; Yan, L.; Li, H.; Li, W.; Zha, F.; Lei, Z. Underwater Superoleophobic Palygorskite Coated Meshes for Efficient Oil/Water Separation. *J. Mater. Chem. A* **2015**, *3* (28), 14696–14702. <https://doi.org/10.1039/C5TA02870A>.
- (127) Li, Y.; Zheng, X.; Yan, Z.; Tian, D.; Ma, J.; Zhang, X.; Jiang, L. Closed Pore Structured NiCo₂O₄-Coated Nickel Foams for Stable and Effective Oil/Water Separation. *ACS Appl. Mater. Interfaces* **2017**, *9* (34), 29177–29184. <https://doi.org/10.1021/acsami.7b05385>.
- (128) Yu, Z.; Yun, F. F.; Gong, Z.; Yao, Q.; Dou, S.; Liu, K.; Jiang, L.; Wang, X. A Novel Reusable Superhydrophilic NiO/Ni Mesh Produced by a Facile Fabrication Method for Superior Oil/Water Separation. *J. Mater. Chem. A* **2017**, *5* (22), 10821–10826. <https://doi.org/10.1039/C7TA01987D>.
- (129) Rana, M.; Chen, J.-T.; Yang, S.; Ma, P.-C. Biomimetic Superoleophobicity of Cotton Fabrics for Efficient Oil–Water Separation. *Advanced Materials Interfaces* **2016**, *3* (16), 1600128. <https://doi.org/10.1002/admi.201600128>.
- (130) Shome, A.; Rather, A. M.; Manna, U. Aloe Vera Mucilage Derived Highly Tolerant Underwater Superoleophobic Coatings. *J. Mater. Chem. A* **2018**, *6* (45), 22465–22471. <https://doi.org/10.1039/C8TA08481E>.
- (131) Zhao, X.; Su, Y.; Cao, J.; Li, Y.; Zhang, R.; Liu, Y.; Jiang, Z. Fabrication of Antifouling Polymer–Inorganic Hybrid Membranes through the Synergy of Biomimetic Mineralization and Nonsolvent Induced Phase Separation. *J. Mater. Chem. A* **2015**, *3* (14), 7287–7295. <https://doi.org/10.1039/C5TA00654F>.
- (132) Zeng, J.; Guo, Z. Superhydrophilic and Underwater Superoleophobic MFI Zeolite-Coated Film for Oil/Water Separation. *Colloids and Surfaces A: Physicochemical and Engineering Aspects* **2014**, *444*, 283–288. <https://doi.org/10.1016/j.colsurfa.2013.12.071>.
- (133) Xiong, Z.; Lin, H.; Zhong, Y.; Qin, Y.; Li, T.; Liu, F. Robust Superhydrophilic Polylactide (PLA) Membranes with a TiO₂ Nano-Particle Inlaid Surface for Oil/Water Separation. *J. Mater. Chem. A* **2017**, *5* (14), 6538–6545. <https://doi.org/10.1039/C6TA11156D>.
- (134) Cao, G.; Zhang, W.; Jia, Z.; Liu, F.; Yang, H.; Yu, Q.; Wang, Y.; Di, X.; Wang, C.; Ho, S.-H. Dually Prewetted Underwater Superoleophobic and under Oil Superhydrophobic Fabric for Successive Separation of Light Oil/Water/Heavy Oil Three-Phase Mixtures. *ACS Appl. Mater. Interfaces* **2017**, *9* (41), 36368–36376. <https://doi.org/10.1021/acsami.7b08997>.

- (135) Zhou, H.; Guo, Z. Superwetting Janus Membranes: Focusing on Unidirectional Transport Behaviors and Multiple Applications. *J. Mater. Chem. A* **2019**, *7* (21), 12921–12950. <https://doi.org/10.1039/C9TA02682G>.
- (136) Roh, K.-H.; Martin, D. C.; Lahann, J. Biphasic Janus Particles with Nanoscale Anisotropy. *Nature Mater* **2005**, *4* (10), 759–763. <https://doi.org/10.1038/nmat1486>.
- (137) Yang, H.-C.; Hou, J.; Chen, V.; Xu, Z.-K. Janus Membranes: Exploring Duality for Advanced Separation. *Angewandte Chemie International Edition* **2016**, *55* (43), 13398–13407. <https://doi.org/10.1002/anie.201601589>.
- (138) Yang, H.-C.; Xie, Y.; Hou, J.; Cheetham, A. K.; Chen, V.; Darling, S. B. Janus Membranes: Creating Asymmetry for Energy Efficiency. *Advanced Materials* **2018**, *30* (43), 1801495. <https://doi.org/10.1002/adma.201801495>.
- (139) Xu, C.; Feng, R.; Song, F.; Wang, X.-L.; Wang, Y.-Z. Desert Beetle-Inspired Superhydrophilic/Superhydrophobic Patterned Cellulose Film with Efficient Water Collection and Antibacterial Performance. *ACS Sustainable Chem. Eng.* **2018**, *6* (11), 14679–14684. <https://doi.org/10.1021/acssuschemeng.8b03247>.
- (140) Wang, Z.; Wang, Y.; Liu, G. Rapid and Efficient Separation of Oil from Oil-in-Water Emulsions Using a Janus Cotton Fabric. *Angewandte Chemie International Edition* **2016**, *55* (4), 1291–1294. <https://doi.org/10.1002/anie.201507451>.
- (141) Han, H.; Baik, S.; Xu, B.; Seo, J.; Lee, S.; Shin, S.; Lee, J.; Koo, J. H.; Mei, Y.; Pang, C.; et al. Bioinspired Geometry-Switchable Janus Nanofibers for Eye-Readable H₂ Sensors. *Advanced Functional Materials* **2017**, *27* (29), 1701618. <https://doi.org/10.1002/adfm.201701618>.
- (142) Hu, L.; Gao, S.; Zhu, Y.; Zhang, F.; Jiang, L.; Jin, J. An Ultrathin Bilayer Membrane with Asymmetric Wettability for Pressure Responsive Oil/Water Emulsion Separation. *J. Mater. Chem. A* **2015**, *3* (46), 23477–23482. <https://doi.org/10.1039/C5TA03975D>.
- (143) Wu, J.; Wang, N.; Wang, L.; Dong, H.; Zhao, Y.; Jiang, L. Unidirectional Water-Penetration Composite Fibrous Film via Electrospinning. *Soft Matter* **2012**, *8* (22), 5996–5999. <https://doi.org/10.1039/C2SM25514F>.
- (144) An, Y.-P.; Yang, J.; Yang, H.-C.; Wu, M.-B.; Xu, Z.-K. Janus Membranes with Charged Carbon Nanotube Coatings for Deemulsification and Separation of Oil-in-Water Emulsions. *ACS Appl. Mater. Interfaces* **2018**, *10* (11), 9832–9840. <https://doi.org/10.1021/acsami.7b19700>.
- (145) Wang, H.; Zhou, H.; Yang, W.; Zhao, Y.; Fang, J.; Lin, T. Selective, Spontaneous One-Way Oil-Transport Fabrics and Their Novel Use for Gauging Liquid Surface

- Tension. *ACS Appl. Mater. Interfaces* **2015**, *7* (41), 22874–22880. <https://doi.org/10.1021/acsami.5b05678>.
- (146) Chen, J.; Liu, Y.; Guo, D.; Cao, M.; Jiang, L. Under-Water Unidirectional Air Penetration via a Janus Mesh. *Chem. Commun.* **2015**, *51* (59), 11872–11875. <https://doi.org/10.1039/C5CC03804A>.
- (147) Zhang, Y.; Barboiu, M. Dynameric Asymmetric Membranes for Directional Water Transport. *Chem. Commun.* **2015**, *51* (88), 15925–15927. <https://doi.org/10.1039/C5CC06805C>.
- (148) Guillen, G. R.; Pan, Y.; Li, M.; Hoek, E. M. V. Preparation and Characterization of Membranes Formed by Nonsolvent Induced Phase Separation: A Review. *Ind. Eng. Chem. Res.* **2011**, *50* (7), 3798–3817. <https://doi.org/10.1021/ie101928r>.
- (149) Doumenc, F.; Salmon, J.-B.; Guerrier, B. Modeling Flow Coating of Colloidal Dispersions in the Evaporative Regime: Prediction of Deposit Thickness. *Langmuir* **2016**, *32* (51), 13657–13668. <https://doi.org/10.1021/acs.langmuir.6b02282>.
- (150) Le Berre, M.; Chen, Y.; Baigl, D. From Convective Assembly to Landau–Levich Deposition of Multilayered Phospholipid Films of Controlled Thickness. *Langmuir* **2009**, *25* (5), 2554–2557. <https://doi.org/10.1021/la803646e>.